Research on Load-Independent Design for High-Frequency Resonant Inverters and Rectifiers

February 2025

Yutaro KOMIYAMA

Graduate School of Science and Engineering
CHIBA UNIVERSITY

(千葉大学審査学位論文)

Research on Load-Independent Design for High-Frequency Resonant Inverters and Rectifiers

February 2025

Yutaro KOMIYAMA

Graduate School of Science and Engineering
CHIBA UNIVERSITY

Table of Contents

List of Figures

List of Tables

Acknowlegement

First and foremost, I would like to express my heartfelt gratitude to my supervisor, Prof. Hiroo Sekiya, for his invaluable guidance and encouragement. He not only provided technical guidance in my research but also taught me how to conduct myself at academic conferences, the mindset required of a researcher, and how to build relationships with researchers. The five years I spent under his supervision have undoubtedly laid a solid foundation for my future as a researcher. I cannot fully express in words how deeply grateful I am.

Next, I would like to express my gratitude to my co-supervisor, Prof. Kien Nguyen, for his guidance and valuable advice. The perspectives provided by a researcher from a different field were essential in advancing my research and have been immensely helpful.

Finally, I would like to express my heartfelt gratitude to my family, who supported me throughout my doctoral studies. I do not take for granted that you respected my decisions and always stood by me. Thank you so much for your constant support and communication.

Chiba University

Yutaro KOMIYAMA

Chapter 1

General Introduction

1.1 Research Background

Today, electric energy has become a fundamental and essential part of human life. Electrical energy can be used in wide range of applications because it can be converted into various type of other energy, such as kinetic, heat, light, and sound. Additionally, electrical energy is well-suited for power conversion and transmission, making it a critical infrastructure in modern society. In order to utilize electrical energy in various applications and scenarios, power converters are necessary. The primary function of power converters is to convert the type of electrical power, such as DC and AC, as well as the voltage and current levels, into the desired form.

Most power converters are based the switching power converter, which uses the switching device in the circuit. The switching devices can switch between short-circuit and open-circuit conditions, which can realize high-efficiency power conversion. As the switching devices play a central role in the switching power converters, the power electronics technology has grown following the development of the switching devices [1]. The switching devices trace their origins to the thyristor

developed in 1956, and have evolved through Gate Turn-Off thyristor (GTO) [2], Metal-Oxide-Semiconductor Field-Effect Transistor (MOSFET) [3], and Insulated Gate Bipolar Transistor (IGBT) [4]. These technological advancements have not only improved the ease of use of the devices but also significantly enhanced their operating frequency and power levels. In recent years, switching devices using wide-bandgap semiconductors such as Gallium Nitride (GaN) and Silicon Carbide (SiC) have garnered attention [5]. The GaN and SiC devices expand the operating range compared to conventional devices, enabling high-frequency operation in the MHz range at power levels up to several kW. Also, the GaN and SiC switching devices are rapidly expanding their market size, with an expected growth rate of 35.80% CAGR, reaching a market size of 5 billion USD by 2032 [6].

With the evolution of the switching devices as a backdrop, high-frequency operation has become one of the key directions in the power converter development. By increasing the switching frequency, the required passive components become smaller, contributing to the miniaturization of overall circuit size. Compact and lightweight circuits are highly demanded in various applications such as AC/DC adapters, in-vehicle power supplies, and portable devices. Moreover, the trend toward higher frequencies also occurs in Wireless Power Transfer (WPT) systems. The standards for WPT, including Qi and AirFuel, have been established, with specifications in the MHz frequency range. In this way, power electronics technology is evolving towards higher frequencies, and it is of great significance in the industrial demand. On the other hand, a technical challenge in increasing the switching frequency is the increase in switching losses. As the switching losses occur with the turn ON and OFF operation, the switching losses increase proportionally with the frequency.

In order to suppress the switching losses, achieving soft switching is an effective measure. By achieving soft switching, the overlap of current and voltage during the switching period can be eliminated, enabling high-efficiency operation even at high frequencies. Therefore, achieving soft switching is an essential design principle for high-frequency switching circuits.

A representative high-frequency soft-switching circuit is the class-E inverter [7]. The class-E inverter achieves Zero-Voltage Switching (ZVS) and Zero-Derivative Switching (ZDS), where both the voltage and its derivative are zero when the switch turns ON. These switching conditions enable high-efficiency power conversion even under high-frequency operation. In addition, the class-E inverter works with a single switching device whose source terminal is connected to a grand. Therefore, the class-E inverter is suitable for high-frequency drives as there is no requirement for high-side gate drives. Due to the superior performance of the class-E inverter in high-frequency operation, the class-E topology has been extended to various circuit topologies. The class-E rectifier [8] is the time-reversal dual of the class-E inverter. Namely, it performs AC-DC conversion, which is the reverse operation of the DC-AC inversion. Although the class-E rectifier can be implemented with diode rectification, the class-E synchronous rectifiers [9] have also been proposed to achieve even higher efficiency. By replacing the diode with the active switch, the power loss due to the forward voltage drop in the diode can be eliminated. Additionally, the class-E power oscillator [10] has been proposed. The class-E power oscillator makes a self-oscillation by adding a passive feedback network to the class-E inverter. Since the power oscillator is unnecessary to have auxiliary power supplies or digital devices, they contribute to circuit simplification and cost reduction. In this way, class-E

resonant circuits have been extensively researched and advanced for applications in high-frequency domains.

However, the class-E inverter exhibits high sensitivity to load variations [11]. When load variations occur, it fails to maintain ZVS, resulting in a significant deterioration in power conversion efficiency. Moreover, output voltage and current fluctuate, making it impossible to achieve the desired output. The weakness in the sensitivity arises because the class-E switching is only satisfied under specific component values, including the load resistance, which is a common drawback of all the class-E resonant circuits. In order to address the load variations, the frequency-modulation control and ON/OFF control are typically applied to the class-E resonant circuits to achieve output regulation and compensation for the ZVS. Nevertheless, the controls at the MHz range have limitations in their bandwidth and accuracy. Additionally, the propagation delays that occur in digital devices appear at high-frequency operation, which complicates the control. Therefore, managing output power and power conversion efficiency against load variations is a significant challenge in the class-E resonant circuits.

Within this background, the load-independent class-E inverter [12] has garnered significant attention. The load-independent operation is a special mode discovered in the class-E inverters, where appropriate parameter tuning can impart robustness to the inverter. In this operating mode, soft switching and output regulation can be achieved without additional control or circuit, even against load variations. As such, it holds the potential to fundamentally solve the issue of load variations in high-frequency circuits. Therefore, it is valuable to extend the concept of the load-independent for various other circuit topologies.

1.2 Research Work

This thesis presents a high-frequency load-independent resonant circuit, including an inverter, power oscillator, and synchronous rectifier. A summary of contributions in this thesis is as follows.

First, the load-independent class-E^{-1} and class-Φ_3 inverters are proposed. The circuit analysis reveals the load-independent design conditions. As the common feature of the load-independent inverters, additional degrees of design freedom to achieve the load-independent operation are obtained by introducing a new resonant structure within the circuit. Additionally, this research demonstrates that the load-independent operation can also be feasible for Zero-Current Switching (ZCS) and constant-current amplitude. Therefore, the applicability of the load-independent inverter is further broadened. The load-independent class-E^{-1} inverter is experimentally applied to a WPT system. The load-independent operation eliminates the need for feedback communication from the secondary side to the primary side in WPT systems, thereby facilitating the simplification of high-frequency circuit design.

Second, the load-independent class-E^{-1} and class-E power oscillators are proposed. In order to achieve load-independent operation in the power oscillator, both the phase condition for sustained oscillation and the load-independent condition must be simultaneously satisfied. This study demonstrates that both conditions can be met by providing feedback from the resonant capacitor in the load-independent constant-current inverter. The proposed feedback network also makes the gate-drive voltage of the power oscillator independent of the load resistance. Consequently, the load-

independent power oscillator gains robustness, achieving high efficiency and stable oscillation against load variations.

Third, the load-independent class-E synchronous rectifier is proposed. The load-independent operation in the rectifiers requires synchronous rectification. In this research, the load-independent rectifier is realized by utilizing the time-reversal duality between power oscillators and synchronous rectifiers. The proposed synchronous rectifier is highly suitable for the secondary-side circuit of high-frequency WPT systems because it requires no auxiliary power supply or control circuits. Experimental validation is conducted on a WPT system using the load-independent class-E inverter as the transmitter, demonstrating the effectiveness of the proposed rectifier.

1.3 Thesis Outline

Chapter 2 will introduce the basic high-frequency circuits, including class-E inverter (Section 2.1), class-E rectifier (Section 2.2), class-E power oscillator (Section 2.3), and class-E synchronous rectifier (Section 2.4). The circuit topologies, operating principles, and relationships between the circuits are explained. Additionally, the load-independent class-E inverter is also introduced in Section 2.5. This section discusses the challenge of load sensitivity in the class-E inverters and how the load-independent class-E inverter has been addressed. The graphical outline of this thesis is shown in Fig. 1.1.

Chapter 3 presents a load-independent inverse class-E inverter, which essentially produces a sinusoidal output current even with a low-Q series resonant filter. Be-

sides, the proposed inverter achieves ZCS and constant current output simultaneously, regardless of the load resistance. The experiment was carried out with a WPT system incorporating the proposed inverter as a transmitter and the class-D rectifier as a receiver. Although the input reactance of the class-D rectifier changed against DC-load variations due to the parasitic capacitances, the proposed inverter showed consistent, constant current operation by using the low-Q series resonant filter. Also, the proposed WPT system maintained a low total harmonic distortion of the transmission current over the wide load range, even with the low-Q output filter.

Chapter 4 presents a load-independent class-Φ_3 resonant inverter. The class-Φ_3 inverter is analyzed and reveals that the feasibility of load-independent operation in the class-Φ_3 operation is revealed. The load-independent class-Φ_3 inverter achieves the ZVS and a constant output-voltage amplitude regardless of the load resistance. The design conditions for achieving the load-independent operation are analytically described in this chapter. The experiment verifications were carried out to confirm the validity of the proposed design.

Chapter 5 presents a load-independent self-tuned series resonant power oscillator. The proposed power oscillator is derived from the load-independent inverse class-E inverter presented in Chapter 3. The proposed power oscillator achieves constant current output and high efficiency against load-resistance variations and component tolerances by adding the self-tuned feedback network. The design method of the proposed oscillator is presented in this chapter. The experimental results show the effectiveness of the proposed power oscillator.

Chapter 6 presents a load-independent class-E power oscillator. The load-independent

class-E inverter is incorporated into the power oscillator by introducing the feedback network using the LCCL filter. The LCCL filter compensates for the phase shift between the output and gate-drive voltages of the load-independent class-E inverter. Furthermore, the input impedance of the LCCL filter becomes purely resistive, which does not interfere with the load-independent operation of the inverter. Consequently, the proposed power oscillator obtains load independence in ZVS, output current, and gate-drive voltage. The proposed circuit works with high stability and efficiency over a wide load range, overcoming the sensitivity issue against load variations in the power oscillator. An analytical investigation of the proposed power oscillator is provided to reveal design conditions for achieving the load-independent operation. The experimental verifications were carried out at 6.78 MHz oscillation frequency.

Chapter 7 presents a load-independent class-E synchronous rectifier with a passive feedforward network. The proposed rectifier generates the synchronized drive voltage using the voltage across the resonant capacitor. Therefore, additional phase-detection circuits and digital devices are not required for the synchronous rectification. Moreover, the proposed synchronous rectifier achieves the ZVS and constant output voltage against load variations. The validity and effectiveness of the proposed rectifier are confirmed by the experiment.

Chapter 8 shows the conclusion of this thesis. Additionally, future research topics are introduced in this section.

ries Resonant Power Amplifier With Constant Current Output and Its Application for WPT System", IEEE Transactions on Power Electronics, May 2024. Chapters 4 is based on reference [14]. Chapters 5 is based on reference [15].

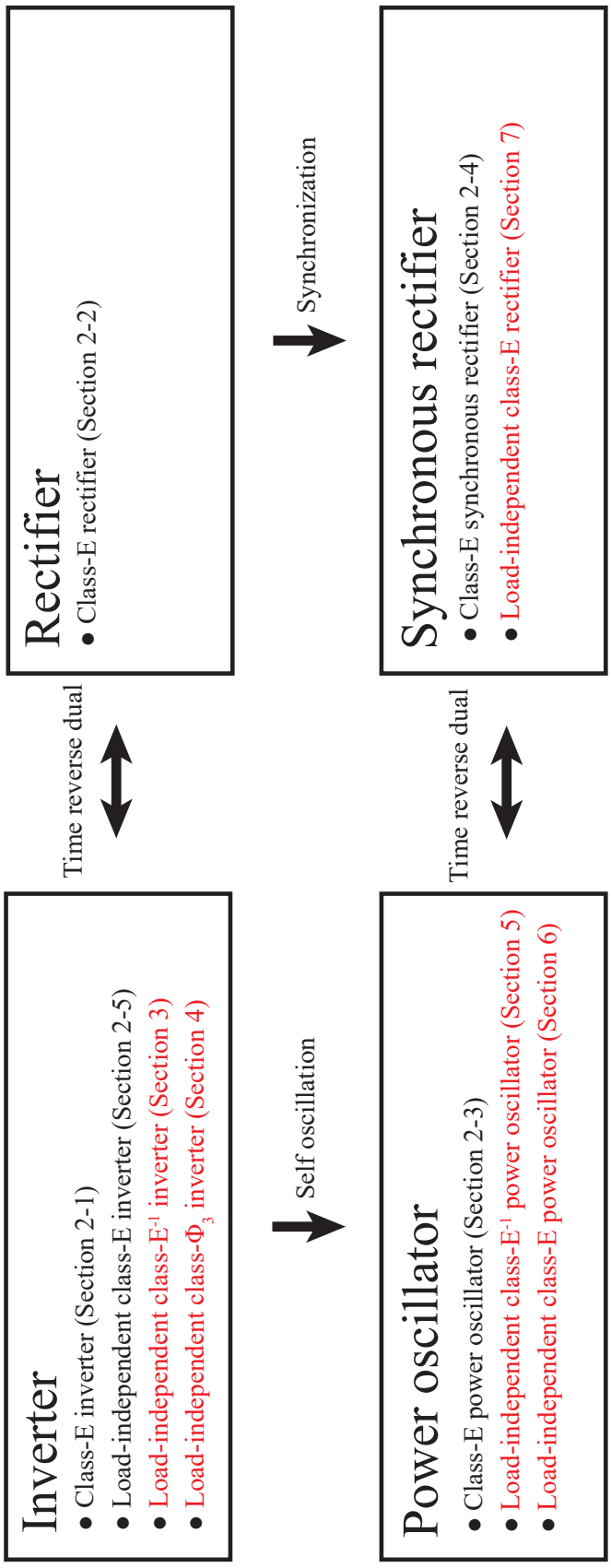

Fig. 1.1: Outline of this thesis. (black characters show the conventional research, and red characters show my proposal.)

References

[1] B. J. Baliga, "Trends in power semiconductor devices," in IEEE Transactions on Electron Devices, vol. 43, no. 10, pp. 1717-1731, Oct. 1996.

[2] L. H. Walker, "10-MW GTO converter for battery peaking service," in IEEE Transactions on Industry Applications, vol. 26, no. 1, pp. 63-72, Jan.-Feb. 1990.

[3] R. H. Dennard, F. H. Gaensslen, H. -N. Yu, V. L. Rideout, E. Bassous and A. R. LeBlanc, "Design of ion-implanted MOSFET's with very small physical dimensions," in IEEE Journal of Solid-State Circuits, vol. 9, no. 5, pp. 256-268, Oct. 1974.

[4] B. Lu and S. K. Sharma, "A Literature Review of IGBT Fault Diagnostic and Protection Methods for Power Inverters," in IEEE Transactions on Industry Applications, vol. 45, no. 5, pp. 1770-1777, Sept.-oct. 2009.

[5] J. Millán, P. Godignon, X. Perpiñà, A. Pérez-Tomás and J. Rebollo, "A Survey of Wide Bandgap Power Semiconductor Devices," in IEEE Transactions on Power Electronics, vol. 29, no. 5, pp. 2155-2163, May 2014.

[6] Global market insights, Semiconductors and electronics, [Online]. Available: https://www.gminsights.com/ja/industry-analysis/sic-and-gan-power-semiconductor-market, Accessed on. Feb. 10, 2025.

[7] N. O. Sokal and A. D. Sokal, "Class E-A new class of high-efficiency tuned single-ended switching power amplifiers," in IEEE Journal of Solid-State Circuits, vol. 10, no. 3, pp. 168-176, June 1975.

[8] M. K. Kazimierczuk, "Analysis of class E zero-voltage-switching rectifier," in IEEE Transactions on Circuits and Systems, vol. 37, no. 6, pp. 747-755, June 1990.

[9] M. K. Kazimierczuk and K. Puczko, "Class E low dv/dt synchronous rectifier with controlled duty ratio and output voltage," in IEEE Transactions on Circuits and Systems, vol. 38, no. 10, pp. 1165-1172, Oct. 1991.

[10] J. Ebert and M. Kazimierczuk, "Class E high-efficiency tuned power oscillator," in IEEE Journal of Solid-State Circuits, vol. 16, no. 2, pp. 62-66, April 1981.

[11] A. Ghahremani, A. -J. Annema and B. Nauta, "Load Mismatch Sensitivity of Class-E Power Amplifiers," in IEEE Transactions on Microwave Theory and Techniques, vol. 67, no. 1, pp. 216-230, Jan. 2019.

[12] R. E. Zulinski and K. J. Grady, "Load-independent class E power inverters. I. Theoretical development," in IEEE Transactions on Circuits and Systems, vol. 37, no. 8, pp. 1010-1018, Aug. 1990.

[13] Y. Komiyama, A. Komanaka, W. Zhu, A. Konishi, K. Nguyen and H. Sekiya, "Analysis and Design of Load-Independent Series Resonant Power Amplifier With Constant Current Output and Its Application for WPT System," IEEE Transactions on Power Electronics, vol. 39, no. 5, pp. 6515-6525, May 2024.

[14] Y. Komiyama, W. Zhu, A. Konishi, K. Nguyen, and H. Sekiya, "Design of Load-Independent Class-Φ 3 Resonant Inverter", IEEE Energy Conversion Congress and Exposition (ECCE), Phoenix, AZ, USA, Oct. 2024. (Accepted)

[15] Y. Komiyama, W. Zhu, A. Komanaka, X. Wei, K. Nguyen, and H. Sekiya, “ Self-tuned series resonant power oscillator with load-independent operation, ” IEEE International Symposium on Circuits and Systems (ISCAS), Monterey, CA, USA, May 2023, pp. 1-5.

Chapter 2

High-Frequency Resonant Circuits

●● ABSTRACT ●●

This chapter will provide background knowledge on high-frequency resonant circuits. The class-E resonant circuits are introduced as the representative of the high-frequency resonant circuits. Circuit topologies and operation principles of the class-E inverter, class-E rectifier, class-E power oscillator, and class-E synchronous rectifier are presented. Additionally, the relationships between them are described. Also, this chapter discusses the common challenge of the class-E resonant circuits, which is the sensitivity against load variations. Finally, the load-independent class-E inverter, which enhances the robustness against load variations, is introduced.

2.1 Class-E Inverter

2.1.1 Circuit Topology

Fig. 2.1(a) shows the circuit topology of the class-E inverter [1]. The class-E inverter is composed of the input voltage V_I, input-choke inductor L_1, switching device S, shunt capacitor C_1, series-resonant filter L_2-C_2, and load resistance R_L.

One of the reasons that the class-E inverter is suitable for high-frequency operation is its topological simplicity. The class-E inverter is driven with a signle switch, whose source terminal is grounded. Therefore, no high-side drive is required. Additionally, the innovative aspect of the class-E topology, compared with the class-D inverters, is that it uses an external shunt capacitor. In general, the switching loss increases in proportion to the drain-source capacitance. Hence, the circuit designers used to select the switching device with low output capacitance for class-D inverters. Nevertheless, Sokal deliberately added the drain-source capacitance to absorb the parasitic capacitance of the switching device [1].

2.1.2 Operating Principle

The class-E inverter achieves high efficiency even in high frequency because of the zero-voltage switching (ZVS) and the zero-derivative switching (ZDS), formulated as

$$v_S(2\pi D) = 0, \tag{2.1}$$

and

$$\left.\frac{dv_S(\theta)}{d\theta}\right|_{\theta=2\pi D} = 0, \tag{2.2}$$

respectively, where D is the OFF-duty ratio, $\theta = 2\pi ft$ represents the angular time, and f is the operating frequency. This specific switching condition is called the class-E switching, which is the definition of the class-E inverter. The class-E switching can be achieved for a unique set of component values, including shunt capacitance, load resistance, and extra load inductance.

Fig. 2.1(b) shows the typical waveforms of the class-E inverter. The input-choke inductance eliminates the ripple current, producing a current source. The switching device turns ON and OFF periodically, with a fixed duty ratio. The switch voltage v_S achieves turn-ON ZVS and ZDS, contributing to reducing the switching loss. The series-resonant filter extracts a fundamental frequency component from the switch voltage, generating the sinusoidal output voltage in the load resistance.

2.2 Class-E Rectifier

2.2.1 Circuit Topology

Fig. 2.2(a) shows the circuit topology of the class-E rectifier [2]. The class-E rectifier is composed of the input AC voltage $\dot{V}_{in}$, series-resonant filter L_1-C_1, rectification diode D, shunt capacitor C_1, output-choke inductor L_1, filter capacitor C_f, and load resistance R_L.

The class-E rectifier has a rectification diode instead of the switching device in the class-E inverter. This is because the turn-OFF class-E switching can be auto-

matically achieved using the diode. The diode turns OFF when the switch current becomes zero, resulting in the automatic turn-OFF ZDS. Besides, the continuity of the switch voltage allows the turn-OFF ZVS. Accordingly, the turn-ON ZVS is also ensured for a set of component values that satisfies the class-E switching condition.

2.2.2 Operating Principle

Fig. 2.2(b) shows the typical waveforms of the class-E rectifier. The class-E rectifier has a time-reversed duality against the class-E inverter. Namely, the waveforms of the class-E rectifier completely agree with the class-E inverter by replacing the angular time θ to $-\theta$. Therefore, the AC to DC rectification, which is the reverse operation of the inverter, can be realized.

2.3 Class-E Power Oscillator

2.3.1 Circuit Topology

Fig. 2.3(a) shows the circuit topology of the class-E power oscillator [3]. The class-E power oscillator consists of the class-E inverter and the passive feedback network. The passive feedback network is composed of the capacitors C_3 and C_4, inductor L_3, and the voltage-device resistances R_1 and R_2.

The class-E power oscillator is a variant of the class-E inverter, which autonomously oscillates by adding a passive feedback network. The class-E power oscillator generates the gate-drive voltage using the output AC voltage. Therefore, the feedback network needs to compensate for the phase shift between the output and gate-drive

voltages. The class-E power oscillator works without the gate-drive circuits, including a crystal oscillator, gate driver, and additional power supplies, which further promotes circuit simplification and cost reduction.

2.3.2 Operating Principle

Fig. 2.3(b) shows the typical waveforms of the class-E power oscillator. The switch is driven by the excitation of the biased sinusoidal voltage v_{gs}, which is generated using the output AC voltage v_O. To induce the sustained oscillation, the total phase shift in the closed loop must be an integer multiple of 2π. Meanwhile, the nominal phase shift of the output voltage is 0.82π in the class-E inverter. Therefore, the feedback network C_3-C_4-L_3 provides an additional phase shift, compensating the phase shift between the output and the gate-drive voltages. Additionally, the class-E power oscillator features to achieve the ZVS at the nominal state, which contributes to high-efficiency operation.

2.4 Class-E Synchronous Rectifier

Fig. 2.4(a) shows the circuit topology of the class-E synchronous rectifier [4]. The class-E synchronous rectifier uses the switching device instead of the rectification diode in the class-E rectifier.

The main purpose of using the switching device instead of the diode is to increase the power-conversion efficiency. In general, the diode has higher conduction losses than the switching device due to the ON resistance and forward voltage drop.

Therefore, active switches can reduce heat dissipation in the device and improve the overall efficiency.

The operating waveforms are exactly the same as the class-E rectifier, shown in Fig. 2.2(b). To achieve synchronous rectification, the switching device needs to turn OFF when the switch current becomes zero.

2.5 Load-Independent Class-E Inverter

2.5.1 Challenge in Class-E Resonant Circuits

The class-E resonant circuits, including inverter, power oscillator, and rectifier, are suitable for high-frequency operation. However, they are highly sensitive to load variations. The class-E switching can be satisfied for a specific parameter set, including the load resistance. Therefore, even a small change in the load resistance causes significant performance deterioration. The ZVS cannot be maintained, and power-conversion efficiency decreases against load variations. In addition, the output voltage and current fluctuate depending on the load resistance. Therefore, power and efficiency management is an essential challenge in the class-E resonant circuits.

2.5.2 Circuit Topology

Fig. 2.5(a) shows the circuit topology of the load-independent class-E inverter [5]. There is no topological difference between the load-independent and original class-E inverters. However, the load-independent class-E inverter uses finite-input inductance instead of the choke inductance.

The load-independent class-E inverter achieves the ZVS regardless of the load resistance. This feature can be enabled by the introduction of the finite-input inductance. In the original class-E inverter, there is no current path to discharge the shunt capacitor under light load conditions, leading to turn-on non-ZVS. In contrast, the load-independent class-E inverter introduces a large ripple in the input current, providing a current path for discharging the shunt capacitor to the input side.

Additionally, the load-independent class-E inverter inherently has a constant voltage gain against load variations. Therefore, no additional control is required to satisfy the output regulation.

2.5.3 Operating Principle

Fig. 2.5(b) shows the typical waveforms of the load-independent class-E inverter. The input current i_1 has a large ripple because of the resonance between L_1 and C_1 during the turn-OFF period. The resonant frequency between L_1 and C_1 is slightly higher than the operating frequency. The switch voltage v_S achieves the ZVS, and output voltage v_O has constant amplitude against load variations.

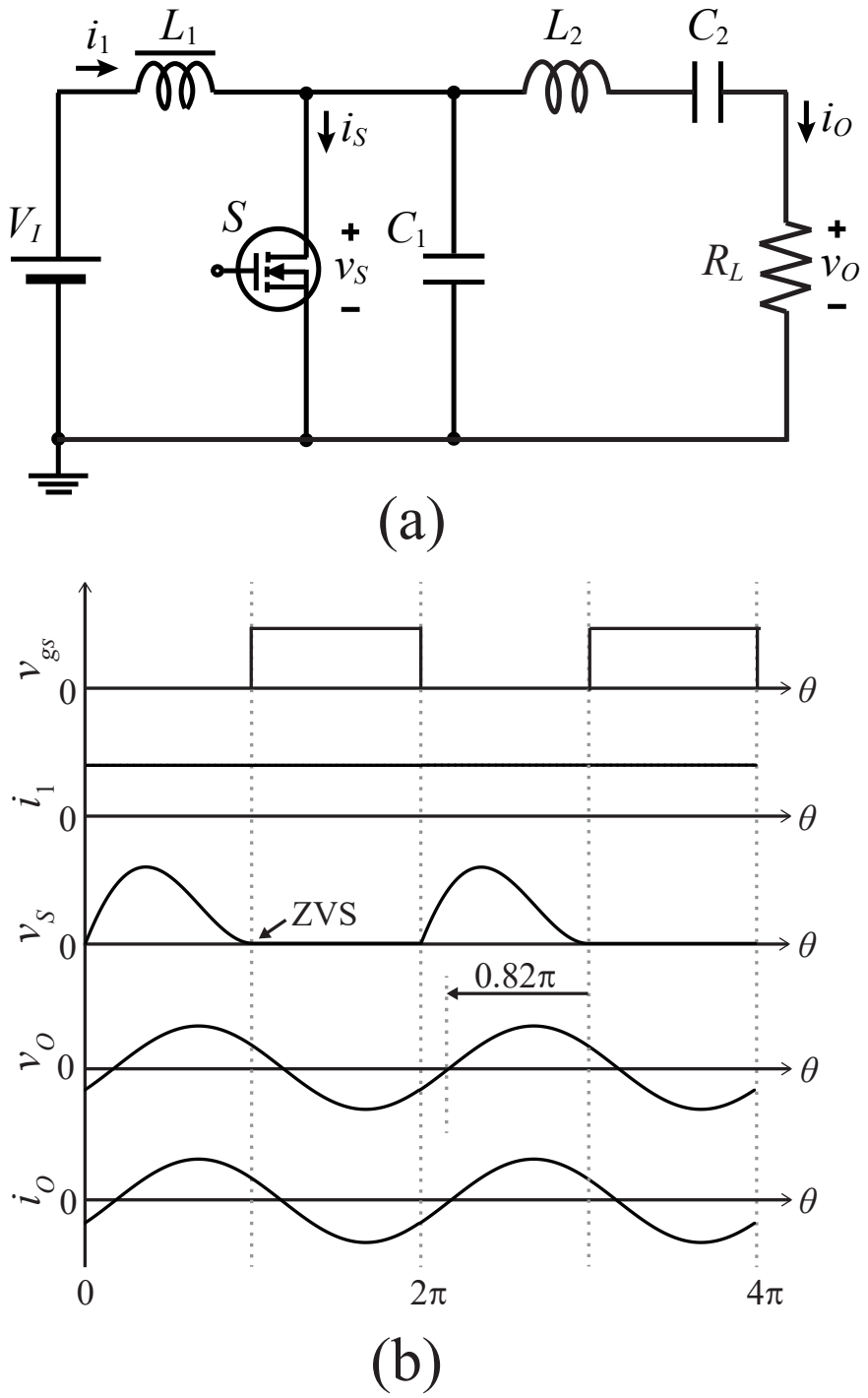

Fig. 2.1: Class-E inverter. (a) Circuit topology. (b) Typical waveform.

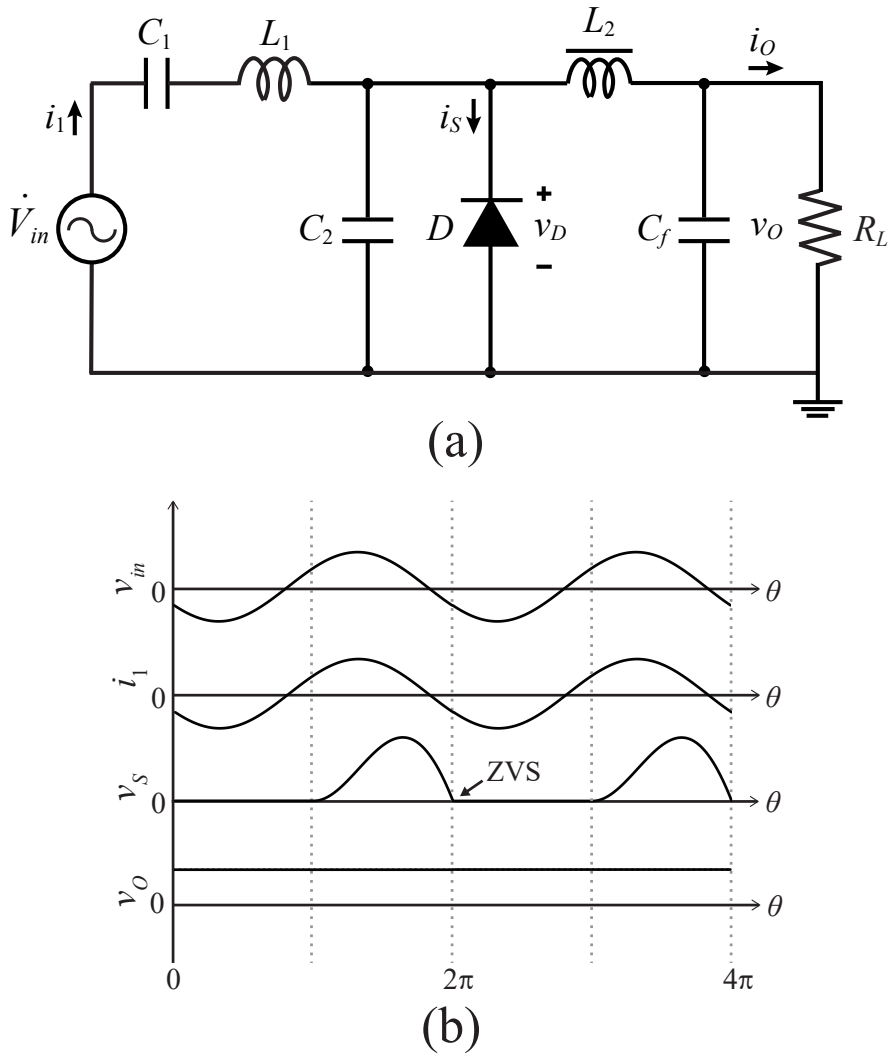

Fig. 2.2: Class-E rectifier. (a) Circuit topology. (b) Typical waveform.

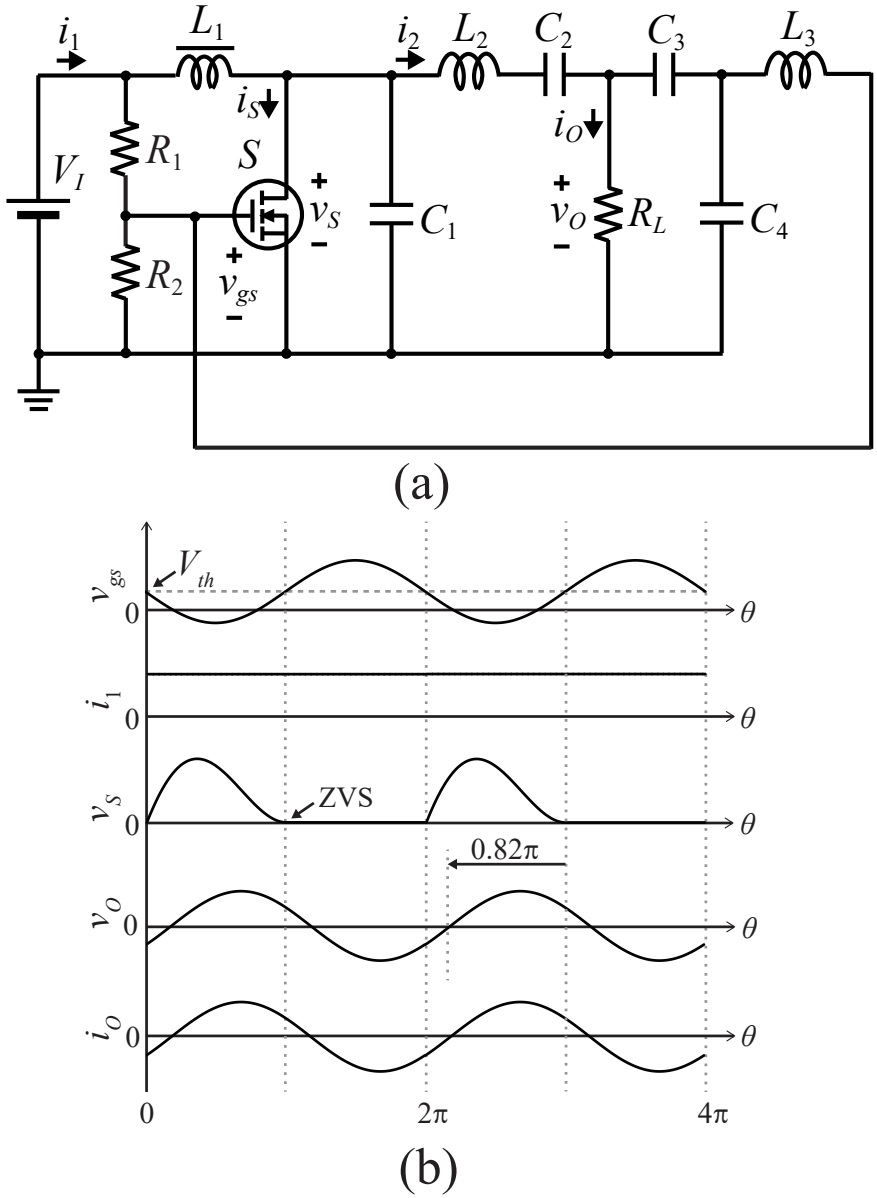

Fig. 2.3: Class-E power oscillator. (a) Circuit topology. (b) Typical waveform.

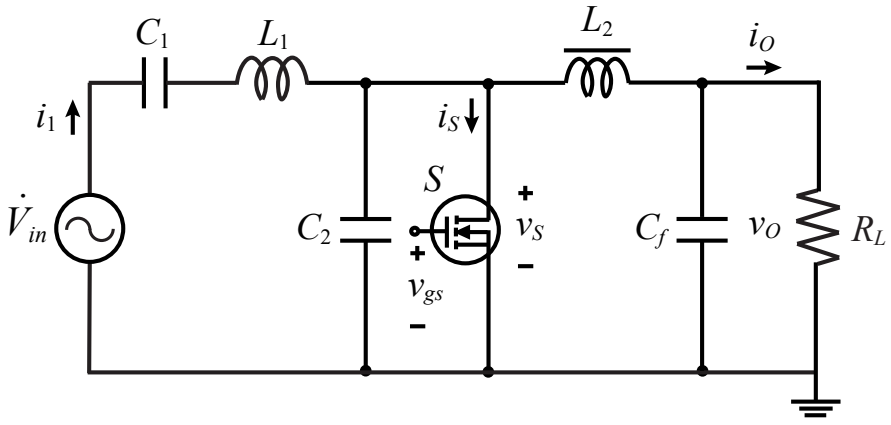

Fig. 2.4: Circuit topology of the synchronous class-E rectifier.

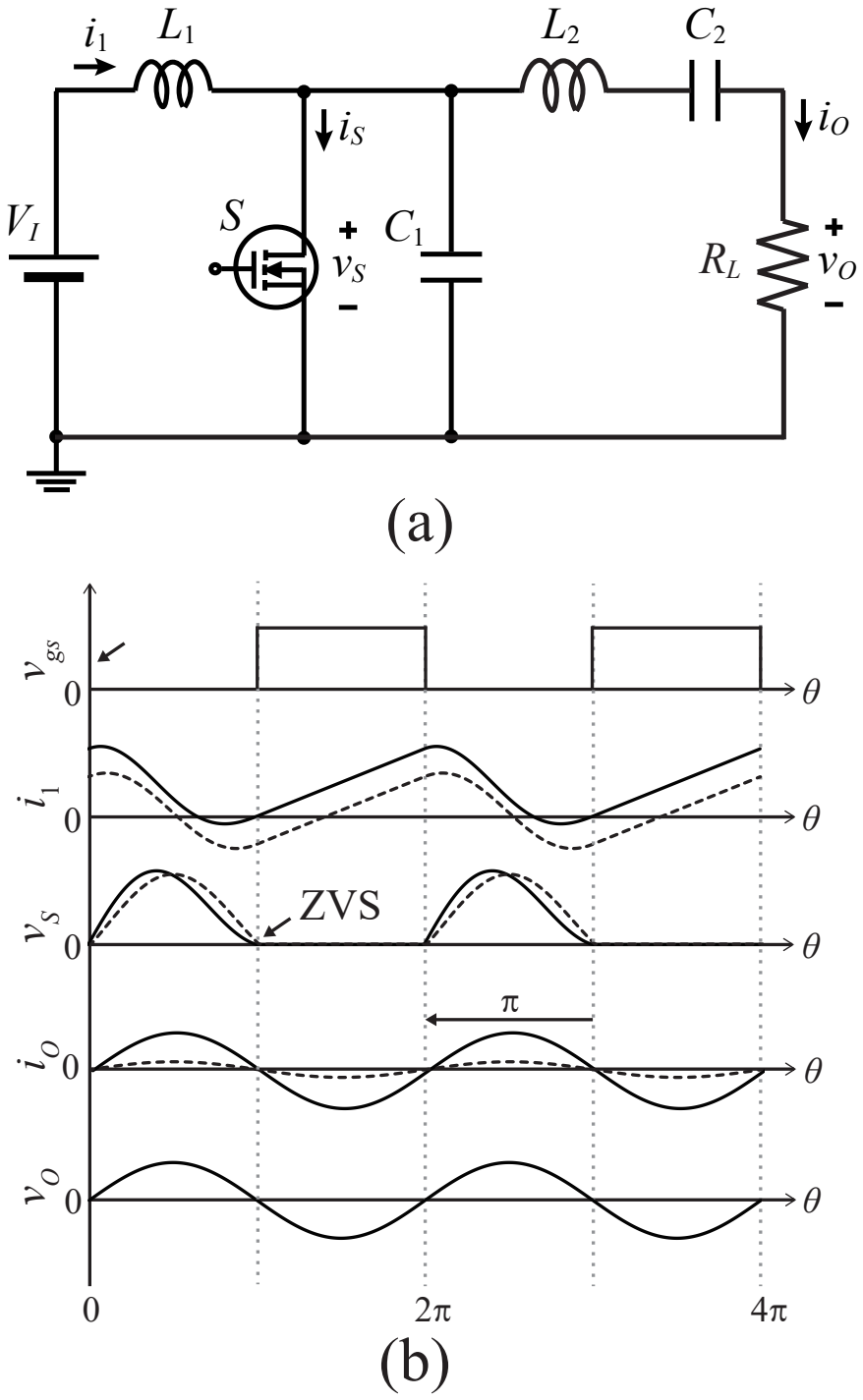

Fig. 2.5: Load-independent class-E inverter. (a) Circuit topology. (b) Typical waveform. (solid line: rated load condition, dashed line: varied load condition.)

References

[1] N. O. Sokal and A. D. Sokal, "Class E-A new class of high-efficiency tuned single-ended switching power amplifiers," in IEEE Journal of Solid-State Circuits, vol. 10, no. 3, pp. 168-176, June 1975.

[2] M. K. Kazimierczuk, "Analysis of class E zero-voltage-switching rectifier," in IEEE Transactions on Circuits and Systems, vol. 37, no. 6, pp. 747-755, June 1990.

[3] J. Ebert and M. Kazimierczuk, "Class E high-efficiency tuned power oscillator," in IEEE Journal of Solid-State Circuits, vol. 16, no. 2, pp. 62-66, April 1981.

[4] M. K. Kazimierczuk and K. Puczko, "Class E low dv/dt synchronous rectifier with controlled duty ratio and output voltage," in IEEE Transactions on Circuits and Systems, vol. 38, no. 10, pp. 1165-1172, Oct. 1991.

[5] R. E. Zulinski and K. J. Grady, "Load-independent class E power inverters. I. Theoretical development," in IEEE Transactions on Circuits and Systems, vol. 37, no. 8, pp. 1010-1018, Aug. 1990.

Chapter 3

Load-Independent Class-E^{-1} Inverter With Constant Current

3.1 Introduction

High performance power semiconductor devices, such as GaN and SiC devices, have enabled the high-frequency and high-efficiency operation of inverters [1–3]. The inverters at the megahertz frequency band are explored and developed, reducing the size and weight of the passive components. Meanwhile, high-frequency operation brings challenges, including growing switching losses and difficulty in high-side gate drives. Thus, the class-E inverter family, including class-E [1–14], class-EF [15–17], and class-Φ inverters [18,19], have attracted attention due to its simple configuration and soft switching feasibility. However, the class-E inverters are essentially sensitive against load variations [5, 6]. The load variations change the circuit operation drastically, causing output voltage variations and efficiency degradation due to hard switching.

To overcome the sensitivity, a load-independent class-E inverter was proposed [7], which enhances the robustness against load variations. The load-independent class-

E inverter uses a finite input coil, which works as a resonant inductance. Namely, the load-independent class-E inverter expands the design flexibility to obtain robustness by introducing a new resonant structure. The load-independent class-E inverter maintains soft switching against load variations. Additionally, the amplitude of the output AC voltage is constant regardless of the load resistance. The robustness can be obtained by a specific tuning of component values without additional controls [8] and circuitry [9]. The design technique of the load-independent class-E inverter has also been applied to various circuit topologies in the class-E inverter family [11–21]. Depending on the circuit topology, the load-independent inverters inherently exhibit different characteristics in output types (constant current: CC or constant voltage: CV), soft switching (ZVS or ZCS), and output-resonant filters (series resonant: SR or parallel resonant: PR). Accordingly, the load-independent inverters can be adapted to a wide range of applications and specifications, such as DC-DC converters [13] and the transmitter of WPT systems [15–17]. Especially for WPT applications, the CC output inverter with the SR output filter is preferable. This is because it avoids overcurrents flowing through the transmitter coil even when the receiver circuit moves away.

Owing to the CC-SR feature, the load-independent class-EF inverter has proven successful in applications as a transmitter for WPT systems [15–17]. Additionally, the class-EF inverter mitigates switch-voltage stress by adding a harmonic resonant branch. In the original class-EF_2 and class-E/F_3 inverters [22–24], the harmonic resonant filter is tuned to an integer multiple of the switching frequency. On the other hand, the load-independent class-EF inverter employs a resonant frequency approximately 1.7 times the switching frequency [15]. This design, however, leads to

significant harmonic distortion in the output current because the harmonic resonant branch cannot fully filter out the harmonics [25]. The high total harmonic distortion (THD) of the current degrades electromagnetic interference (EMI) performance [26] and efficiency [27]. Furthermore, the harmonics in the output current deteriorate the consistency of the CC operation. Therefore, it is important to develop another CC-SR inverter topology with a low THD output current.

This chapter presents an analysis and design of the load-independent SR inverter with CC output. A novel circuit topology with CC-SR property is introduced, which can inherently output sinusoidal current even with a low-Q SR filter. Analytical design equations of the proposed inverter are provided, which allows a quick and intuitive component-value selection. This chapter also presents the design procedure and experiment for the WPT system incorporating the proposed inverter as the transmitter. The experimental verifications were conducted with the WPT system with the proposed inverter. The proposed inverter achieved superior consistency of the CC operation and a lower THD transmission current compared with the load-independent class-EF inverter. Furthermore, the proposed inverter showed low sensitivity to reactance components because it can produce sufficiently pure sinusoidal wave even with the low-Q SR filter. The experimental results showed the validity of the inverter design and analysis.

3.2 Load-Independent Inverter With CC-SR Property

This section provides a brief review of the load-independent class-EF inverter [15] and introduces the proposed inverter. These inverters have a common feature in the CC-SR property.

3.2.1 Load-Independent Class-EF Inverter

Fig. 3.1(a) and 3.1(b) show the circuit topology and example waveforms of the load-independent class-EF inverter, respectively, where D is the on-duty ratio, $\theta = \omega t = 2\pi f t$ is the angular displacement, ω denotes the angular switching frequency, and f is the switching frequency. Besides, the subscript 'r' of the symbol means its rated value.

The load-independent class-EF inverter achieves ZVS and a constant amplitude output current simultaneously, regardless of the load resistance R, as shown in Fig. 3.1(b). The load-independent operation is obtained for a specific set of component values, which is determined by satisfying the design conditions of [15]

$$\frac{dI_m}{dR} = 0, \tag{3.1}$$

and

$$v_S(2\pi D) = 0, \tag{3.2}$$

where I_m is the amplitude of the output current i. The condition (3.1) represents the CC operating condition, and (3.2) shows the ZVS condition. By satisfying (3.1)

and (3.2) simultaneously, the design parameters for the load-independent operation are derived. Therefore, the class-EF inverter only requires specific tuning to obtain robustness against load variations without requiring additional controls and circuits.

However, the load-independent class-EF inverter introduces significant harmonic distortion into the output current. This is because the resonant frequency of L_h-C_h needs to be tuned to approximately 1.7 times the switching frequency, and thus, the harmonic current cannot be fully filtered out by L_h-C_h.

Although the harmonics in the output current can be reduced by using a high-Q SR filter, it results in higher sensitivity, a large inductance, and increased voltage stress and power losses for the resonant components. Also, the push-pull topology is effective for suppressing second-order harmonics. It has a tradeoff against the increase in device and component numbers and accurate tuning for circuit balance.

3.2.2 Proposed Inverter

Fig. 3.2(a) shows the circuit topology of the proposed inverter, which consists of the DC-input voltage source V_I, choke inductance L_C, series inductance L_S, switching device S, shunt capacitance C_S, SR filter L_0-C_0, and load resistance R. Fig. 3.2(b) depicts the example waveforms of the proposed inverter for fixed load resistances.

The choke inductance L_C sufficiently reduces the ripple current and behaves as a DC-current source. The switching device turns on and off periodically. During the turn-on period, current flows into the switching device, which achieves ZCS at the turn-off moment, as shown in Fig. 3.2(b). The ZCS is a dual operation

of the ZVS in the class-E inverters [28]. Namely, the proposed inverter can be called load-independent inverse class-E inverter. The L_S and C_S resonate at slightly higher than the switching frequency, and the nearly sinusoid voltage appears across the capacitor C_S. The output voltage is generated by extracting a fundamental frequency component from the voltage across C_S through the SR output filter.

The proposed inverter exhibits robustness against resistive load variations. Namely, the ZCS is maintained regardless of the load resistance, resulting in high-efficiency operation over the wide load range. Also, the amplitude and phase shift of the output current is independent of the load resistance. The output currents for $R/R_r = 1$ and $R/R_r = 0.1$ are completely overlapped in Fig. 3.2(b).

The proposed inverter no longer requires a high-Q SR filter because v_{C_S} exhibits inherently close to the sinusoidal waveform. Also, a sufficiently pure sinusoidal output can be obtained even without the SR filter. In the design without the SR filter, C_0 only works as a DC blocking with a large capacitance, while L_0 works as the phase-shift inductance required for the load-independent design. One major advantage of applying the low-Q SR filter is that the proposed inverter obtains robustness against reactance component variations.

3.3 Analysis of Proposed Inverter

This chapter provides the waveform expressions, inverter characteristics, and design equations of the proposed inverter. The analysis is conducted under the following assumptions.

1. The choke inductance L_C is large enough so that the input current I_I can be regarded as DC.
2. The switching device operates ideally. Namely, the switching time, parasitic capacitances, on-resistance, and threshold voltage are zero, and off-resistance is infinite. Besides, the switch turns on during $0 \leq \theta < 2\pi D$, and turns off during $2\pi D \leq \theta < 2\pi$.
3. The resonant inductance L_0 is devided into a resonant component L_a and an extra-inductive component L_b. The L_a and C_0 resonate at the switching frequency, namely

$$\frac{1}{\omega\sqrt{L_a C_0}} = 1. \tag{3.3}$$

   Additionally, the quality factor of the SR output filter $Q = \omega L_0/R$ is high enough so that the output current can be regarded as a pure sine wave as

$$i(\theta) = I_m \sin(\theta + \varphi), \tag{3.4}$$

   where φ is the phase shift from gate-drive voltage defined as shown in Fig. 3.2(b), and I_m is the amplitude of the output current.
4. All the passive component works linearly with no parasitic components.

In the analysis, the dimensionless circuit parameters are used to provide a generalized discussion. The voltage and current are normalized by input voltage V_I and rated load resistance R_r, as like

$$v^* = \frac{v}{V_I}, \quad \text{and} \quad i^* = \frac{R_r i}{V_I}. \tag{3.5}$$

Besides, the component parameters are also normalzied by ω and R_r, as like

$$\lambda_S = \frac{\omega L_S}{R_r}, \quad \gamma_S = \frac{1}{\omega C_S R_r}, \quad \text{and} \quad \rho = \frac{R}{R_r}. \tag{3.6}$$

Fig. 3.3 shows the analytical model of the proposed inverter.

3.3.1 Waveform Derivation

During the switch turn-on period of $0 \leq \theta < 2\pi D$, a second-order differential equation for switch current i_S^* is obtained using KCL as

$$\frac{d^2 i_S^*(\theta)}{d\theta^2} + {\omega_S^*}^2 i_S^*(\theta) = {\omega_S^*}^2 [I_I^* - I_m^* \sin(\theta + \varphi)], \tag{3.7}$$

where I_I^* is the normalized input current and ω_S^* is defined as

$$\omega_S^* = \sqrt{\frac{\gamma_S}{\lambda_S}}. \tag{3.8}$$

By solving (3.7), the switch current for $0 \leq \theta < 2\pi D$ can be obtained as

$$\begin{aligned} i_S^*(\theta) =& A\cos(\omega_S^*\theta) + B\sin(\omega_S^*\theta) \\ & - \frac{{\omega_S^*}^2 I_m^*}{{\omega_S^*}^2 - 1}\sin(\theta + \varphi) + I_I^*, \quad \text{for } 0 \leq \theta < 2\pi D, \end{aligned} \tag{3.9}$$

where A and B are constants. Besides, the voltage across γ_S is derived by integrating the current flowing through it as

$$\begin{aligned} v_{C_S}^*(\theta) =& \gamma_S^* \int_0^\theta I_I^* - i_S^*(\theta') - I_m^* \sin(\theta' + \varphi) d\theta' \\ =& -\lambda_S \omega_S^* \Bigg[A\sin(\omega_S^*\theta) - B\cos(\omega_S^*\theta) \\ & + \frac{\omega_S^* I_m^*}{{\omega_S^*}^2 - 1}\cos(\theta + \varphi) \Bigg], \quad \text{for } 0 \leq \theta < 2\pi D. \end{aligned} \tag{3.10}$$

During the switch turn-off period of $2\pi D \leq \theta < 2\pi$, the switch current becomes zero, namely

$$i_S^*(\theta) = 0, \quad \text{for } 2\pi D \leq \theta < 2\pi. \tag{3.11}$$

The expression of the voltage across shunt capacitance during the turn-off period, which is the same as the switch voltage, can be given by integrating the current flowing through γ_S as

$$\begin{aligned} v_{C_S}^*(\theta) =& v_S^*(\theta) = \gamma_S \int_{2\pi D}^{\theta} I_I^* - I_m^* \sin(\theta' + \varphi) d\theta'. \\ =& \gamma_S \{ I_I^*(\theta - 2\pi D) + I_m^* [\cos(\theta + \varphi) - \cos(2\pi D + \varphi)] \} \\ & - \lambda_S \omega_S^* \Bigg[A \sin(2\pi D \omega_S^*) - B \cos(2\pi D \omega_S^*) \\ & + \frac{\omega_S^* I_m^*}{{\omega_S^*}^2 - 1} \cos(2\pi D + \varphi) \Bigg], \quad \text{for } 2\pi D \leq \theta < 2\pi. \end{aligned} \tag{3.12}$$

Note that the boundary condition at $\theta = 2\pi D$ with (3.10) is taken into account in (3.12).

3.3.2 Boundary Condition

From the continuity of the current flowing through λ_S and the voltage across γ_S, we obtain the boundary conditions as

$$i_S^*(0) = i_S^*(2\pi), \tag{3.13}$$

and

$$v_{C_S}^*(0) = v_{C_S}^*(2\pi). \tag{3.14}$$

From (3.9)-(3.14), the constants A and B can be obtained as

$$A = \frac{\omega_S^{*2} I_m^*}{\omega_S^{*2} - 1} \sin\varphi - I_I^*, \tag{3.15}$$

and

$$\begin{aligned} B = & \left\{ \frac{\omega_S^* [\cos(2\pi D\omega_S^*) - (1 - 2\omega_S^{*2})\cos\varphi]}{(\omega_S^{*2} - 1)[1 - \cos(2\pi D\omega_S^*)]} \right. \\ & \left. - \frac{\omega_S^{*2} \sin\varphi \sin(2\pi D\omega_S^*)}{(\omega_S^{*2} - 1)[1 - \cos(2\pi D\omega_S^*)]} \right\} I_m^* \\ & + \frac{\pi\omega_S^* + \sin(2\pi D\omega_S^*)}{1 - \cos(2\pi D\omega_S^*)} I_I^*. \end{aligned} \tag{3.16}$$

3.3.3 Load-Independent Condition

The proposed inverter achieves ZCS at the turn-off instant, namely

$$i_S^*(2\pi D) = 0. \tag{3.17}$$

There is no power-loss factor in this analysis. Therefore, the input and output powers are equal. Hence, we have

$$1 \times I_I^* = \frac{\rho I_m^{*2}}{2}. \tag{3.18}$$

From (3.9), (3.17), and (3.18), the relationship between I_m^* and ρ is obtained as

$$\begin{aligned} & [\pi(1 - D)\omega_S^* \sin(2\pi D\omega_S^*) + 1 - \cos(2\pi D\omega_S^*)] I_m^* \rho \\ & - \frac{4\omega_S^{*2} \sin(\pi D + \varphi) \sin(\pi D\omega_S^*) \sin[\pi D(1 - \omega_S^*)]}{\omega_S^{*2} - 1} = 0. \end{aligned} \tag{3.19}$$

For achieving the CC output, I_m^* must be independent from ρ. This means that the coefficient of ρ and the constant term in (3.19) must be both zero. Thus, we have the load-independent-design conditions as

$$\pi(1 - D)\omega_S^* \sin(2\pi D\omega_S^*) + 1 - \cos(2\pi D\omega_S^*) = 0, \tag{3.20}$$

and

$$\varphi = \pi(1 - D). \tag{3.21}$$

By satisfying (3.20) and (3.21), the proposed inverter attains the ZCS and CC output regardless of the load resistance. Fig. 3.4 shows the normalized resonant angular frequency ω_S^* and phase shift φ that satisfy (3.20) and (3.21).

3.3.4 SR Output Filter

From the assumption, the SR output filter $\lambda_0 - \gamma_0$ passes only a fundamental frequency component from the voltage across γ_S. Namely, we obtain

$$v^*_{C_{S1}}(\theta) = \rho I^*_m \sin(\theta + \varphi) + \lambda_b I^*_m \cos(\theta + \varphi). \tag{3.22}$$

where $v^*_{C_{S1}}$ is the fundamental frequency component in $v^*_{C_S}$. By applying the Fourier Series Expansion for (3.22) and considering (3.20) and (3.21), we obtain

$$\begin{aligned} \rho I^*_m &= \frac{1}{\pi}\int_0^{2\pi} v^*_{C_S}(\theta)\sin(\theta+\varphi)d\theta \\ &= \frac{2\gamma_S {\omega^*_S}^2[\pi(1-D)\cos(\pi D) + \sin(\pi D)]}{\pi({\omega^*_S}^2 - 1)} I^*_I, \end{aligned} \tag{3.23}$$

and

$$\begin{aligned} \lambda_b I^*_m =& \frac{1}{\pi}\int_0^{2\pi} v^*_{C_S}(\theta)\cos(\theta+\varphi)d\theta \\ =& \frac{\gamma_S {\omega^*_S}^2}{\pi({\omega^*_S}^2 - 1)}\left\{\pi(1-D) + \frac{\sin(\pi D)}{2} - \frac{\pi}{{\omega^*_S}^2}\right. \\ &\left. + \frac{2\sin(\pi D)\left[\sin(\pi D) + \pi(1-D)\cos(\pi D)\right]}{\pi(1-D)({\omega^*_S}^2 - 1)}\right\} I^*_m. \end{aligned} \tag{3.24}$$

3.3.5 Inverter Characteristics

Fig. 3.5(a) and (b) show the normalized maximum switch voltage V^*_{Smax} and current I^*_{Smax} as functions of duty ratio D and normalized shunt capacitance γ_S. The V^*_{Smax} and I^*_{Smax} are obtained by computing the maximum value against θ using (3.12) and (3.9), respectively. It is seen from Fig. 3.5(a) that the normalized peak switch voltage decreases for lower D. Meanwhile, the low switch-current stress is attained for larger γ_S, as shown in Fig. 3.5(b).

Fig. 3.5(c) shows the power-output capability, which is defined as

$$c_p = \frac{\rho {I^*_m}^2}{2V^*_{Smax}I^*_{Smax}}. \tag{3.25}$$

It is seen from Fig. 3.5(c) that the maximum power-output capability $c_p = 0.102$ is obtained for $D = 0.481$ and $\gamma_S = 1.08$.

Fig. 3.6 shows the normalized extra-inductance λ_b and output current amplitude I^*_m as functions of duty ratio for fixed γ_S, which is depicted using (3.23) and (3.24). It can be seen from Fig. 3.6(b) that the output current amplitude is adjustable depending on D and γ_S. The design point that achieves the maximum power-output capability is obtained as $\lambda_b = 1.33$ and $I^*_m = 1.15$.

3.3.6 Circuit Design for Maximum Power-Output Capability

The proposed inverter is designed for given input voltage V_I, rated load resistance R_r, switching frequency f, and quality factor Q. The component values can be uniquely determined by satisfying (3.18), (3.20), (3.21), (3.23), and (3.24) for any D

and γ_S. The design equations for any D and γ_S, and the specific case of maximum power-output capability are derived as

$$C_S = \frac{1}{\omega\gamma_S R_r} = \frac{0.147}{fR_r}, \tag{3.26}$$

$$L_S = \frac{1}{\omega_S^{*2} C_S} = \frac{0.0977 \times R_r}{f}, \tag{3.27}$$

$$L_0 = \frac{QR_r}{\omega} = \frac{0.159 \times QR_r}{f}, \tag{3.28}$$

$$\begin{aligned} L_b =& \frac{\gamma_S \omega_S^{*2} R_r}{\pi\omega(\omega_S^{*2}-1)} \left\{ \pi(1-D) + \frac{\sin(\pi D)}{2} - \frac{\pi}{\omega_S^{*2}} \right. \\ & \left. + \frac{2\sin(\pi D)\left[\sin(\pi D) + \pi(1-D)\cos(\pi D)\right]}{\pi(1-D)(\omega_S^{*2}-1)} \right\} \\ =& \frac{0.212 \times R_r}{f}, \end{aligned} \tag{3.29}$$

and

$$C_0 = \frac{1}{\omega^2(L_0 - L_b)} = \frac{0.159}{fR_r(Q-1.33)}. \tag{3.30}$$

The amplitude of the output current is derived from (3.23) as

$$\begin{aligned} I_m &= \frac{\pi(\omega_S^{*2}-1)V_I}{\gamma_S \omega_S^{*2} R_r[\pi(1-D)\cos(\pi D) + \sin(\pi D)]} \\ &= \frac{1.15 \times V_I}{R_r}. \end{aligned} \tag{3.31}$$

3.3.7 Circuit Design for Reducing Switching Loss

The proposed inverter achieves ZCS regardless of the load resistance, reducing the current-related turn-off losses. However, in high-frequency operations, voltage-related turn-on losses become dominant. Therefore, design methods to reduce turn-on losses is provided in this section.

The turn-on switching loss can be given as

$$P_{SW} = \frac{1}{2} C_{OSS} V_S^2 f, \tag{3.32}$$

where C_{OSS} is the output capacitance of the switching device, and V_S is the switch voltage at turn-on instant. We can see from (3.32) that reducing V_S is effective for suppressing the turn-on loss.

Fig. 3.7 shows the example waveforms of the switch current and voltage. There are ringings in both switch current and voltage during the turn-off period, which is caused by the resonance between L_S and C_{OSS}. For reducing V_S, it is desirable to turn on the switch when the switch voltage drops completely, as shown in Fig. 3.7. Namely, the number of the ringings during the turn-off period should be an integer multiple as

$$n_S T_S = \frac{1-D}{f}, \tag{3.33}$$

where n_S is the number of the ringings, for example, $n_S = 3$ in Fig. 3.7. Besides, $T_S = 2\pi\sqrt{L_S C_{OSS}}$ represents a ringing period. From (3.33), the design value of the L_S can be obtained as

$$L_S = \frac{1}{C_{OSS}} \left(\frac{1-D}{\omega n_S} \right)^2. \tag{3.34}$$

The design equation of C_S can be

$$C_S = \frac{1}{\omega_S^{*2} L_S}. \tag{3.35}$$

The remaining component values can be determined using (3.28)-(3.30).

3.4 Application for WPT

This chapter introduces a WPT system using the proposed inverter as a concrete application example, along with a design procedure, power-loss analysis, and experiment. Furthermore, this chapter compares the performances of the proposed WPT system and the WPT system using the load-independent class-EF inverter [15].

3.4.1 System Configuration

Fig. 3.8 shows the circuit configurations of the WPT system with the load-independent class-EF and the proposed inverters, respectively. The load-independent class-EF and the proposed inverters are employed as transmitters. The current-driven class-D rectifier [29] is adopted for the receiver. The class-D rectifier consists of two diodes D_1 and D_2 with parasitic capacitances of C_{D1} and C_{D2}, smoothing capacitor C_f and load resistance R_L. The coupling section is of the series-to-series (S-S) type, and the transmitter coil L_1 and receiver coil L_2 are coupled with a coupling coefficient k.

3.4.2 Analytical Expressions of Proposed WPT System

The input impedance of the class-D rectifier is ideally pure resistive component [30]. However, in a high-frequency region, it becomes capacitive due to the parasitic capacitances of the diodes. When the parasitic capacitances C_{D1} and C_{D2} are considered, the input resistance and capacitance of the class-D rectifier can be

expressed as [31]

$$R_{rct} = \frac{[1 - \cos(2\pi D_{rct})]^2 R_L}{2\pi^2}, \tag{3.36}$$

and

$$C_{rct} = \frac{2\pi(C_{D1} + C_{D2})}{\sin(4\pi D_{rct}) + 2\pi(1 - 2D_{rct})}, \tag{3.37}$$

respectively, where

$$D_{rct} = \frac{1}{2\pi} \cos^{-1}\left[\frac{\omega(C_{D1} + C_{D2})R_L - 2\pi}{\omega(C_{D1} + C_{D2})R_L + 2\pi}\right], \tag{3.38}$$

is the diode on-duty ratio.

The impedance seen from the inverter is obtained as

$$Z_{inv} = \frac{\omega^2 k^2 L_1 L_2 R_{rct}}{R_{rct}^2 + \frac{1}{\omega^2 C_{rct}^2}} + j\omega\left[L_1 + \frac{k^2 L_1 L_2}{C_{rct}\left(R_{rct}^2 + \frac{1}{\omega^2 C_{rct}^2}\right)}\right], \tag{3.39}$$

under the complete resonance in the secondary side as

$$\frac{1}{\omega\sqrt{L_2 C_2}} = 1. \tag{3.40}$$

It can be seen from (3.39) that both the resistive and reactive parts depend on the load resistance R_L. Meanwhile, the proposed inverter has robustness even against reactive-component variations due to the low-Q SR filter.

From (3.39), the DC-output voltage of the WPT system with the proposed inverter is expressed as

$$V_O = \omega k I_m \sqrt{\frac{L_1 L_2 R_{rct} R_L}{2\left(R_{rct}^2 + \frac{1}{\omega^2 C_{rct}^2}\right)}} \tag{3.41}$$

We can see from (3.41) that the output voltage depends on the load resistance R_L. When we consider the case that the effect of the parasitic capacitance of the diode can be ignored, namely $R_{rct} \gg 1/(\omega C_{rct})$, the output voltage is derived from (5.7) and (3.41) as

$$V_O = \frac{\pi k \omega \sqrt{L_1 L_2}}{2} I_m = \frac{0.0677 \times R_{Lr} V_I}{k f \sqrt{L_1 L_2}}. \tag{3.42}$$

The parameter R_{Lr} in (3.42) represents the rated load resistance, which is the fixed value and is given as a design specification. Although the output voltage V_O depends on the initial design value of the load resistance R_{Lr}, the output voltage keeps a constant value against the changes in the load resistance R_L.

3.5 Experimental Results

The circuit experiment was conducted for the WPT system with the load-independent class-EF and the proposed inverters, shown in Fig. 3.8(a) and 3.8(b).

3.5.1 Experimental Prototype

The design specification of the WPT system with the proposed inverter was given as: $f = 3.39$ MHz, $V_I = 120$ V, $R_{Lr} = 50\ \Omega$, and $V_O = 65$ V. The coupling coils were solenoid-type and made with air core, having a transmission distance of $d = 15$ mm. The geometric parameters of the coupling coils are given in Table 3.1, where h_{core} and d_{core} are the height and diameter of the coils, respectively. Additionally, the turn numbers N and wire diameters d_w in Table 3.1 are determined to obtain the desired output voltage from (3.42).

The implemented coupling coils had inductances of $L_1 = 5.24$ μH and $L_2 = 5.93$ μH with ESRs of $r_{L_1} = 0.342$ Ω and $r_{L_2} = 0.488$ Ω, respectively. Besides, a measured coupling coefficient between L_1 and L_2 was $k = 0.224$. From the measured parameters, the equivalent resistance $R_{inv} = 56.5$ Ω was obtained. The proposed inverter can provide a sinusoidal output current even without the SR filter. Therefore, we used sufficiently large capacitance for C_0, which only works as a DC blocking. Table 3.2 gives the component values of the WPT system with proposed and load-independent class-EF inverters, which were obtained by following the design in Section 5.3 and 3.3.7.

The WPT system with the load-independent class-EF inverter shown in Fig. 3.8(a) was also designed with the same coupling coils and the receiver circuit as the proposed WPT system. However, there is a difference in the voltage gain between the load-independent class-EF and the proposed inverters. Therefore, the input voltage of the WPT system with the load-independent class-EF inverter was set to $V_I = 180$ V to obtain the same output voltage as the proposed WPT system. Table 3.2 gives the component values of the WPT system with the load-independent class-EF inverter, which were designed with the on-duty ratio of $D = 0.3$ [15].

For implementing the WPT system, we selected GS-065-004-1-L GaN E-HEMT from GaN Systems for the switching device, whose on-resistance was $r_S = 0.45$ Ω. Fig. 3.9 shows the output capacitance of the selected GaN E-HEMT as a function of the switch voltage. It is essential for the proposed inverter to select the switching device whose output capacitance is sufficiently low. This is because the analysis given in Section 6.4 does not consider the output capacitance. The T68-6 iron-powder toroidal core from Micrometals was used to implement the series inductance

L_S. The STPS5H100 Schottky Rectifier from STMicroelectronics was adopted for the diode D_1 and D_2, whose on-resistance, forward voltage, and parasitic capacitance were 0.024 Ω, 0.49 V, and 90 pF, respectively. The experimental component values are given in Table 3.2, which were measured by E4990A Impedance Analyzer from Keysight Technologies. Fig. 3.10 shows a photograph of the implemented WPT system with the proposed inverter and the class-D rectifier.

3.5.2 Operating Waveform

Fig. 7.4(a)-(c) shows the experimental waveforms of the WPT system with the load-independent class-EF inverter. It is seen from Fig. 7.4(a)-(c) that the switch voltage v_S achieved the ZVS regardless of the load resistance. In addition, the amplitude and the phase shift of the transmission current i_1 were constant even for different load resistances due to the load-independent design. However, the current i_1 comprises significant harmonics due to the specific tuning of the L_h-C_h for the load-independent design.

Fig. 7.4(d)-(f) shows the experimental waveforms of the WPT system with the proposed inverter. We can see from Fig. 7.4(d)-(f) that the switch current i_S achieved the ZCS, and the amplitude of current i_1 was constant regardless of the load resistance. The switch voltage at the turn-on moment was reduced, effectively suppressing the turn-on switching loss, as described in Section 3.3.7. Besides, the current i_1 became a sinusoidal waveform despite the absence of the SR filter. The voltage across the diode D_1 was strongly influenced by parasitic capacitance, resulting in long rise and fall times for light load conditions, as given in (3.38). Also, the reac-

tance component seen from the inverter changes with DC load variations due to the parasitic capacitances of the diodes. Nevertheless, the proposed inverter achieves consistent CC operation. This is because the proposed inverter did not use the SR filter and was less sensitive against reactance component variations. These results demonstrate the effectiveness of the proposed inverter.

Fig. 7.4(g)-(i) show the numerical waveforms of the WPT system with the proposed inverter for $R_L = 100\ \Omega$ and $R_L = 1\ \mathrm{k}\Omega$. The waveforms are derived using the numerical analysis [32], which considers parasitic components, including the non-linear output capacitance shown in Fig. 3.9, the on-resistances of the switch and diodes, and ESRs of the inductances. We can see from Fig. 7.4(d)-(f) and 7.4(g)-(i) that the experimental and numerical waveforms showed good agreement, which demonstrates the validity of the experimental results.

3.5.3 Circuit Characteristics

Fig. 7.5 shows the experimental characteristics of the WPT system with the proposed and load-independent class-EF inverters as a function of normalized load resistance. The experimental power-delivery efficiency was calculated as

$$\eta = \frac{P_O^2}{V_I I_I}, \tag{3.43}$$

where P_O is the DC-output power.

We can see from Fig. 7.5(a) that the transmission current amplitude of the load-independent class-EF inverter changed at the small load resistance. On the other hand, the proposed inverter maintained consistent CC operation. This is because the proposed inverter exhibits robustness even against reactive-component variations

due to the low-Q output filter. Although relatively large ESRs exist in the coupling coils, they are absorbed by the equivalent resistance seen from the inverter in the S-S coupling. Therefore, the CC operation of the proposed inverter was not significantly affected by the ESRs.

We can see from Fig. 7.5(a) that the output voltage of both WPT systems increased as the load resistance. The output voltage can be constant against load variations in an ideal case where the diodes have no parasitic capacitance, as given in (3.42). However, the effects of the parasitic capacitances appear at high-frequency operations. As a result, the output voltage varied depending on the load resistance, as given in (3.41). The weak output-voltage regulation is an essential issue in the load-independent inverters [11–19]. Therefore, the DC-DC converter is typically added after the rectifier stage [16] for further accuracy of the output regulation. Also, the numerical design method, which can consider the parasitic components of the devices, has been proposed [33]. Although the method has a high computational cost, it is effective for the WPT system with the proposed inverter to increase the accuracy of the output-voltage regulation.

Fig.7.5(b) demonstrates that the WPT system with the proposed inverter achieved the same level of efficiency at heavy load as the WPT system with the load-independent class-EF inverter. However, the efficiency of the proposed inverter decreased at light load. This is because the proposed inverter had a turn-on switching loss, which cannot be negligible at light load. The peak DC-to-DC efficiency 88 % was achieved for 60 W output power in the proposed WPT system.

Fig. 3.13 shows the power-loss breakdown of the WPT system with the proposed inverter, where the subscript of the symbol indicates the power-loss factor. The

power losses are calculated by using the numerical analysis [32], which considers the ESR of inductors, on resistances of the switching device and diodes, the forward voltage of the diodes, and turn-on switching loss as power-loss factors. We can see from Fig. 3.13 that the power-loss due to the ESR of L_2 and the turn-on switching loss are the dominant factors at heavy load. Meanwhile, the power loss due to the ESR of L_1 becomes dominant at the light load. This is because the power loss in the transmitter coil is constant against load variations due to the CC operation, which is the major challenge for the CC inverters. Although CC inverters are naturally inefficient at light loads, they are appropriate for the transmitter of the WPT systems from the perspective of overcurrent protection. The predicted power-delivery efficiency for $R_L = 100\,\Omega$ and $R_L = 1\,\mathrm{k}\Omega$ are 88.3% and 41.7%, which are quantitatively agrees with the experimental efficeincy of 88.0% and 41.3%, respectively.

Fig. 3.14 shows the THD of transmission current i_1 in the WPT system with the class-EF and the proposed inverters. The THD of the transmission current is defined as

$$\mathrm{THD} = \frac{\sqrt{\sum_{n=2}^{\infty} {I_{mn}^*}^2}}{I_m^*}, \tag{3.44}$$

where I_{mk}^* is the normalized amplitude of k-th harmonic current flowing through transmitter coil. We can see from Fig. 3.14 that the proposed inverter achieved lower THD than the load-independent class-EF inverter over the entire load range. The THD of the load-independent class-EF inverter increases, especially for the small load resistance, because the loaded quality factor of the SR filter becomes small. On the other hand, the proposed inverter inherently outputs a sinusoidal waveform without the SR filter. Therefore, the THD of the output current is almost

constant against load variations.

Based on the experimental results, we can verify that the proposed inverter mitigated harmonic currents in the coupling part of the WPT system. Furthermore, the WPT system incorporating the proposed inverter achieved superior consistency of the CC operation compared to the WPT system with the load-independent class-EF inverter. These results substantiate the effectiveness of the proposed inverter.

3.6 Comparison With Previous Works

Table 3.3 gives the load-independent inverters with CC output characteristics proposed so far. The load-independent class-EF inverter [15] has the SR-CC feature, which is suitable for the transmitter of the WPT system. Furthermore, the switch-voltage stress is suppressed by utilizing the harmonic resonant filter. However, the output current suffers from harmonic distortion. The load-independent class-E inverter [14] achieves CC output with a PR output filter. Although the inverter has a floating load, it consists of only four passive elements, contributing to circuit miniaturization. The load-independent push-pull class-E and class-Φ inverters [19,27] apply the LCCL filter to attain the CC output. The inverters introduce a three-winding coupled inductor, reducing harmonics in the input current. The load-independent class-F/E inverter [21] has a dual topology with the load-independent class-EF inverter [15] and achieves ZCS and CC output regardless of the load resistance with the PR filter.

The proposed inverter has the switch voltage and current waveforms, which are less sensitive against load variations compared with the original class-E inverters.

Moreover, the proposed load-independent inverter can inherently produce a purely sinusoidal output even with a low-Q output filter. Consequently, it exhibits lower sensitivity to component variations in the resonant filter. This unique characteristic represents an advantage of the proposed inverter.

3.7 Conclusion

This chapter has presented the analysis and design of the load-independent SR inverter with CC output, along with its WPT system application. The proposed inverter inherently achieves ZCS and a CC output regardless of the load resistance. Furthermore, the proposed inverter can generate a sufficiently pure sinusoidal output even with a low-Q SR filter. In the experiment, the WPT system that incorporates the proposed inverter as the transmitter was implemented. The experimental results demonstrated that the proposed inverter achieved superior consistency of the CC operation and reduced THD of current flowing through the transmitter coil compared with the WPT system employing the load-independent class-EF inverter. The experimental results showed the validity of the inverter design and analysis.

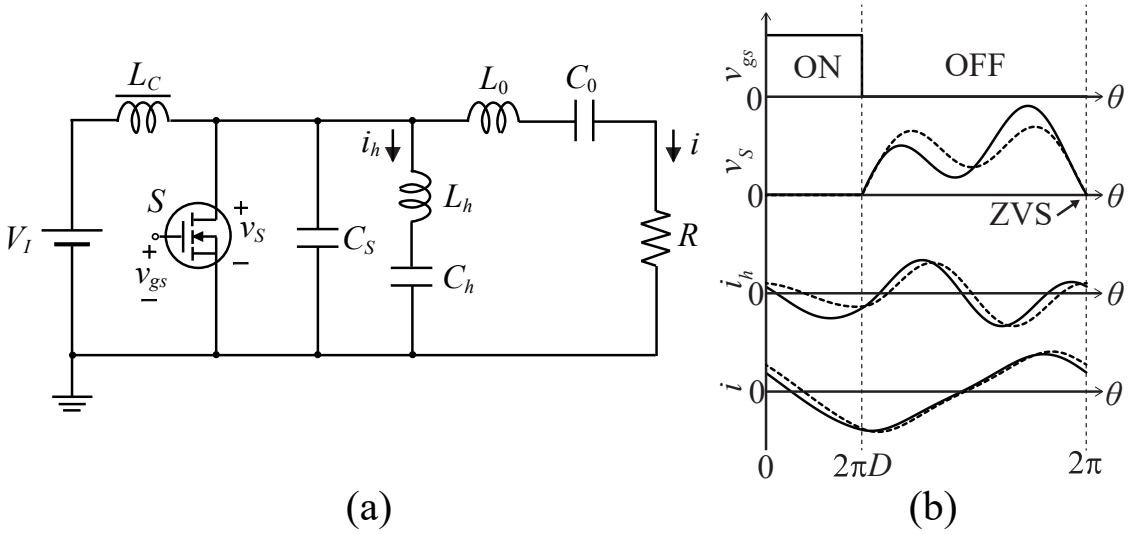

Fig. 3.1: The load-independent class-EF inverter. (a) Circuit topology. (b) Example waveforms at fixed load resistances (solid line: $R/R_r = 1$, dashed line: $R/R_r = 0.1$.)

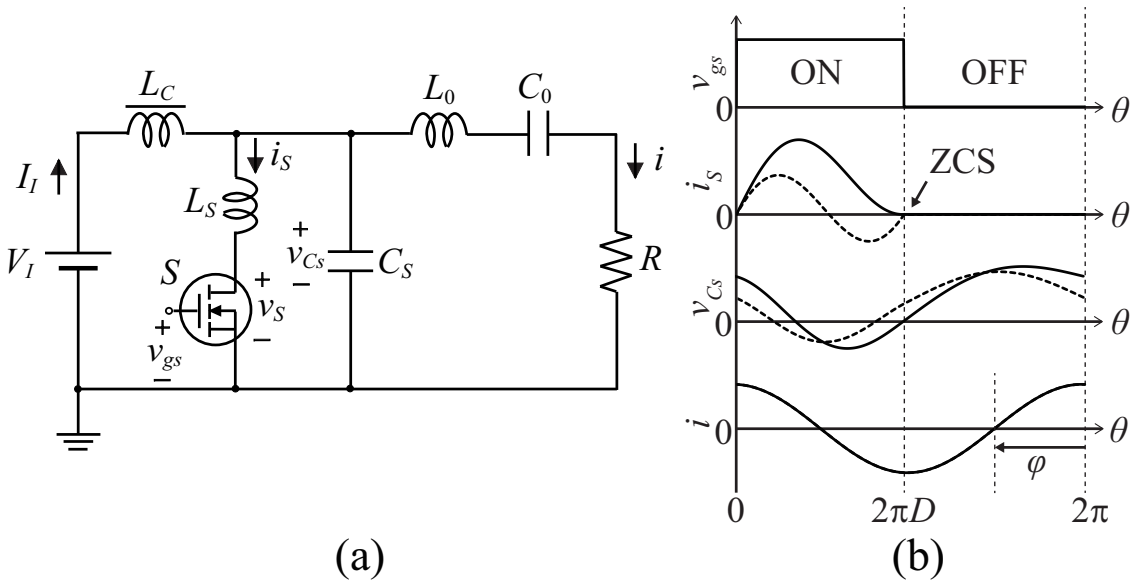

Fig. 3.2: Proposed inverter. (a) Circuit topology. (b) Example waveforms for fixed load resistances (solid line: $R/R_r = 1$, dashed line: $R/R_r = 0.1$.)

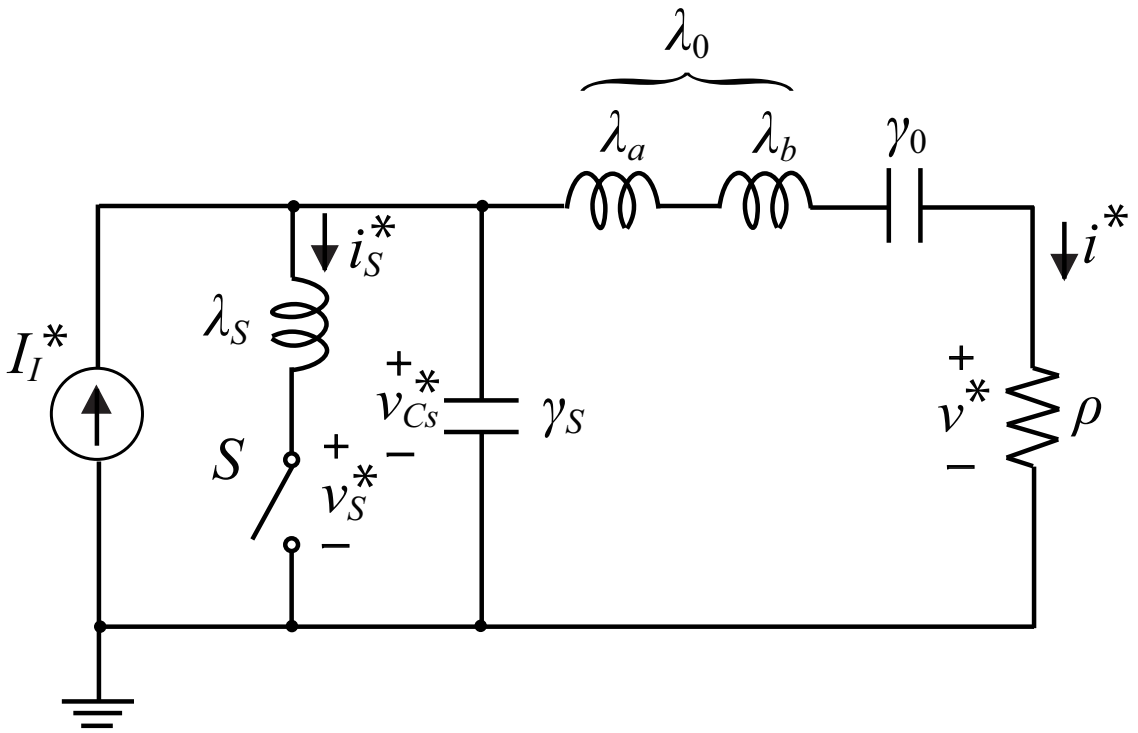

Fig. 3.3: Analytical model of the proposed inverter.

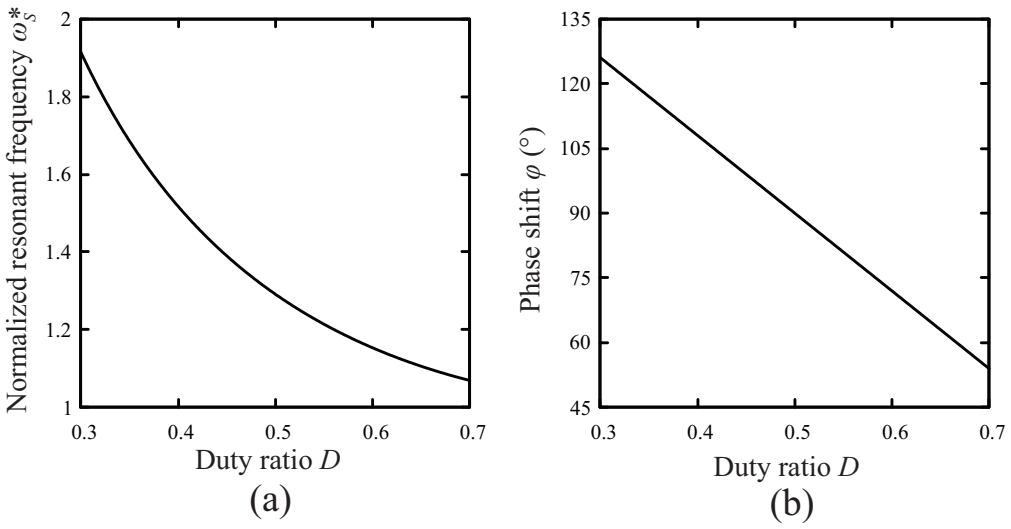

Fig. 3.4: The circuit parameters that satisfy the load-independent conditions as functions of duty ratio D. (a) The normalized resonant angular frequency ω_S^*. (b) The phase shift between output current and gate-drive voltage.

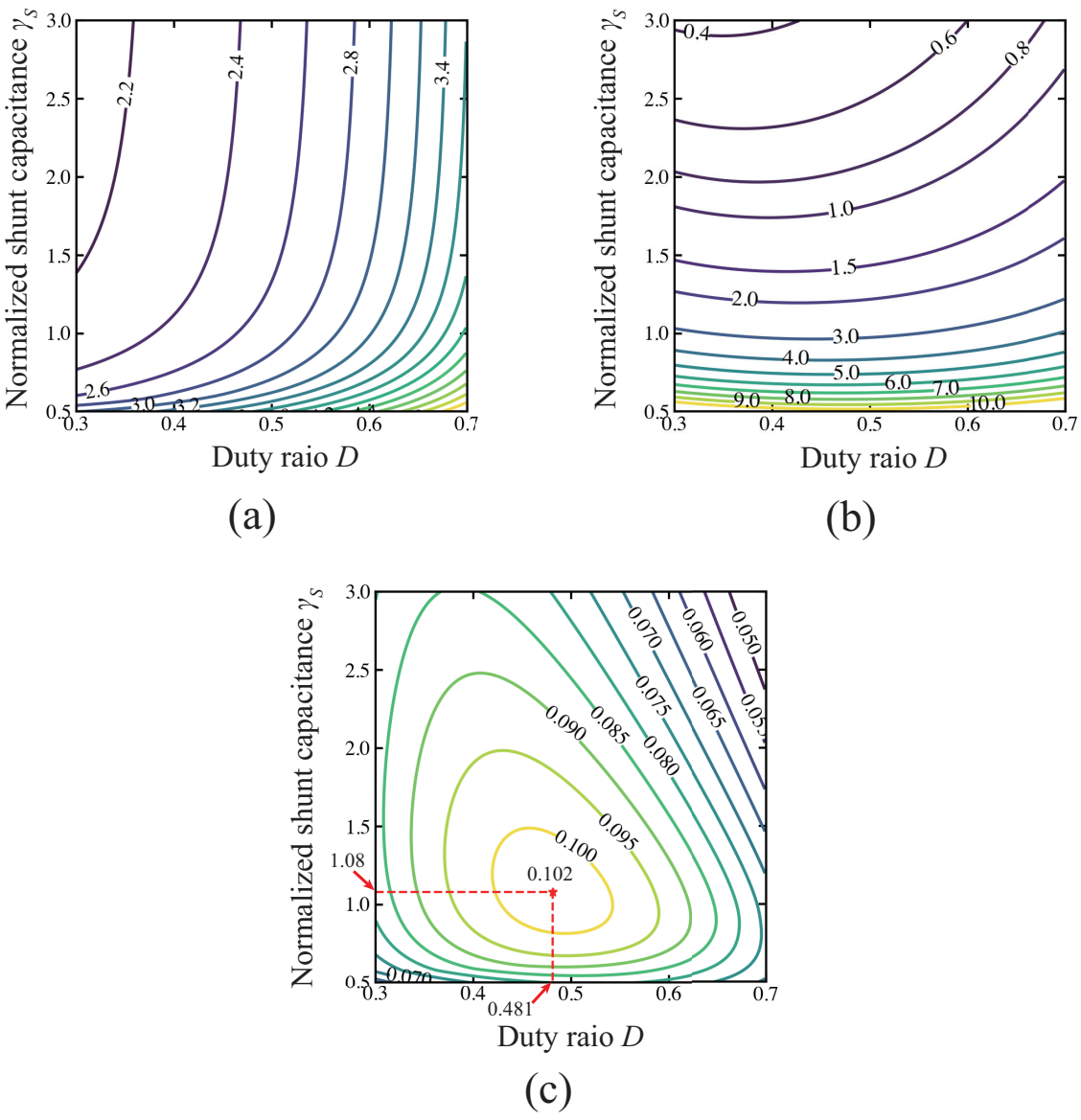

Fig. 3.5: Inverter characteristics as functions of duty ratio D and normalized shunt capacitance γ_S. (a) Switch-voltage stress V^*_{Smax}. (b) Switch-current stress I^*_{Smax}. (c) Power-output capability.

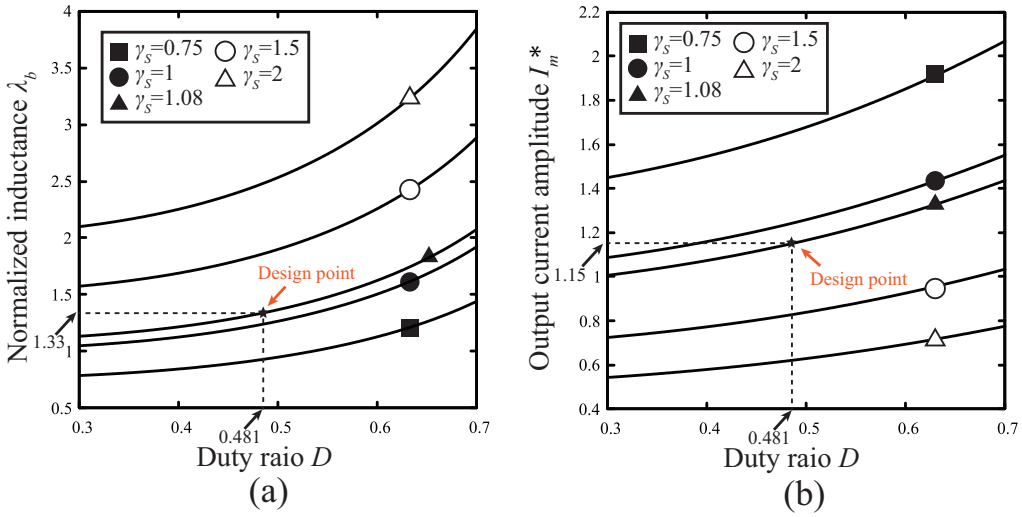

Fig. 3.6: Design curves of the proposed inverter as functions of duty ratio D. (a) Normalized inductance λ_b. (b) Normalized output-current amplitude I_m^*.

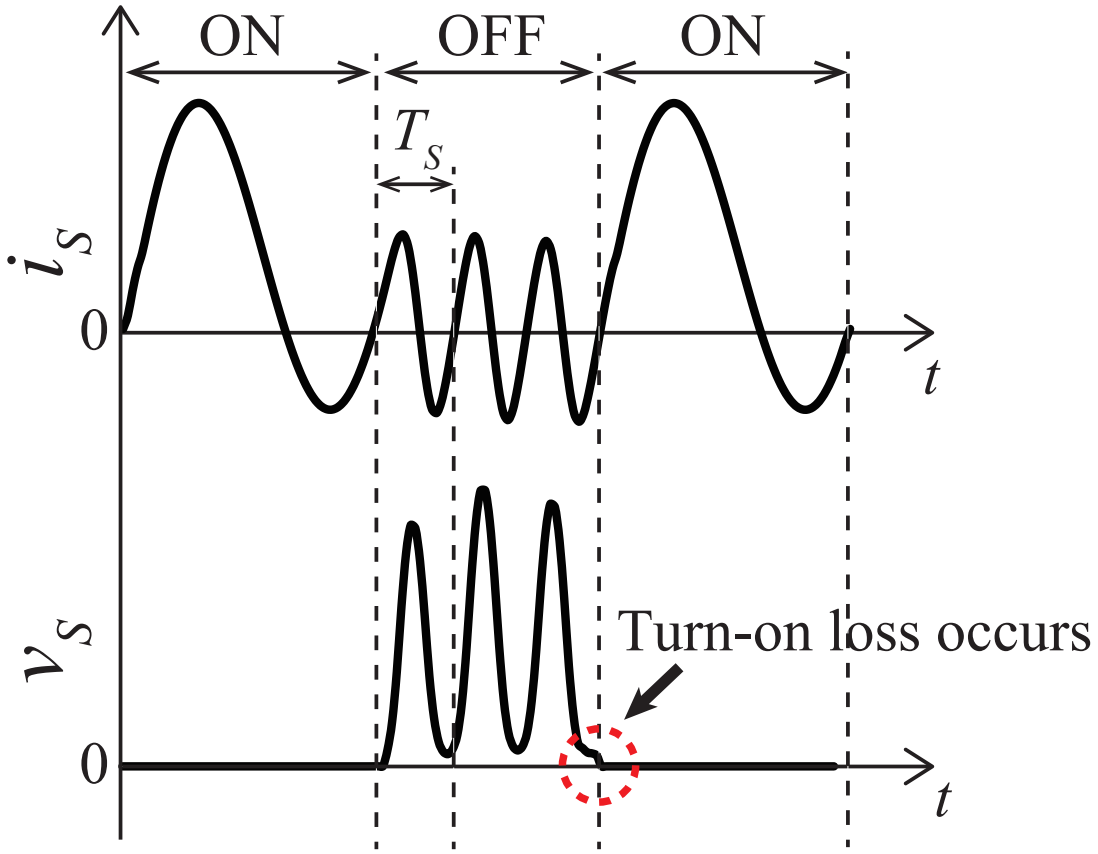

Fig. 3.7: The example waveforms of switch current and voltage of the proposed inverter.

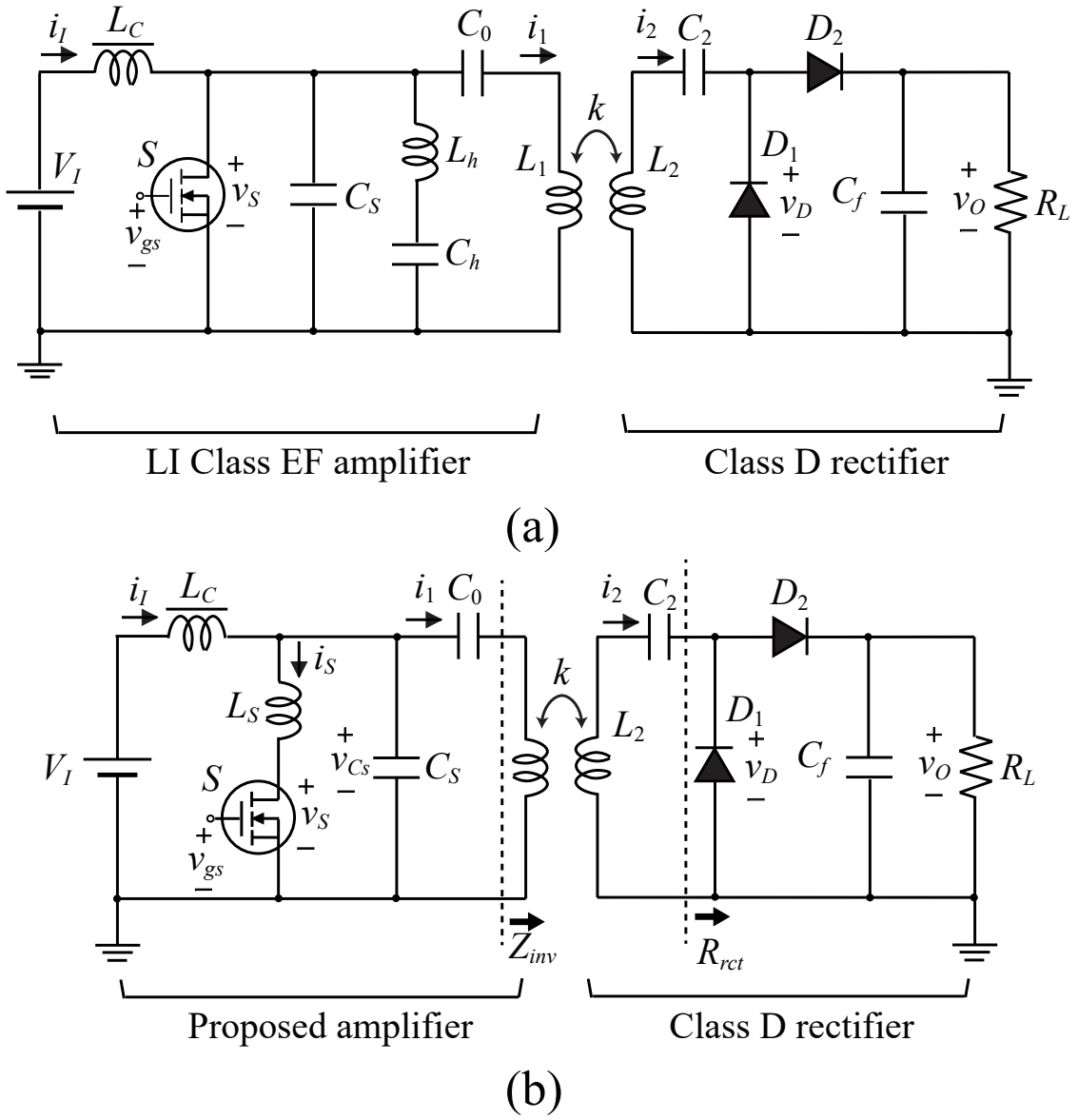

Fig. 3.8: The circuit configurations of the WPT system. (a) With the load-independent class-EF inverter. (b) With the proposed inverter.

Table 3.1: Geometric parameters of transmitter and receiver coils.

	h_{core}	d_{core}	N	d_w
Transmitter coil	15 mm	60 mm	6	1.2 mm
Receiver coil	12 mm		6	1.2 mm

Table 3.2: Analytical and measured component values of the WPT systems.

Load-Independent class-EF WPT system			WPT system with proposed inverter		
	Analytical	Experiment		Analytical	Experiment
L_C	-	150 μH	L_C	-	150 μH
L_h	7.07 μH	7.04 μH	L_S	2.42 μH	2.42 μH
C_S	147 pF	100 pF	C_S	519 pF	519 pF
C_0	20.4 nF	19.8 nF	C_0	-	1.0 μF
C_h	112 pF	111 pF	C_2	372 pF	371 pF
C_2	372 pF	371 pF	C_f	-	1.0 μF
C_f	-	1.0 μF	r_{L_C}	-	100 mΩ
r_{L_C}	-	100 mΩ	r_{L_S}	-	178 mΩ
r_{L_h}	-	304 mΩ			

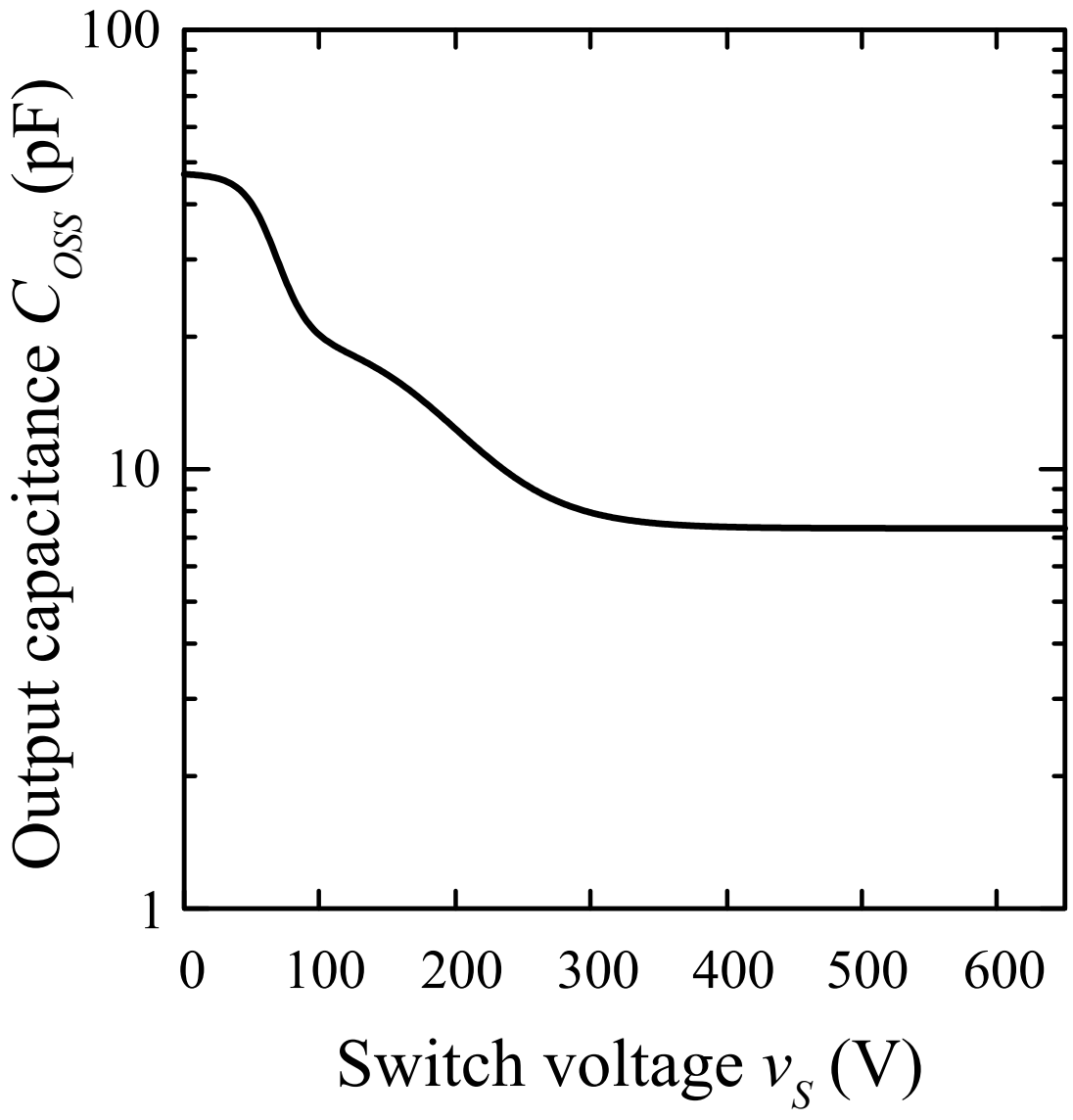

Fig. 3.9: The output capacitance of the selected GaN E-HEMT as a function of the switch voltage.

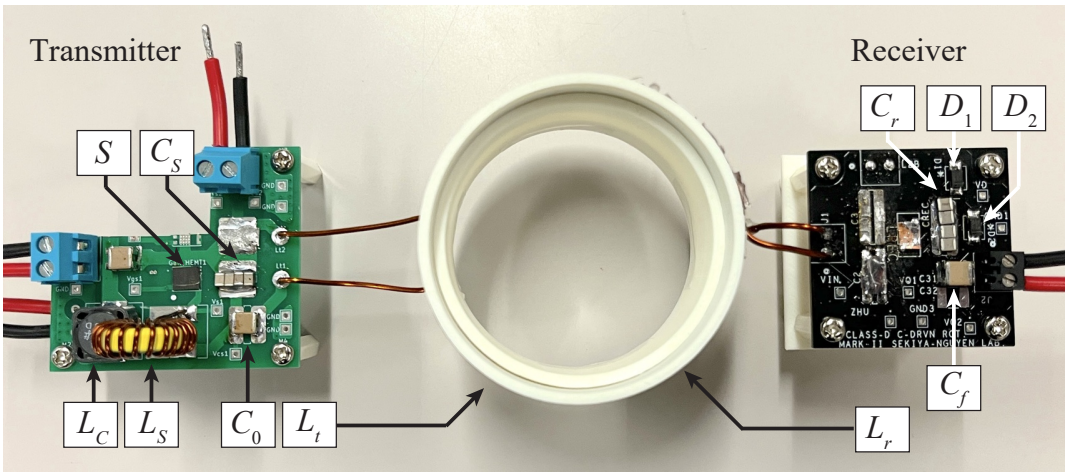

Fig. 3.10: Photograph of the implemented proposed WPT system.

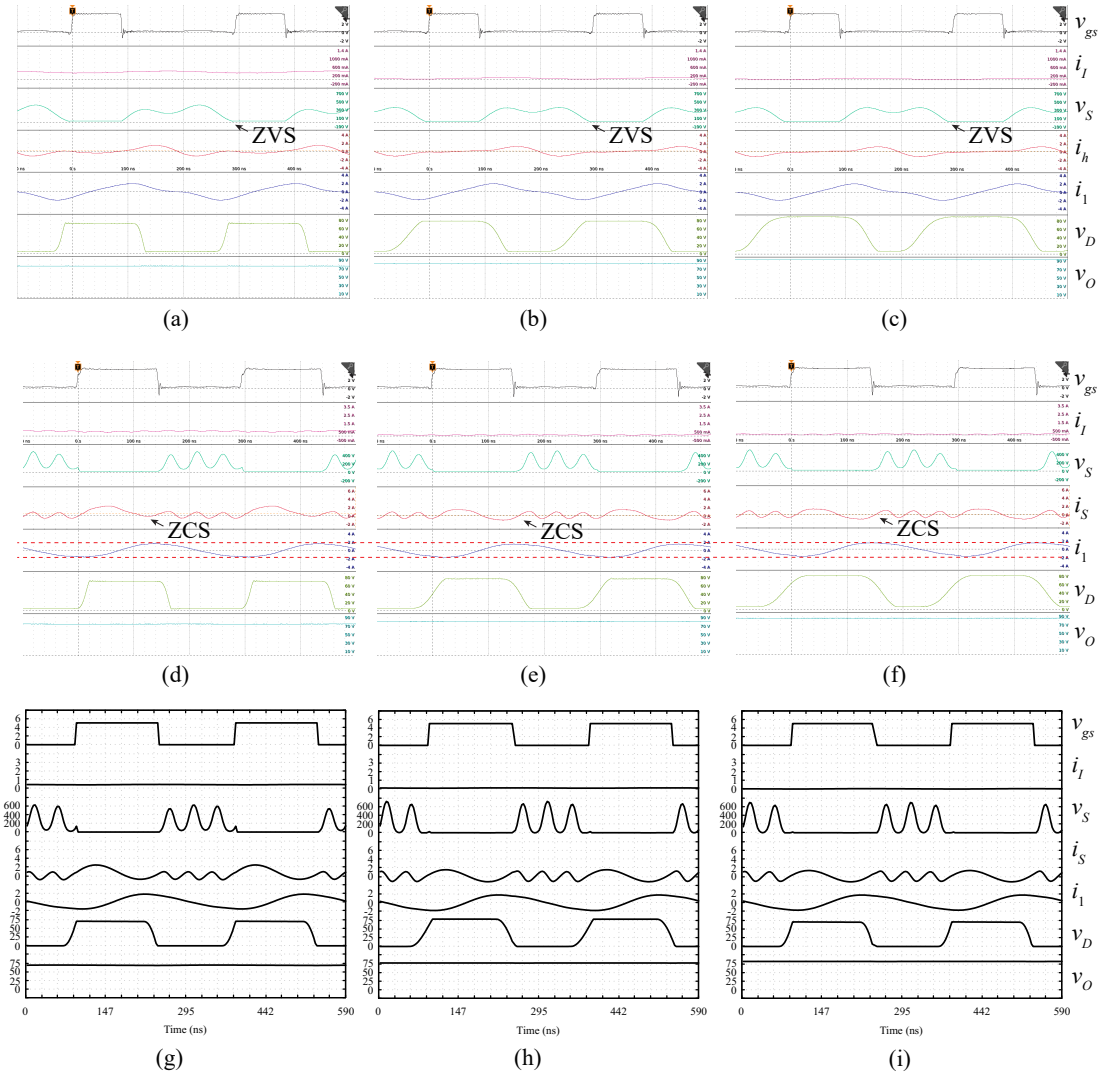

Fig. 3.11: Experimental and numerical waveforms of the WPT systems. (a) With the load-independent class-EF inverter for $R_L = 100\ \Omega$ (Experiment). (b) With the load-independent class-EF inverter for $R_L = 1\ \text{k}\Omega$ (Experiment). (c) With the load-independent class-EF inverter for open load (Experiment). (d) With the proposed inverter for $R_L = 100\ \Omega$ (Experiment). (e) With the proposed inverter for $R_L = 1\ \text{k}\Omega$ (Experiment). (f) With the proposed inverter for open load (Experiment). (g) With the proposed inverter for $R_L = 100\ \Omega$ (Numerical). (h) With the proposed inverter for $R_L = 1\ \text{k}\Omega$ (Numerical). (i) With the proposed inverter for open load (Numerical).

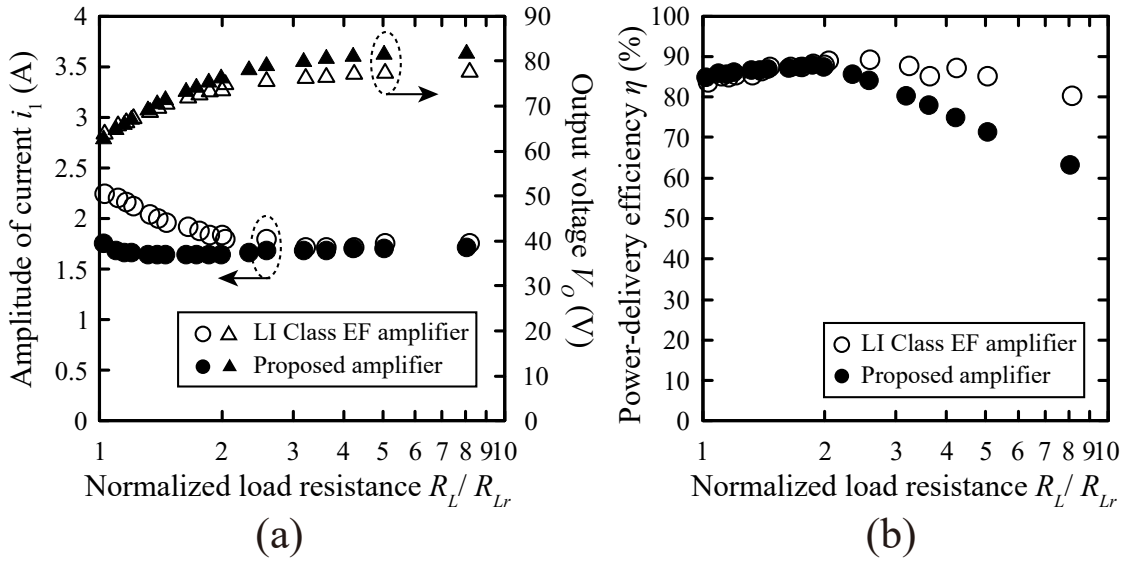

Fig. 3.12: Experimental characteristics of the WPT system with the load-independent class-EF and the proposed inverters as a function of normalized load resistance. (a) Amplitude of the current i_1 and output voltage V_O. (b) Power-delivery efficiency η.

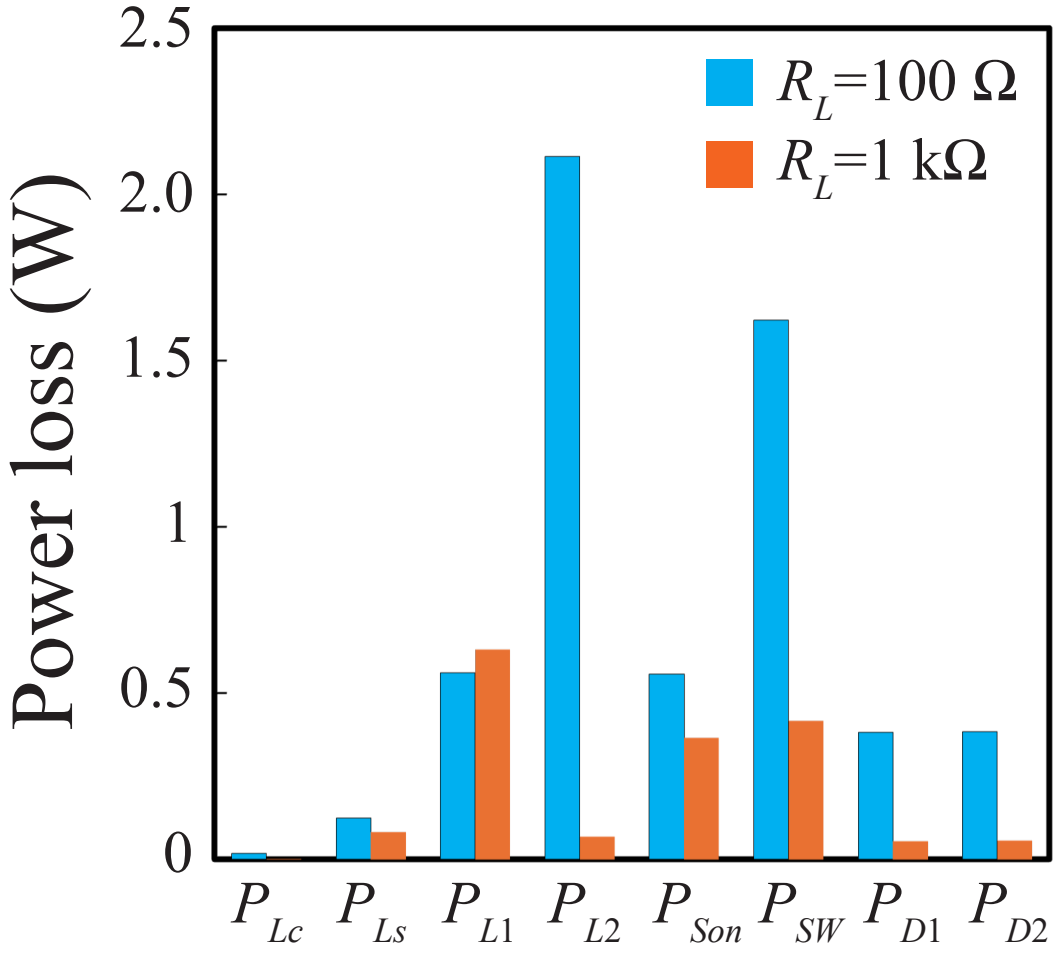

Fig. 3.13: Power-loss breakdown of the WPT system with the proposed inverter for $R_L = 100\ \Omega$ and $R_L = 1\ \text{k}\Omega$.

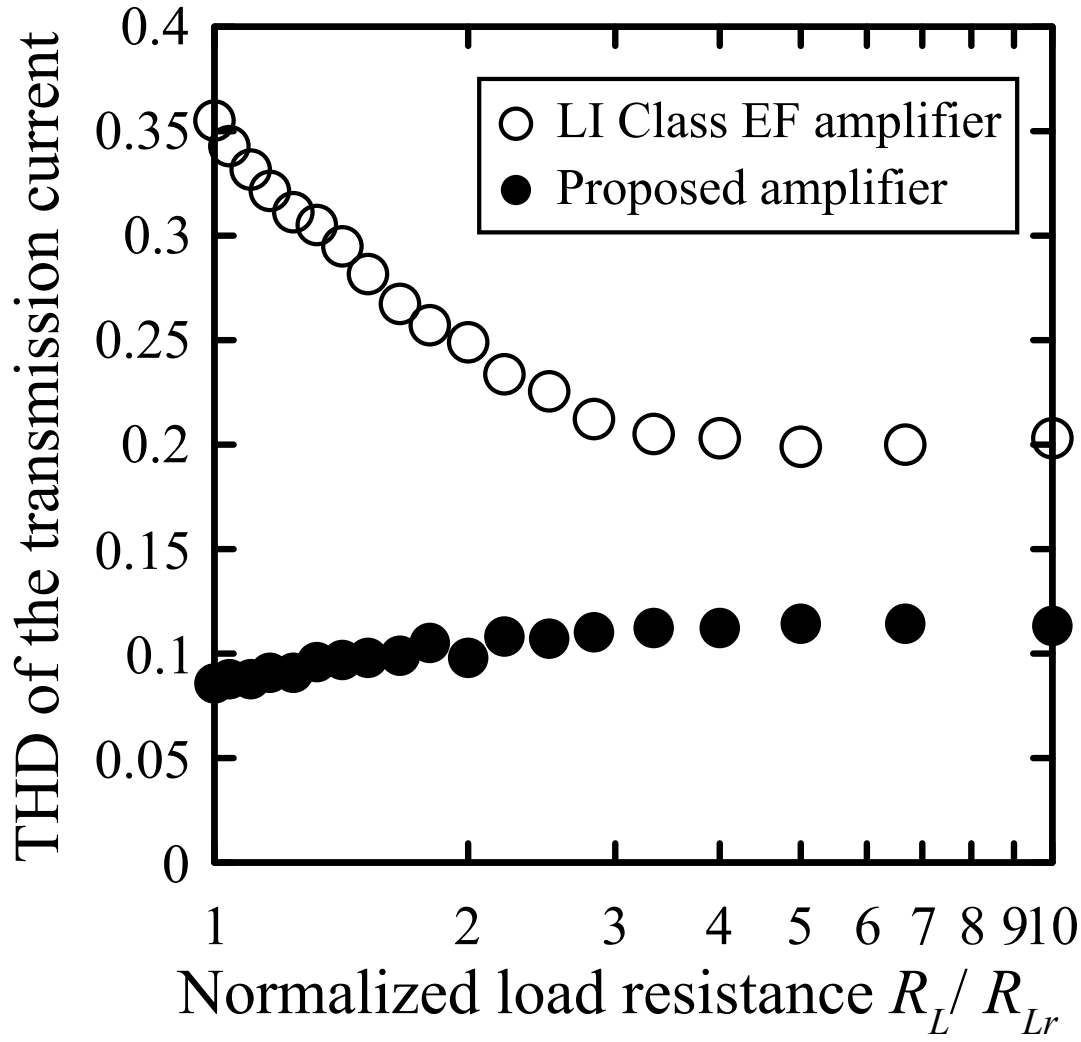

Fig. 3.14: The THD of the output current as a function of normalized load resistance.

Table 3.3: Load-independent inverters with CC output feature.

	Aldhaher [15]	Tomohiro [14]	Huang [27]	Huang [19]	Zhu [21]	This work
Circuit topology	class-EF	class-E	Push-pull class-E	Push-pull class-Φ	class-F/E	Inverse class-E
Output resonant filter	Series	Parallel	LCCL	LCCL	Parallel	Series
Component number	6	4	7	8	5 or 7	5
Switching type	ZVS	ZVS	ZVS	ZVS	ZCS	ZCS
Output	CC	CC	CC	CC	CC	CC
Power-output capability	0.0882	0.101	-	-	0.085	0.102
Frequency (MHz)	13.56	1	6.78	6.78	1	3.39
Output power (W)	14-150	0.3-11.5	0-320	70-320	2.5-25	0-75
Efficiency	94.4% (DC/AC)	89.3% (DC/AC)	89.3% (DC/DC)	91% (DC/DC)	94.2% (DC/AC)	88.0% (DC/DC)

References

[1] X. Hao, J. Zou, K. Yin, X. Ma and T. Dong, "Enhanced Power Conversion Capability of Class-E Power Amplifiers With GaN HEMT Based on Cross-Quadrant Operation," in IEEE Transactions on Power Electronics, vol. 37, no. 11, pp. 13966-13977, Nov. 2022.

[2] K. N. Surakitbovorn and J. M. Rivas-Davila, "On the Optimization of a Class-E Power Amplifier With GaN HEMTs at Megahertz Operation," in IEEE Transactions on Power Electronics, vol. 35, no. 4, pp. 4009-4023, April 2020.

[3] Z. Tong, L. Gu, Z. Ye, K. Surakitbovorn and J. Rivas-Davila, "On the Techniques to Utilize SiC Power Devices in High- and Very High-Frequency Power Converters," in IEEE Transactions on Power Electronics, vol. 34, no. 12, pp. 12181-12192, Dec. 2019.

[4] N. O. Sokal and A. D. Sokal, "Class E-A new class of high-efficiency tuned single-ended switching power amplifiers," in IEEE Journal of Solid-State Circuits, vol. 10, no. 3, pp. 168-176, June 1975.

[5] A. Ghahremani, A. -J. Annema and B. Nauta, "Load Mismatch Sensitivity of Class-E Power Amplifiers," in IEEE Transactions on Microwave Theory and Techniques, vol. 67, no. 1, pp. 216-230, Jan. 2019.

[6] S. Park and J. Rivas-Davila, "Duty Cycle and Frequency Modulations in Class-E DC-DC Converters for a Wide Range of Input and Output Voltages," in IEEE Transactions on Power Electronics, vol. 33, no. 12, pp. 10524-10538, Dec. 2018.

[7] R. E. Zulinski and K. J. Grady, "Load-independent class E power inverters. I. Theoretical development," in IEEE Transactions on Circuits and Systems, vol. 37, no. 8, pp. 1010-1018, Aug. 1990.

[8] M. Liu, C. Zhao, J. Song and C. Ma, "Battery Charging Profile-Based Parameter Design of a 6.78-MHz Class E2 Wireless Charging System," in IEEE Transactions on Industrial Electronics, vol. 64, no. 8, pp. 6169-6178, Aug. 2017.

[9] Z. Sun, Y. Wang, J. Sun, Y. Guan and D. Xu, "Design of a Strong Robust Wireless Power Transfer System With Wide-Range Output Regulation Based on Dual-Band Architecture," in IEEE Transactions on Industrial Electronics, vol. 70, no. 11, pp. 11142-11152, Nov. 2023.

[10] F. Raab, "Idealized operation of the class E tuned power amplifier," in IEEE Transactions on Circuits and Systems, vol. 24, no. 12, pp. 725-735, December 1977.

[11] A. Komanaka, W. Zhu, X. Wei, K. Nguyen and H. Sekiya, "Generalized Analysis of Load-Independent ZCS Parallel-Resonant Inverter," in IEEE Transactions on Industrial Electronics, vol. 69, no. 1, pp. 347-356, Jan. 2022.

[12] Y. Komiyama, W. Zhu, K. Nguyen and H. Sekiya, "Load-Independent Constant-Current/Zero-Current Switching Inverter with Series Resonant Filter," 2023 IEEE Applied Power Electronics Conference and Exposition (APEC), Orlando, FL, USA, 2023, pp. 490-494.

[13] T. Sensui and H. Koizumi, "Load-Independent Class E2 Parallel Resonant DC-DC Converter," in IEEE Transactions on Circuits and Systems II: Express Briefs, vol. 69, no. 11, pp. 4374-4378, Nov. 2022.

[14] T. Sensui and H. Koizumi, "Load-Independent Class E Zero-Voltage-Switching Parallel Resonant Inverter," in IEEE Transactions on Power Electronics, vol. 36, no. 11, pp. 12805-12818, Nov. 2021.

[15] S. Aldhaher, D. C. Yates and P. D. Mitcheson, "Load-Independent Class E/EF Inverters and Rectifiers for MHz-Switching Applications," in IEEE Transactions on Power Electronics, vol. 33, no. 10, pp. 8270-8287, Oct. 2018.

[16] J. M. Arteaga, S. Aldhaher, G. Kkelis, C. Kwan, D. C. Yates and P. D. Mitcheson, "Dynamic Capabilities of Multi-MHz Inductive Power Transfer Systems Demonstrated With Batteryless Drones," in IEEE Transactions on Power Electronics, vol. 34, no. 6, pp. 5093-5104, June 2019.

[17] J. M. Arteaga, S. Aldhaher, G. Kkelis, D. C. Yates and P. D. Mitcheson, "Multi-MHz IPT Systems for Variable Coupling," in IEEE Transactions on Power Electronics, vol. 33, no. 9, pp. 7744-7758, Sept. 2018.

[18] J. M. Rivas, O. Leitermann, Y. Han and D. J. Perreault, "A Very High Frequency DC-DC Converter Based on a Class Φ 2 Resonant Inverter," in IEEE Transactions on Power Electronics, vol. 26, no. 10, pp. 2980-2992, Oct. 2011.

[19] X. Huang, Y. Lin, Y. Dou, S. Lin and J. Huang, "Load-Independent Push-Pull Class-Φ 2 Inverter With Single Compact Three-Winding Inductor," in IEEE Transactions on Power Electronics, vol. 38, no. 10, pp. 11916-11927, Oct. 2023.

[20] H. Sekiya, K. Tokano, W. Zhu, Y. Komiyama and K. Nguyen, "Design Procedure of Load-Independent Class-E WPT Systems and Its Application in Robot Arm," in IEEE Transactions on Industrial Electronics, vol. 70, no. 10, pp. 10014-10023, Oct. 2023.

[21] W. Zhu, Y. Komiyama, A. Komanaka, K. Nguyen and H. Sekiya, "Analysis of Load-Independent ZCS Parallel-Resonant Inverter With Constant Current," in IEEE Transactions on Industrial Electronics, vol. 71, no. 9, pp. 10433-10443, Sept. 2024.

[22] S. D. Kee, I. Aoki, A. Hajimiri and D. Rutledge, "The class-E/F family of ZVS switching amplifiers," in IEEE Transactions on Microwave Theory and Techniques, vol. 51, no. 6, pp. 1677-1690, June 2003.

[23] Z. Kaczmarczyk, "High-Efficiency Class E, EF2 , and E/F3 Inverters," in IEEE Transactions on Industrial Electronics, vol. 53, no. 5, pp. 1584-1593, Oct. 2006.

[24] I. Nikiforidis, J. M. Arteaga, C. H. Kwan, N. Pucci, D. C. Yates and P. D. Mitcheson, "Generalized Multistage Modeling and Tuning Algorithm for Class EF and Class Φ Inverters to Eliminate Iterative Retuning," in IEEE Transactions on Power Electronics, vol. 37, no. 10, pp. 12877-12900, Oct. 2022.

[25] S. Aldhaher and P. D. Mitcheson, "500W 13.56MHz Class EF Push-pull Inverter for Advanced Dynamic Wireless Power Applications," 2019 IEEE PELS Workshop on Emerging Technologies: Wireless Power Transfer (WoW), London, UK, 2019, pp. 263-267.

[26] M. Liu, M. Fu and C. Ma, "Low-Harmonic-Contents and High-Efficiency Class E Full-Wave Current-Driven Rectifier for Megahertz Wireless Power Transfer Systems," in IEEE Transactions on Power Electronics, vol. 32, no. 2, pp. 1198-1209, Feb. 2017.

[27] X. Huang, Z. Yu, Y. Dou, S. Lin, Z. Ouyang and M. A. E. Andersen, "Load-Independent Push-Pull Class E2 Topology With Coupled Inductors for MHz-WPT Applications," in IEEE Transactions on Power Electronics, vol. 37, no. 7, pp. 8726-8737, July 2022.

[28] T. Mury and V. F. Fusco, "Inverse Class-E Amplifier With Transmission-Line Harmonic Suppression," in IEEE Transactions on Circuits and Systems I: Regular Papers, vol. 54, no. 7, pp. 1555-1561, July 2007.

[29] M. Kazimierczuk, "Class D current-driven rectifiers for resonant DC/DC converter applications," IEEE Trans. Ind. Electron., vol. 38, no. 5, pp. 344-354, 1991.

[30] M. K. Kazimierczuk and D. Czarkowski, Resonant Power Converters. Wiley, 2011.

[31] K. Fukui and H. Koizumi, "Analysis of half-wave class DE low dv/dt rectifier at any duty ratio," IEEE Trans. Power Electron., vol. 29, no. 1, pp. 234-245, 2014.

[32] W. Zhu, Y. Komiyama, K. Nguyen, and H. Sekiya, "Comprehensive and simplified numerical design procedure for class-E switching circuits," IEEE Access, vol. 9, pp. 149 971-149 981, 2021.

[33] W.Zhu, Y.Komiyama, K.Nguyen, and H.Sekiya, "Heuristic algorithm-based design method for class-E switching circuits," in Proc. IEEE Energy Conv. Congr. Expo. (ECCE), pp. 5692-5697, 2021.

Chapter 4

Load-Independent Class-Φ_3 Inverter

4.1 Introduction

Wide-bandgap semiconductor devices such as GaN and SiC expand the operating range of power electronic circuits, especially in the high-frequency regime [1]. In high-frequency operation, the energy-storage requirement of the circuit can be reduced, which reduces the physical size of passive components. As a result, the power density of the circuits can be increased. However, the high-frequency operation increases the switching losses proportionally. Therefore, high-frequency inverters are mandatory to achieve ZVS to suppress the switching losses [2, 3].

The circuit design that accounts for load variations is also a critical challenge for power electronics circuits. A specific control is typically applied to maintain high power-conversion efficiency and output regulation against the load variations [4, 5]. However, the requirements for PWM resolution become more stringent in high-frequency regimes, leading to the difficulty in maintaining control accuracy and stability. Hence, a fundamental solution to load variations in high-frequency power

electronics circuits at the megahertz band has been strongly demanded. Recently, the load-independent inverters [6–13], which exhibit robustness against load variations, have attracted much attention. The load-independent inverters inherently achieve the ZVS and a constant AC output against the load variations. Therefore, the load-independent inverters eliminate the need for applying controls, paving a new way to address load variations.

The load-independent designs have been realized in various circuit topologies so far [6–13]. Among them, the load-independent class-Φ_2 inverter [9–13] has been widely studied aiming at applications such as wireless power transfer systems [9] and inverters for plasma generation [10]. The load-independent class-Φ_2 inverter achieves the ZVS against load variations. Additionally, it maintains the constant amplitude of the output AC voltage regardless of the load resistance. The load-independent operation can be realized by tuning the component values properly, whose design conditions are clarified analytically [9]. Another essential aspect of the load-independent class-Φ_2 inverter is its reduced switch-voltage stress. The load-independent class-Φ_2 inverter has a harmonic series-resonant filter parallel to the switch, which is tuned at twice the switching frequency. As a result, the peak switch voltage is effectively reduced, allowing wider device selection.

The class-Φ_3 inverter [14–16] has another operating mode in the same circuit topology as the class-Φ_2 inverter. The class-Φ_3 inverter tunes the harmonic resonant filter at three times the switching frequency. Compared with the class-Φ_2 inverter, the class-Φ_3 inverter reduces the peak switch voltage at OFF-duty ratios of 50 % or less [15]. Moreover, the class-Φ_3 inverter has a larger input-output voltage gain, achieving higher power-output capability [16]. However, the feasibility of achieving

the load-independent operation in the class-Φ_3 inverter has never been explored. The class-Φ_3 inverter boasts superior power-output capability, suggesting a potential for enhancing the power-conversion efficiency.

This chapter proposes the design of the load-independent class-Φ_3 resonant inverter. We analyze the class-Φ_3 inverter and reveal that the load-independent operation is feasible in the class-Φ_3 operation. Namely, the load-independent class-Φ_3 inverter achieves the ZVS and a constant output-voltage amplitude regardless of the load resistance. The design conditions for achieving the load-independent operation are analytically described in this chapter. The experiment verifications were carried out to confirm the validity of the proposed design. In the experiment, the load-independent class-Φ_3 inverter achieved higher power-conversion efficiency over a wide range of load variations compared with the load-independent class-Φ_2 inverter, which substantiates the effectiveness of the proposed inverter.

4.2 Load-Independent Inverters

Fig. 4.1 shows the circuit topology of the load-independent class-Φ_2 and class-Φ_3 inverters, which have identical circuit topology. The circuit is composed of input finite-inductor L_1, shunt capacitor C_1, harmonic resonant filter L_2-C_2, series resonant filter L_3-C_3, and load resistance R_L. The harmonic resonant filter L_2-C_2 is tuned at twice and three times the switching frequency in the load-independent class-Φ_2 and class-Φ_3 inverters, respectively. Accordingly, the sets of component values for achieving the load-independent operation are totally different between the load-independent class-Φ_2 and class-Φ_3 inverters.

4.2.1 Load-Independent Class-Φ_2 Inverter

Fig. 4.2(a) shows the example waveforms of the load-independent class-Φ_2 inverter for fixed load resistances, where $\theta = \omega t = 2\pi f t$ is the phase angle, ω represents the switching angular frequency, f indicates the switching frequency, and D is the OFF-duty ratio. Besides, the subscript 'r' means its rated value. We can see from Fig. 4.2(a) that the frequency of current i_2 is twice higher than the output voltage. Owing to the harmonic current, the switch voltage is in a trapezoidal shape, effectively suppressing the voltage stress. The output sinusoidal voltage is obtained by extracting the fundamental frequency component from the switch voltage through the series resonant filter L_3-C_3.

The load-independent class-Φ_2 inverter achieves the ZVS regardless of the load resistance R_L, as shown in Fig. 4.2(a). Additionally, the amplitude of the output AC voltage is also independent of the load. The load-independent operation can be obtained by tuning the component values properly. Therefore, additional controls and circuits are not required to achieve high efficiency and output regulation against load variations.

4.2.2 Load-Independent Class-Φ_3 Inverter

Fig. 4.2(b) shows the example waveforms of the load-independent class-Φ_3 inverter for fixed load resistances. The load-independent class-Φ_3 inverter achieves the ZVS and constant output voltage regardless of the load resistance, the same as the class-Φ_2 inverter. In the class-Φ_3 operation, the third-harmonic current flows through L_2-C_2. The harmonic current suppresses the peak switch voltage and current si-

multaneously, as shown in Fig. 4.2(b). Additionally, the output voltage is larger than the class-Φ_2 inverter for the same input voltage. As a result, the power-output capability is improved compared with the class-Φ_2 inverter.

4.3 Circuit Analysis

Circuit analysis for the load-independent class-Φ_3 inverter is performed based on the following assumptions.

1. The quality factor of the harmonic resonant filter L_2-C_2 and the series resonant filter L_3-C_3 are sufficiently high so that the currents flowing through these branches can be regarded as pure sinusoidal waves as

$$i_2(\theta) = I_2 \sin(3\theta + \varphi_2), \tag{4.1}$$

and

$$i_O(\theta) = I_m \sin(\theta + \varphi), \tag{4.2}$$

where I_2 and I_m are the amplitudes, and φ_2 and φ are the phase shifts from the turn-OFF timing of the switch.

2. The resonant inductor L_3 is divided into the resonant component L_R and extra inductance L_X. The L_R and C_3 is resonate with the switching frequency as

$$\omega = \frac{1}{\sqrt{L_R C_3}}. \tag{4.3}$$

3. The switching device is modeled as an ideal switch, which turns OFF during $0 \leq \theta < 2\pi D$ and turns ON during $2\pi D \leq \theta < 2\pi$. Besides, the output capacitance of the switching device is absorbed into the shunt capacitance C_1.

4. Each passive component works linearly with no parasitic components.

Fig. 4.3 shows the analytical circuit model, which is derived from the above assumptions.

4.3.1 Waveform equations

For the switch turn-OFF period, a differential equation can be obtained from KCL as

$$\begin{aligned}\frac{d^2v_S(\theta)}{d\theta^2}+\omega_1^2v_S(\theta)=&\omega_1^2\left[V_I-\omega L_1I_m\cos\left(\theta+\varphi\right)\right.\\&\left.-3\omega L_1I_2\cos\left(3\theta+\varphi_2\right)\right],\end{aligned}\tag{4.4}$$

where

$$\omega_1=\frac{1}{\omega\sqrt{L_1C_1}},\tag{4.5}$$

is the normalized resonant frequency between L_1 and C_1. By solving (6.15), the analytical expression of the switch voltage during the turn-OFF period can be obtained as

$$\begin{aligned}v_S(\theta)=&A\cos\left(\omega_1\theta\right)+B\sin\left(\omega_1\theta\right)+V_I\\&-\frac{\omega L_1\omega_1^2I_m}{\omega_1^2-1}\cos\left(\theta+\varphi\right)-\frac{3\omega L_1\omega_1^2I_2}{\omega_1^2-9}\cos\left(3\theta+\varphi_2\right),\end{aligned}\tag{4.6}$$

where A and B are constants.

From KVL, we obtain

$$\frac{di_1(\theta)}{d\theta}=\frac{1}{\omega L_1}\left[V_I-v_S(\theta)\right].\tag{4.7}$$

By using (6.17) and (6.18), we obtain the expression of current i_1 during turn-OFF period as

$$\begin{aligned} i_1(\theta) = &- \frac{\omega_1[A\sin(\omega_1\theta) - B\cos(\omega_1\theta)]}{\omega L_1} \\ &+ \frac{\omega_1^2 I_m \sin(\theta+\varphi)}{\omega_1^2 - 1} + \frac{\omega_1^2 I_2 \sin(3\theta+\varphi_2)}{\omega_1^2 - 9} \end{aligned} \tag{4.8}$$

For the switch turn-ON period, the switch voltage becomes zero as

$$v_S(\theta) = 0. \tag{4.9}$$

From KVL, we obtain

$$\frac{di_1(\theta)}{d\theta} = \frac{V_I}{\omega L_1}. \tag{4.10}$$

From (6.19) and (6.21), we obtain the expression of i_1 during turn-ON period as

$$\begin{aligned} i_1(\theta) = &\frac{V_I(\theta - 2\pi D) - \omega_1[A\sin(2\pi D\omega_1) - B\cos(2\pi D\omega_1)]}{\omega L_1} \\ &+ \frac{\omega_1^2 I_m \sin(2\pi D+\varphi)}{\omega_1^2 - 1} + \frac{\omega_1^2 I_2 \sin(6\pi D+\varphi_2)}{\omega_1^2 - 9} \end{aligned} \tag{4.11}$$

4.3.2 Boundary Conditions

The unknown constants A and B can be obtained from the boundary conditions of the waveform equations, which can be described as

$$i_1(0) = i_1(2\pi), \tag{4.12}$$

and

$$\left.\frac{di_1(\theta)}{d\theta}\right|_{\theta=0} = \left.\frac{di_1(\theta)}{d\theta}\right|_{\theta=2\pi}. \tag{4.13}$$

From (6.19) and (6.24)-(6.26), we obtain

$$A = \frac{1}{\omega C_1}\left(\frac{I_m \cos\varphi}{\omega_1^2 - 1} + \frac{3I_2 \cos\varphi_2}{\omega_1^2 - 9} - \frac{V_I}{\omega L_1 \omega_1^2}\right), \tag{4.14}$$

and

$$\begin{aligned} B =& \frac{1}{\omega C_1 \omega_1 [1 - \cos(2\pi D\omega_1)]}\left\{\frac{2\pi(1-D)V_I}{\omega L_1}\right. \\ & - \omega_1\left(\frac{I_m \cos\varphi}{\omega_1^2 - 1} + \frac{3I_2 \cos\varphi_2}{\omega_1^2 - 9} - \frac{V_I}{\omega L_1 \omega_1^2}\right)\sin(2\pi D\omega_1) \\ & + \frac{\omega_1^2 I_m[\sin(2\pi D + \varphi) - \sin\varphi]}{\omega_2 - 1} \\ & \left. + \frac{\omega_1^2 I_2[\sin(2\pi D + \varphi_2) - \sin\varphi_2]}{\omega_2 - 9}\right\}, \end{aligned} \tag{4.15}$$

4.3.3 Design Conditions

The L_2 and C_2 are in complete resonance with the resonant frequency of $3f$, shorting out the third harmonic current. Therefore, the third harmonic component in the switch voltage is eliminated. From the Fourier series expansion, we obtain

$$\frac{1}{\pi}\int_0^{2\pi} v_S(\theta)\sin(3\theta + \varphi_2) = 0, \tag{4.16}$$

and

$$\frac{1}{\pi}\int_0^{2\pi} v_S(\theta)\cos(3\theta + \varphi_2) = 0, \tag{4.17}$$

The L_3 and C_3 are tuned to pass only the fundamental frequency component but are designed to be slightly inductive to achieve the ZVS. Namely, from the Fourier series expansion, we obtain

$$\frac{1}{\pi}\int_0^{2\pi} v_S(\theta)\sin(\theta + \varphi) = R_L I_m = V_m, \tag{4.18}$$

and

$$\frac{1}{\pi}\int_0^{2\pi} v_S(\theta)\cos(\theta+\varphi) = \omega L_X I_m, \tag{4.19}$$

where V_m is the amplitude of the output voltage, and L_X is the extra inductive component.

To achieve the load-independent operation, the amplitude of the output voltage must be independent of the load resistance. Besides, the ZVS should be achieved at the turn-ON instant. Therefore, the following conditions must be simultaneously achieved.

$$\frac{dV_m}{dR_L} = 0, \tag{4.20}$$

and

$$v_S(2\pi D) = 0, \tag{4.21}$$

From (6.17), (6.20), and (6.27)-(6.31), values of I_m, I_2, ω_1, φ, φ_2, and L_X that achieves the load-independent operation are determined for fixed shunt capacitance C_1 and duty ratio D.

4.4 Experimental Verification

The design specifications of the load-independent class-Φ_3 inverter is given as switching frequency $f = 6.78$ MHz, input voltage $V_I = 25$ V, rated load resistance $R_{Lr} = 10\ \Omega$, and quality factor $Q_r = \omega L_3/R_{Lr} = 10$. The shunt capacitance C_1 and the OFF-duty ratio of the class-Φ_3 inverter were obtained as $C_1 = 222$ pF

and $D = 0.41$, respectively, for maximizing the power-output capability. Also, we experimented with the load-independent class-Φ_2 inverter in the same specifications for comparison.

Table 4.1 gives the component values, which are determined from the analysis provided in Section 6.4. Based on the design specifications and component values, we selected the passive component and devices, as given in Table 4.3. The selected switching device of GS61004B has an output capacitance of 110 pF with non-linearity. Therefore, the component values of the shunt capacitance C_1 in Table 4.1 have a relatively large difference between analytical and measured values. Fig. 4.4 shows an implemented class-Φ_3 inverter.

Fig. 6.11 shows the experimental and analytical waveforms of the load-independent class-Φ_2 and class-Φ_3 inverters for fixed load resistances. We can see that the experimental and analytical waveforms are in good agreement, confirming the validity of the analysis given in Section 6.4. We can see from Figs. 6.11(a)-(c) and 6.11(d)-(f) that both the load-independent class-Φ_2 and class-Φ_3 inverters achieved the ZVS and constant output-voltage amplitude against load variations. From these results, we confirmed that the load-independent design can also be realized in the class-Φ_3 inverter. The measured output powers of the load-independent class-Φ_2 and class-Φ_3 inverters at the rated condition were 42.4 W and 75.2 W, respectively. Namely, higher output power can be obtained in the load-independent class-Φ_3 at the same input voltage.

Fig. 6.6 shows the experimental and analytical characteristics of the load-independent class-Φ_2 and class-Φ_3 inverters as a function of normalized load resistance. The analytical power-conversion efficiency is derived considering the equivalent series resis-

tance of the inductors and ON-resistance of the switching device as the power-loss factors. We can see from Fig. 6.6(a) that the amplitude of the output voltage is constant against load variations in both the load-independent class-Φ_2 and class-Φ_3 inverters. Meanwhile, from Fig. 6.6(b), we can see that the load-independent class-Φ_3 inverter achieved higher efficiency than the load-independent class-Φ_2 inverter. This is because the power loss in the ESR of L_2 was higher in the load-independent class-Φ_2 design.

These results confirm that the load-independent class-Φ_3 inverter achieved the load-independent operation and improved efficiency than the load-independent class-Φ_2 inverter, demonstrating the effectiveness of the proposed design.

4.5 Performance Comparison

Table 4.3 gives the comparison between the load-independent class-Φ_2 and Φ_3 inverters. We can see from Table 4.3 that the class-Φ_2 inverter has lower switch-voltage stress for a given input voltage. The switch-current stresses are comparable for the two inverters. Meanwhile, the load-independent class-Φ_3 inverter has a larger output voltage for the same input voltage than the load-independent class-Φ_2 inverter. Consequently, the load-independent class-Φ_3 inverter achieves an improved power-output capability of 0.137.

4.6 Conclusion

This chapter has proposed the design of the load-independent class-Φ_3 inverter. The load-independent class-Φ_3 inverter achieves the ZVS and constant AC output voltage regardless of the load resistance. Additionally, it achieves higher efficiency and power-output capability than the load-independent class-Φ_2 inverter. In the experiment, the load-independent class-Φ_3 inverter achieved 87.5 %-95.9 % power-conversion efficiency within a tenfold change in the load resistance, showing the effectiveness of the proposed inverter.

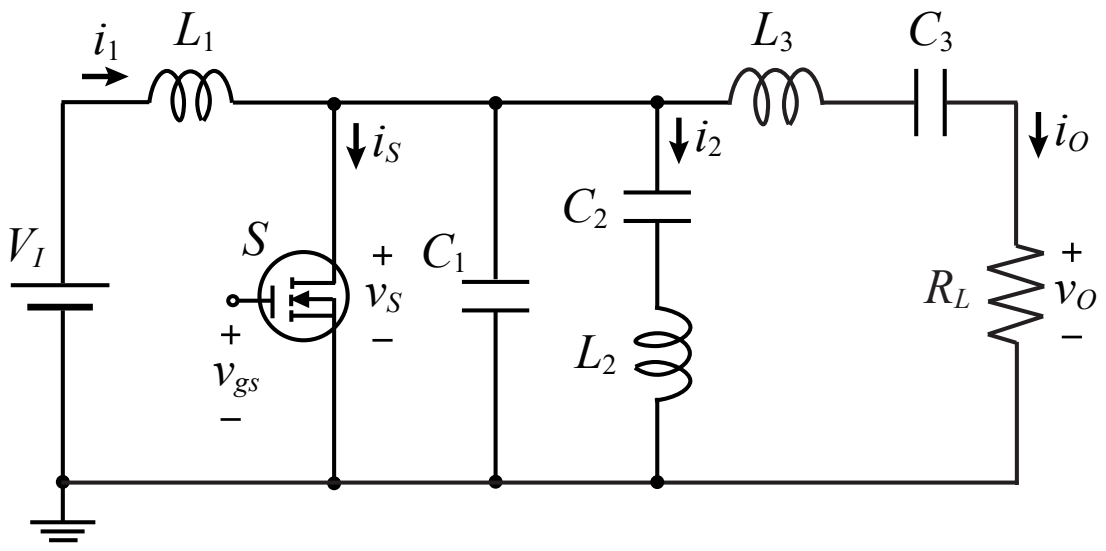

Fig. 4.1: Circuit topology of the load-independent class-Φ_2 and class-Φ_3 inverters.

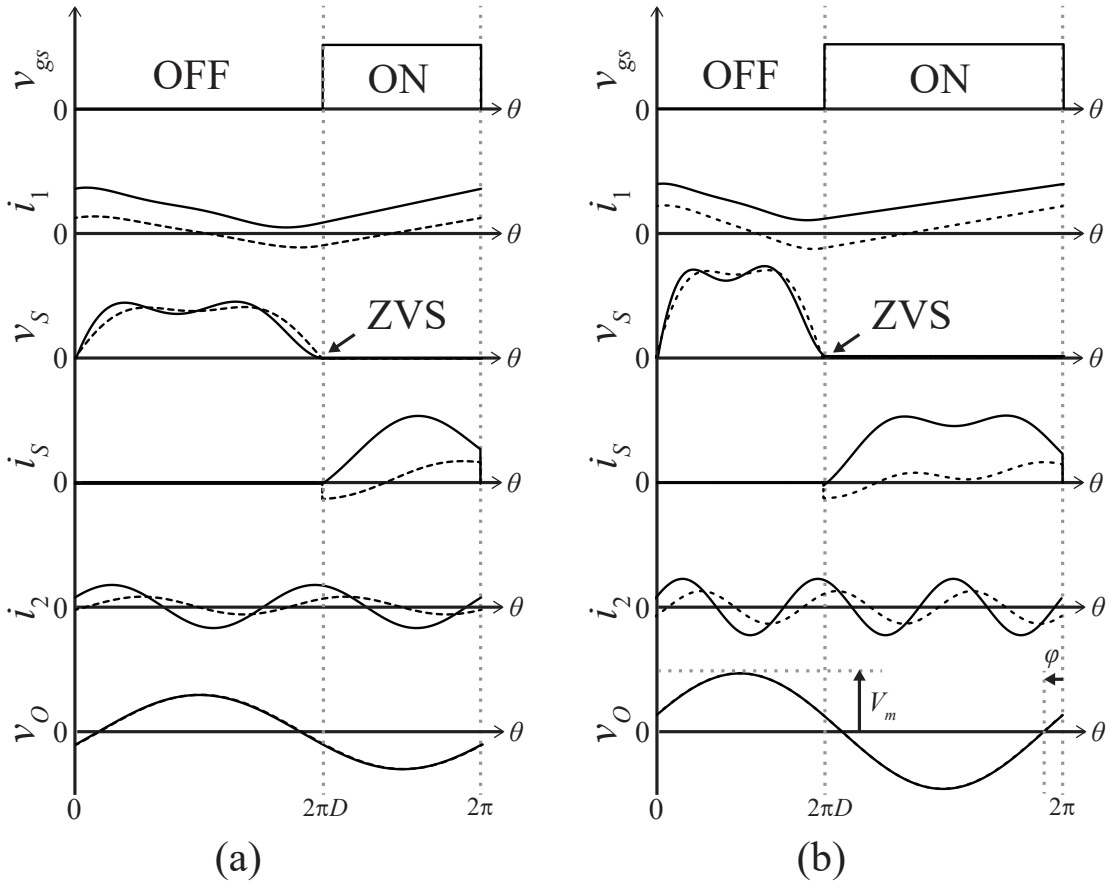

Fig. 4.2: Example waveforms for fixed load resistance (solid line: $R_L/R_{Lr} = 1$, dashed line: $R_L/R_{Lr} = 10$). (a) Load-independent class-Φ_2 inverter. (b) Load-independent class-Φ_3 inverter.

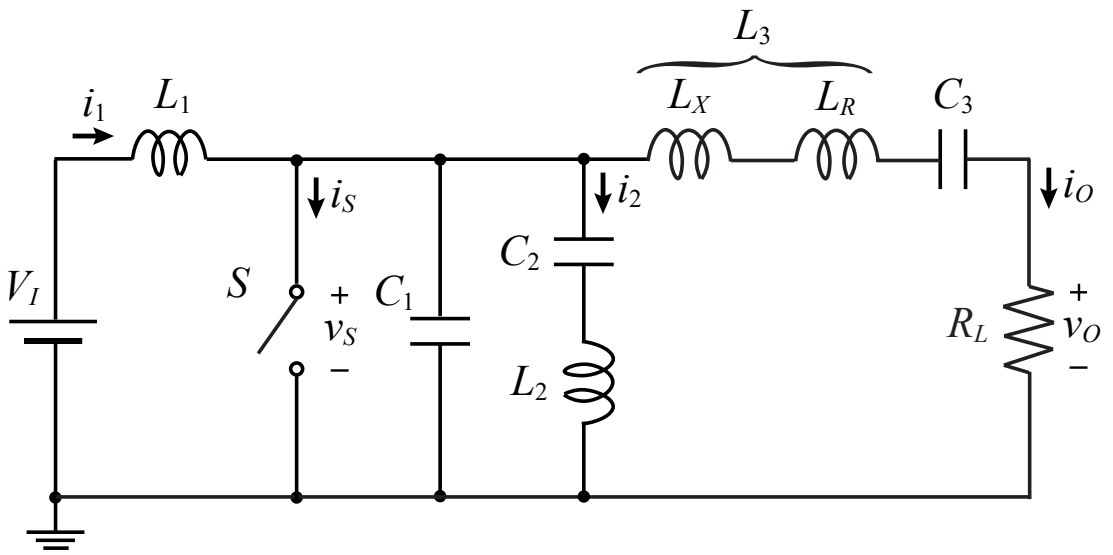

Fig. 4.3: Analytical circuit model of the class-Φ_3 inverter.

Table 4.1: Analytical and experimental component values.

	Class-Φ_2 inverter		Class-Φ_3 inverter	
	Analytical	Measured	Analytical	Measured
L_1	532 nH	534 nH	834 nH	832 nH
L_2	1761 nH	1770 nH	1174 nH	1170 nH
L_3	2347 nH	2333 nH	2347 nH	2333 nH
C_1	535 pF	222 pF	222 pF	0 pF
C_2	78 pF	52 pF	52 pF	46 pF
C_3	239 pF	237 pF	237 pF	233 pF

Table 4.2: Components and devices used on the PCB.

	Parts number	Manufacturer
Switching device	GS61004B	GaN Systems
Load resistance	TEH100	Ohmite
Resonant capacitors	S111DUE	Johanson Technology
Magnetic core for L_1	T50-6	Micrometals
Magnetic core for L_2	T50-6	Micrometals
Magnetic core for L_2	T80-6	Micrometals

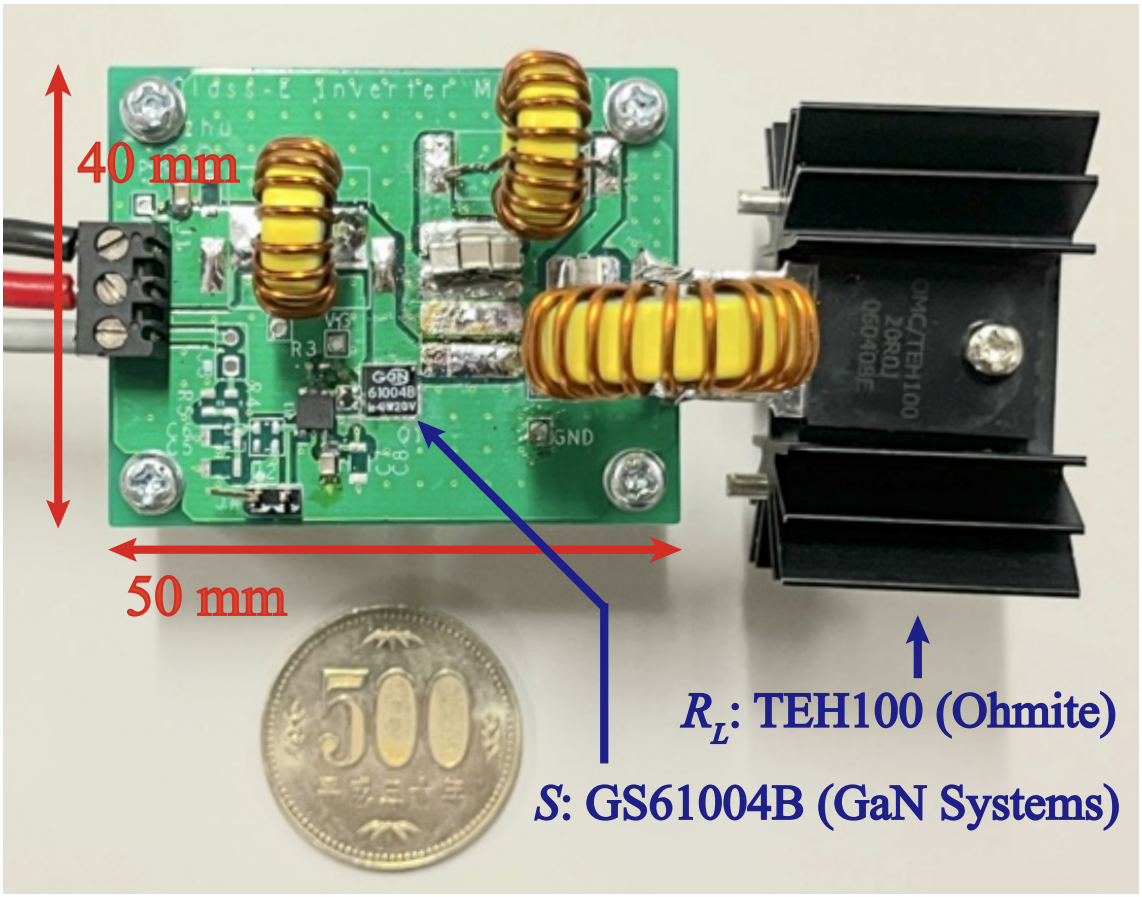

Fig. 4.4: Photo of the implemented load-independent class-Φ_3 inverter.

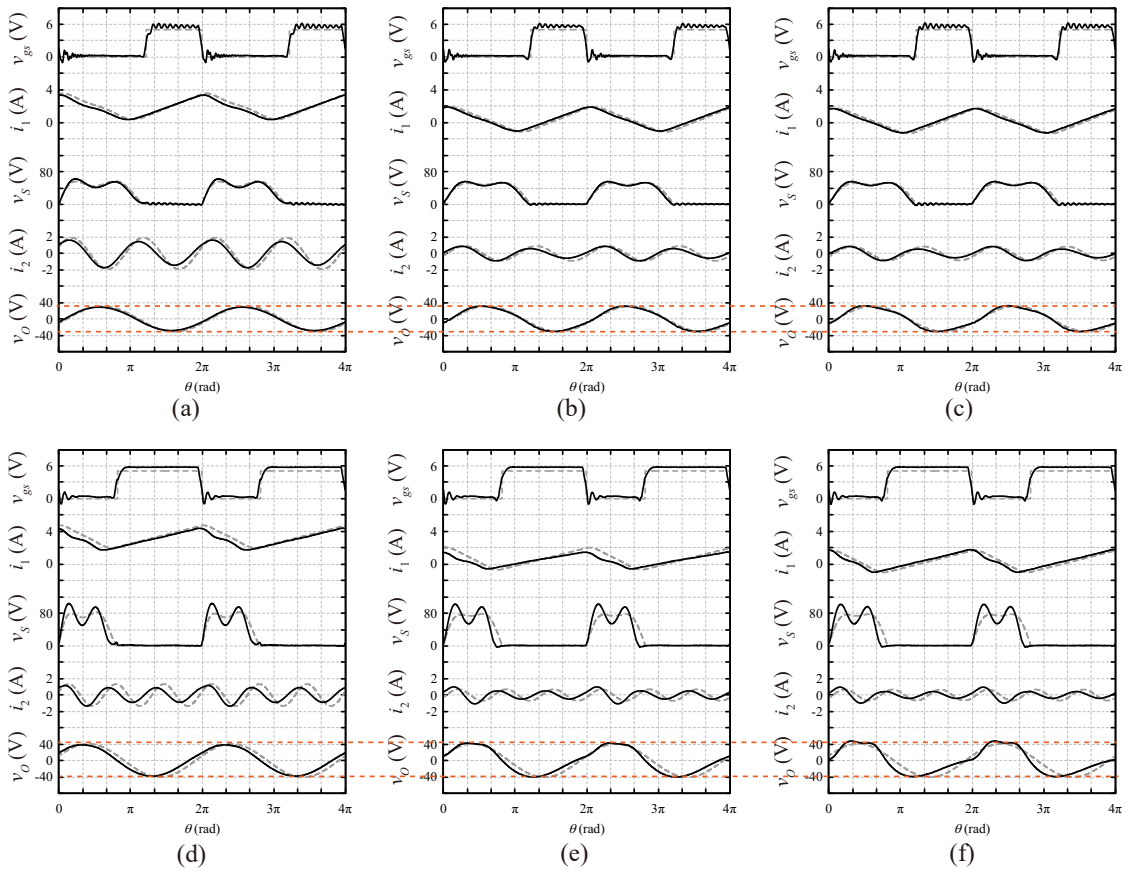

Fig. 4.5: Superimposed experimental and analytical waveforms for fixed load resistance (solid line: experiment, dashed line: analytical). (a)-(c) Load-independent class-Φ_2 inverter. (d)-(f) Load-independent class-Φ_3 inverter. (a) and (d) For $R_L/R_{Lr} = 1$. (b) and (e) For $R_L/R_{Lr} = 5$. (c) and (f) For $R_L/R_{Lr} = 10$.

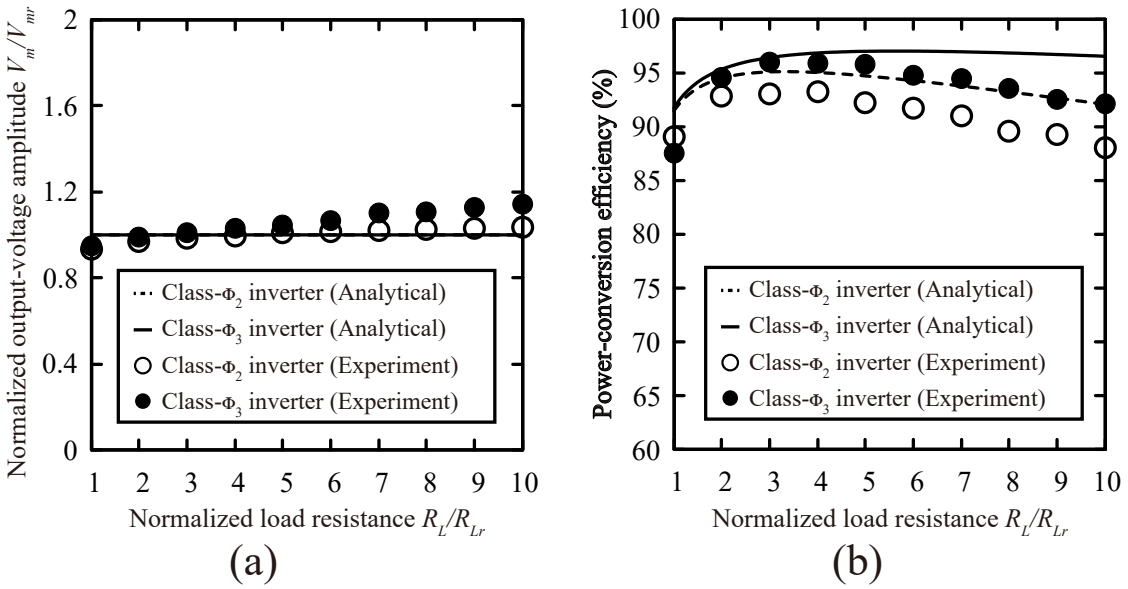

Fig. 4.6: Circuit characteristics as a function of normalized load resistance. (a) Normalized output-voltage amplitude. (b) Power-conversion efficiency.

Table 4.3: Comparison between the load-independent class-Φ_2 and class-Φ_3 inverters.

	Switch-voltage stress	Switch-current stress	Output-voltage amplitude	Power-output capability	Power-conversion efficiency
Load-independent class-Φ_2 inverter	2.27 V_I	2.94 R_{Lr}/V_I	1.24 V_I	0.116	88.0%-93.2%
Load-independent class-Φ_3 inverter	3.31 V_I	2.95 R_{Lr}/V_I	1.63 V_I	0.137	87.5%-95.9%

References

[1] R. S. Pengelly, S. M. Wood, J. W. Milligan, S. T. Sheppard, and W. L. Pribble, "A review of GaN on SiC high electron-mobility power transistors and MMICs," IEEE Trans. Microw. Theory Techn., vol. 60, no. 6, pp. 1764-1783, 2012.

[2] N. O. Sokal and A. D. Sokal, "Class E-A new class of high-efficiency tuned single-ended switching power amplifiers," IEEE J. Solid-State Circuits, vol. 10, no. 3, pp. 168-176, 1975.

[3] K. H. Liu and F. C. Y. Lee, "Zero-voltage switching technique in DC/DC converters," IEEE Trans. Power Electron., vol. 5, no. 3, pp. 293-304, 1990.

[4] Y. Li, X. Ruan, L. Zhang, and Y.-K. Lo, "Multipower-level hysteresis control for the Class E DC-DC converters," IEEE Trans. Power Electron., vol. 35, no. 5, pp. 5279-5289, 2020.

[5] Y. Zhou and J. Choi, "Design of high-frequency, load-independent resonant inverter using phase-shift control method," in Proc. IEEE Appl. Power Electron. Conf. Expo. (APEC), 2023, pp. 1070-1076.

[6] R. Zulinski and K. Grady, "Load-independent class E power inverters. I. theoretical development," IEEE Trans. Circuits Syst., vol. 37, no. 8, pp. 1010-1018, 1990.

[7] S.Aldhaher, D.C.Yates, and P.D.Mitcheson, "Load-independent Class E/EF inverters and rectifiers for MHz-switching applications," IEEE Trans. Power Electron., vol. 33, no. 10, pp. 8270-8287, 2018.

[8] H. Sekiya, K. Tokano, W. Zhu, Y. Komiyama, and K. Nguyen, "Design procedure of load-independent class-E WPT systems and its application in robot arm," IEEE Trans. Ind. Electron., vol. 70, no. 10, pp. 10014-10023, 2023.

[9] X. Huang, Y. Lin, Y. Dou, S. Lin, and J. Huang, "Load-independent push-pull class-Φ 2 inverter with single compact three-winding inductor," IEEE Trans. Power Electron., vol. 38, no. 10, pp. 11 916-11 927, 2023.

[10] Y. Zhou and J. Choi, "High-frequency inverter design for a wide range of resistive and reactive load variation," in Proc. IEEE Energy Conv. Congr. Expo. (ECCE), 2023, pp. 3537-3544.

[11] J. Rivas, O. Leitermann, Y. Han, and D. Perreault, "A very high frequency DC-DC converter based on a class Φ 2 resonant inverter," IEEE Trans. Power Electron., vol. 26, no. 10, pp. 2980-2992, 2011.

[12] L. Raymond, W. Liang, J. Choi, and J. Rivas, "27.12 MHz large voltage gain resonant converter with low voltage stress," in Proc. IEEE Energy Conv. Congr. Expo., 2013, pp. 1814-1821.

[13] L. Roslaniec, A. Jurkov, A. Bastami, and D. Perreault, "Design of single-switch inverters for variable resistance/load modulation operation," IEEE Trans. Power Electron., vol. 30, no. 6, pp. 3200-3214, 2015.

[14] H. Sekiya, J. Ma, K. Nguyen, and X. Wei, "Design of class-Φ 3 inverter," in Proc. 2020 Int. SoC Design Conf. (ISOCC), 2020, pp. 179-180.

[15] S. Pezeshkpour and M. M. Ahmadi, "Design procedure for a high-efficiency class-E/F3 power amplifier," IEEE Trans. Power Electron., vol. 38, no. 11, pp. 14 388-14 399, 2023.

[16] J. Ma, Asiya, X. Wei, K. Nguyen, and H. Sekiya, "Analysis and design of generalized class-E/F2 and class-E/F3 inverters," IEEE Access, vol. 8, pp. 61 277-61 288, 2020.

Chapter 5

Load-Independent Class-E^{-1} Power Oscillator

The class-E inverter is used in an extensive range of applications, such as induction heatings [1], DC-DC converters [2], and WPT systems [3]. The class-E inverter has only one switch with a grounded source terminal, which allows high-frequency operation in the megahertz band. However, the class-E inverter is highly sensitive to component values [4, 5], which means that it cannot maintain high efficiency and constant output for variations, including component tolerances and load variations.

For obtaining the robustness against component tolerances in the resonant filter, the frequency-modulation control is applied to the class-E inverter [6]. The class-E inverter improves the efficiency against the component tolerances by tuning the operating frequency. However, it requires a digital control system, which increases the cost and complexity. The self-tuned oscillator [7] realizes the frequency tuning without external digital controls. The self-tuning feedback loop provides the gate-driving voltage with almost the constant phase shift, realizing the same function as the frequency-modulation control [6] without control. Although the self-tuned oscillator has solved the problem of resonant-component tolerances, it is still sensitive

to load-resistance variations.

The load-independent class-E inverter [8–11] is a simple solution for maintaining high efficiency and constant output against load-resistance variations without any control. The class-E inverter can acquire robustness to load-resistance variations by designing specific component values to satisfy the load-independent conditions [8–10]. For obtaining the robustness against both the resistive and reactance component variations in the resonant filter, the load-independent-designed self-tuned oscillator is proposed [12,13]. These oscillators provide constant gate-driving voltage against load variations, keeping the load-independent operation even with the component tolerances. Although the self-tuned load-independent oscillator is robust to both resistive and reactance component variations, there is no series-resonant-type oscillator that is suitable for the transmitter circuit of the WPT systems.

This chapter proposes the self-tuned series resonant power oscillator with load-independent operation. The proposed circuit is the first self-tuned load-independent oscillator with a series resonant filter. The proposed power oscillator is derived from the load-independent CC/ZCS inverter [10]. The proposed circuit achieves CC output and high efficiency against load-resistance variations and component tolerances by adding the self-tuned feedback network. The design method of the proposed oscillator is presented in this chapter. The experimental results show the effectiveness of the proposed power oscillator.

5.1 Load-Independent CC/ZCS inverter

Fig. 5.1 shows the circuit topology and operating waveforms of the load-independent CC/ZCS inverter [10] with duty ratio $D = 0.5$. The load-independent CC/ZCS inverter is composed of the voltage source V_I, choke coil L_C, switching device S, series inductance L_S, shunt capacitance C_S, and series resonant filter $L_0 - C_0 - R_L$. The load-independent CC/ZCS inverter achieves the ZCS and constant CC output regardless of the load resistance, as shown in Fig. 5.1(b), where $\theta = \omega t = 2\pi f t$ is the angular displacement and f is the operating frequency, and the subscript 'r' in R_{Lr} indicates the rated value. For achieving the load-independent operatin [8–11], the inverter must satisfy

$$\varphi = \pi - \pi D, \tag{5.1}$$

and

$$1 - \cos\left(\frac{2\pi D}{\omega\sqrt{L_S C_S}}\right) + \frac{\pi(1-D)}{\omega\sqrt{L_S C_S}} \sin\left(\frac{2\pi D}{\omega\sqrt{L_S C_S}}\right) = 0, \tag{5.2}$$

where φ is the phase shift between the output current and gate-drive voltage. Namely, the load-independent CC/ZCS inverter has a phase shift $\varphi = \pi/2$ for $D = 0.5$, as shown in Fig. 5.1(b).

Although the load-independent CC/ZCS inverter has excellent robustness for load-resistance variations, it has a high sensitivity for component tolerances in the resonant filter due to a high-quality factor defined as $Q = \omega L_0/R_L$. Fig. 5.2(a) and (b) shows the switch-current waveforms of the load-independent CC/ZCS inverter against variations in resonant inductance for fixed load resistance. We can see that the non-ZCS waveforms appeared when $L_0/L_{0r} = 0.9$. Besides, the reverse cur-

rent increases for $L_0/L_{0r} = 1.1$, especially at light load. These deteriorations in switch-current waveform decrease the power-conversion efficiency.

5.2 Proposed oscillator

Fig. 5.3 shows the circuit topology and operating waveforms of the proposed oscillator. The proposed oscillator consists of the load-independent CC/ZCS inverter [10] with an additional self-tuned feedback network, as shown in Fig. 5.3(a). The feedback network is composed of a blocking capacitance C_B and voltage-dividing resistances R_{d1} and R_{d2} for generating the bias voltage of the switch V_{th}. In the load-independent CC/ZCS inverter, the voltage across the resonant capacitance v_{C2} is in the same phase as the gate-drive voltage because the output current has a phase shift of $\varphi = \pi/2$ for $D = 0.5$. The proposed oscillator uses this property to produce the gate-driving voltage by feeding back the voltage across the resonant capacitance, as shown in Fig. 5.3(b).

Based on the proposed feedback network, the proposed oscillator autonomously tunes the operating frequency to the resonant one. The self-tuning can be realized because the phase shift of the feedback voltage is independent of the operating frequency. Therefore, the proposed oscillator has robustness against the component tolerances in the resonant filter. Moreover, self-tuning can be achieved even when load-resistance variations occur. This is because the phase shift of the feedback voltage is fixed for load-resistance variations due to the load-independent operation [8–11]. Namely, the proposed oscillator is robust to simultaneous variations in load resistance and component tolerances.

Fig. 5.2(c) and (d) show the example waveforms of the proposed oscillator against variations in resonant inductance for fixed load resistance. We can see that the non-ZCS waveforms in Fig. 5.2(a) and (b) are mitigated in Fig. 5.2(c) and (d) by the self-tuning. Also, the reverse current is suppressed in Fig. 5.2(c) and (d). The switch-current waveform of the proposed oscillator has small changes against L_0 variations, resulting in stable circuit operation. Therefore, it can be said that the proposed oscillator overcomes the sensitivity problem in the component tolerances through the self-tuning feedback network.

5.3 Circuit design

In this chapter, we design the proposed oscillator from the given specification of input voltage V_I, rated load resistance R_{Lr}, operating frequency f, and quality factor Q. Firstly, the load-independent CC/ZCS inverter with $D = 0.5$ is designed for the proposed oscillator. From [10], the component values are derived as

$$C_S = \frac{0.96424}{\omega R_{Lr}}, \tag{5.3}$$

$$L_S = \frac{0.62172 R_{Lr}}{\omega}, \tag{5.4}$$

$$L_0 = \frac{Q R_{Lr}}{\omega}, \tag{5.5}$$

and

$$C_0 = \frac{1}{\omega R_{Lr}(Q - 1.3132)}. \tag{5.6}$$

The amplitude of the output current I_m is

$$I_m = \frac{1.2133 V_I}{R_{Lr}}. \tag{5.7}$$

Second, the component value in the feedback network is derived. The resistances R_{d1} and R_{d2} are used for producing the bias voltage for the switch. Namely, they satisfy

$$V_{th} = \frac{R_{d2} V_I}{R_{d1} + R_{d2}}. \tag{5.8}$$

Besides, R_{d1} and R_{d2} need to be large enough so that the current flowing through them can be ignored. Also, C_B should be large enough to block the DC. The capacitance C_1 and C_2 are divided to adjust the amplitude of the gate-driving voltage. By considering the maximum absolute of the gate-driving voltage V_{gsmax}, C_2 and C_1 are designed as

$$C_2 \geq \frac{I_m}{\omega(V_{gsmax} - V_{th})}, \tag{5.9}$$

and

$$C_1 = \frac{C_0 C_2}{C_2 - C_0}. \tag{5.10}$$

5.4 Experimental verifications

The design specifications of the proposed oscillator were given as $V_I = 30$ V, $R_{Lr} = 50\ \Omega$, $f = 1$ MHz, and $Q = 5$. We chose the GS66504B from GaN Systems as the switching device, whose threshold voltage $V_{th} = 1.7$ V and ON resistance $r_{ON} = 0.16\ \Omega$. The powder iron core T106-2 and T200-2 from Micrometals were used

for series inductance L_S and resonant inductance L_0, whose ESR were $r_{L_S} = 0.118\ \Omega$ and $r_{L_0} = 0.306\ \Omega$, respectively. Also, the shielded power inductor MSS1210H from Coilcraft was used as the choke coil L_C. Table 7.1 shows the component values of the implemented oscillator. Fig. 5.4 shows the photo of the experimental prototype. In this chapter, we also conducted the experiment for the load-independent CC/ZCS inverter with the same specifications for comparison.

Fig. 5.5 shows the experimental waveforms of the load-independent CC/ZCS inverter against load-resistance variations for fixed resonant inductance. We can see from Fig. 5.5(b) that the switch current achieved ZCS and the output-current amplitude was constant against load-resistance variations. However, the non-ZCS waveforms appeared in Fig. 5.5(a), and the reverse current increased in Fig. 5.5(c). We can state that the load-independent CC/ZCS inverter has high sensitivity against L_0 variations.

Fig. 5.6 shows the analytical and experimental waveforms of the proposed oscillator against load-resistance variations for fixed resonant inductance. The analytical waveforms are derived based on the circuit analysis in [8]. We can see from Fig. 5.6(b) and (e) that the load-independent ZCS and CC output were achieved for the rated resonant inductance. Moreover, we can see from Fig. 5.6(a) and (d) that the ZCS was achieved even with the L_0 variations. Besides, the reverse current in Fig. 5.5(c) was suppressed in Fig. 5.6(c) and (f). The measured operating frequency in the rated load was $f = 1.003$ MHz at $L_0/L_{0r} = 1$, $f = 1.052$ MHz at $L_0/L_{0r} = 0.9$, and $f = 0.9708$ MHz at $L_0/L_{0r} = 1.1$. Thus, we can say that the self-tuning worked well in the proposed oscillator, improving the characteristics against component tolerances in the resonant filter. The agreement of the analytical

and experimental waveforms showed the validity of the proposed design method.

Fig. 7.5 shows the normalized output-current amplitude and the power-conversion efficiency as a function of the load resistance. The analytical efficiency is calculated by using the power-loss analysis in [14]. We consider the power loss, including the ESRs of L_C, L_S and L_0, switch ON-resistance, and switching loss caused by the non-ZCS. We can see from Fig. 7.5(b) that the flat characteristics of the output-current amplitude and high efficiency against load-resistance variations were obtained in both the load-independent CC/ZCS inverter and the proposed oscillator. In addition, we can see from Fig. 7.5(a) and (c) that the proposed oscillator kept high efficiency even with the deviations in L_0, especially at light load compared with the load-independent CC/ZCS inverter. We can conclude that the proposed oscillator has excellent load characteristics even with the variations in the resonant component, showing the effectiveness of the proposed topology. The proposed oscillator achieved 95.0 % efficiency with 12 W output power in 1MHz operation.

5.5 Conclusion

This chapter has proposed the self-tuned series resonant power oscillator with load-independent operation. The proposed oscillator maintains high efficiency and constant AC output even with load variations and component tolerances. The experimental results show the effectiveness of the proposed power oscillator.

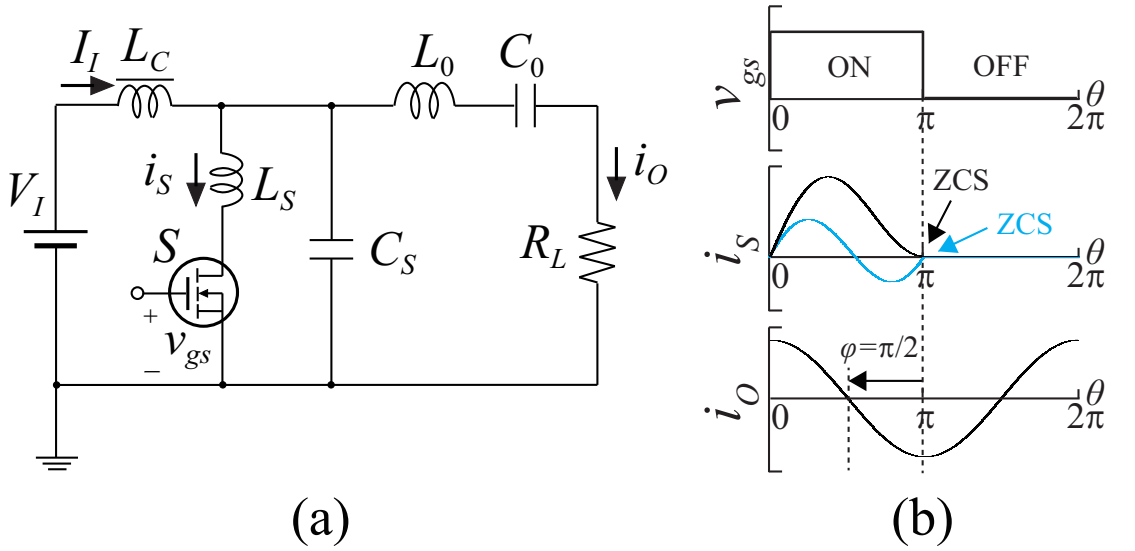

Fig. 5.1: The load-independent CC/ZCS inverter. (a) Circuit topology. (b) Operating waveforms. (Black line: $R_L/R_{Lr} = 1$ and blue line: $R_L/R_{Lr} = 0.1$.)

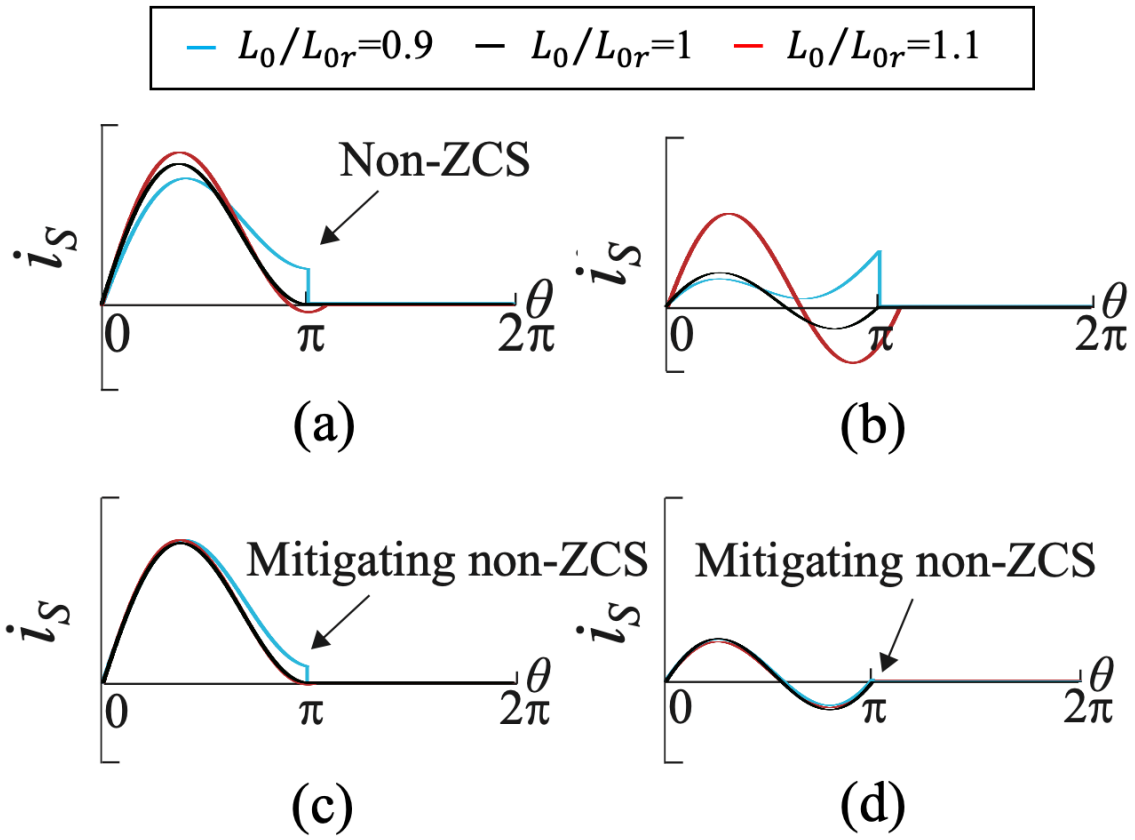

Fig. 5.2: The switch-current waveforms against variations in resonant inductance for fixed load resistance. (a) For load-independent CC/ZCS invertert at $R_L/R_{Lr} = 1$. (b) For load-independent CC/ZCS invertert at $R_L/R_{Lr} = 0.1$. (c) For proposed oscillator at $R_L/R_{Lr} = 1$. (d) For proposed oscillator at $R_L/R_{Lr} = 0.1$.

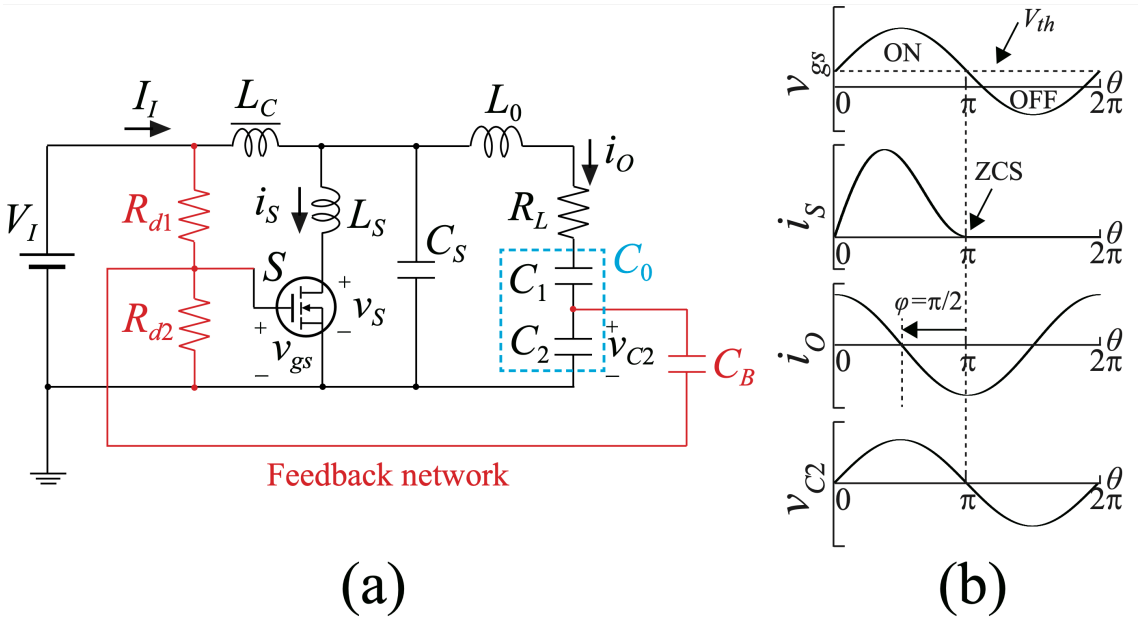

Fig. 5.3: The proposed oscillator. (a) Circuit topology. (b) Operating waveforms.

Table 5.1: Analytical and measured component values.

	Analytical	Measured		Analytical	Measured
L_C	-	154.0 μH	C_S	3069 pF	3066 pF
L_S	4.947 μH	4.994 μH	C_B	-	1.014 μF
L_0	39.79 μH	39.89 μH	R_{d1}	10.00 kΩ	10.12 kΩ
C_1	886.5 pF	886.6 pF	R_{d2}	166.5 kΩ	160.0 kΩ
C_2	33.04 nF	36.04 nF	R_{Lr}	50.00 Ω	50.10 Ω

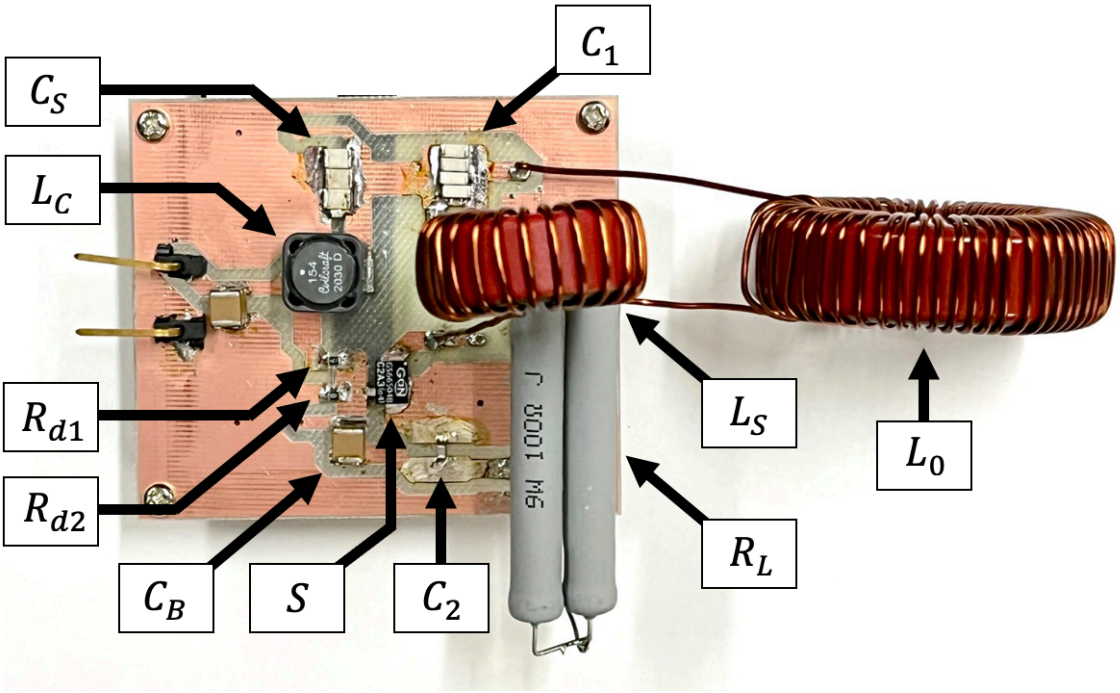

Fig. 5.4: Photo of the implemented proposed oscillator.

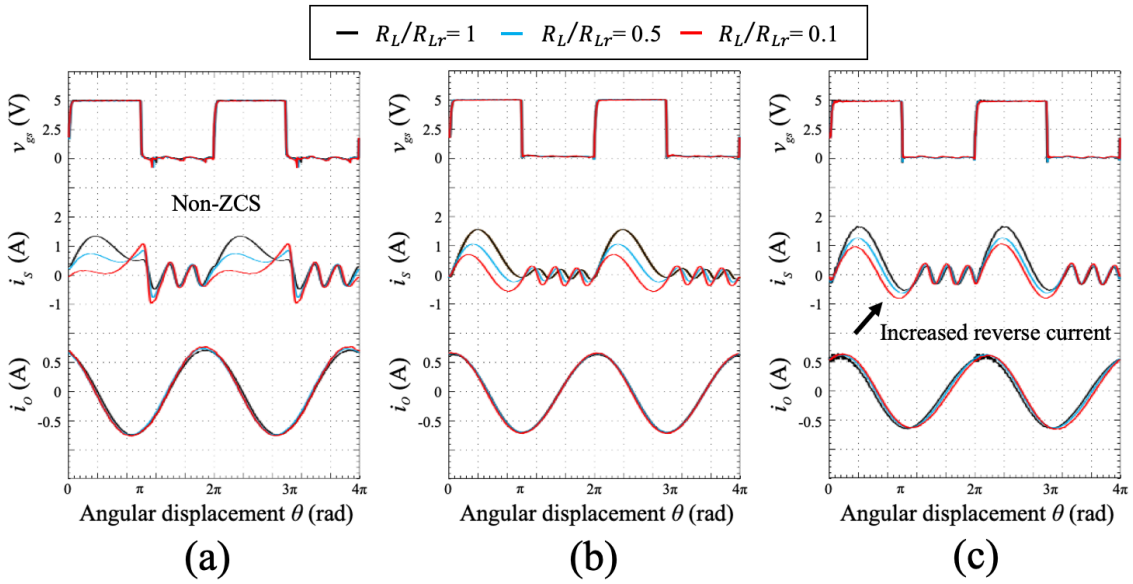

Fig. 5.5: The experimental waveforms of the load-independent CC/ZCS inverter against load-resistance variations for fixed resonant inductance. (a) For $L_0/L_{0r} = 0.9$. (b) For $L_0/L_{0r} = 1$. (c) For $L_0/L_{0r} = 1.1$.

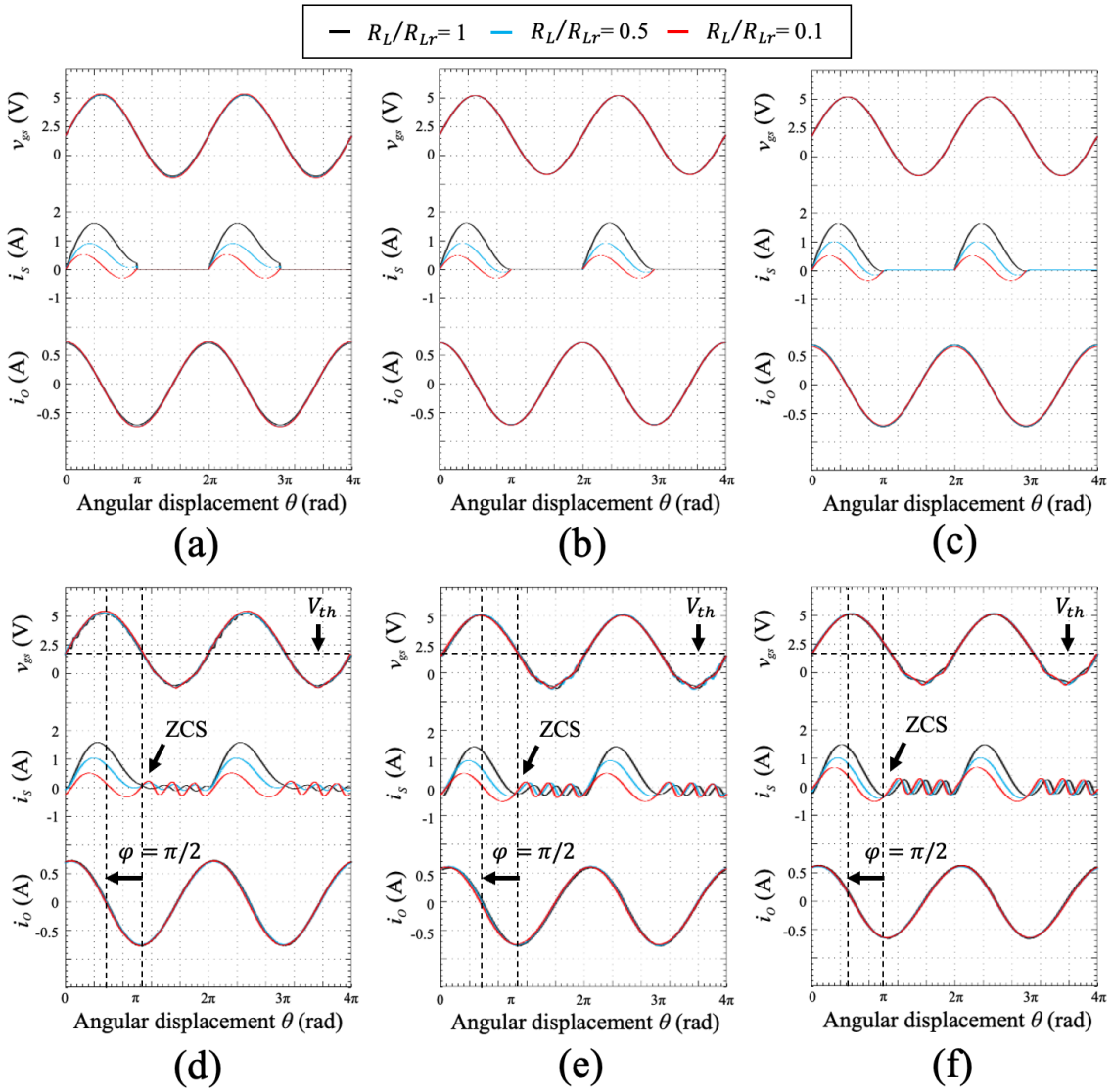

Fig. 5.6: The waveforms of the proposed oscillator against load-resistance variations for fixed resonant inductance. (a) Analytical waveforms for $L_0/L_{0r} = 0.9$. (b) Analytical waveforms for $L_0/L_{0r} = 1$. (c) Analytical waveforms for $L_0/L_{0r} = 1.1$. (d) Experimental waveforms for $L_0/L_{0r} = 0.9$. (e) Experimental waveforms for $L_0/L_{0r} = 1$. (f) Experimental waveforms for $L_0/L_{0r} = 1.1$.

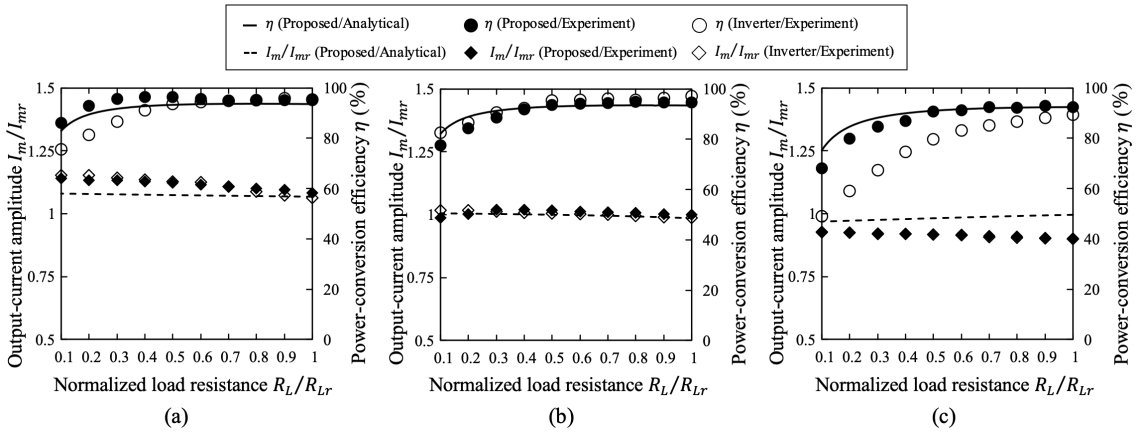

Fig. 5.7: The normalized output-current amplitude and the power-conversion efficiency as a functinos of the load resistance. (a) For $L_0/L_{0r} = 0.9$. (b) For $L_0/L_{0r} = 1$. (c) For $L_0/L_{0r} = 1.1$.

References

[1] H. Sarnago, O. Lucía, A. Mediano, and J. M. Burdío, "A class-E direct AC-AC converter with multicycle modulation for induction heating systems," *IEEE Trans. Ind. Electron*, vol. 61, no. 5, pp. 2521-2530, May 2014.

[2] N. Weitz, S. Utzelmann, S. Ditze, and M. März, "A resonant push-pull DC-DC converter With an intrinsic current source behavior for radio frequency power conversion," *IEEE Trans. Power Electron.*, vol. 37, no. 6, pp. 7001-7012, Jun. 2022.

[3] J. Arteaga, S. Aldhaher, G. Kkelis, C. Kwan, D. Yates, and P. Mitcheson, "Dynamic capabilities of multi-MHz inductive power transfer systems demonstrated with batteryless drones," *IEEE Trans. Power Electron.*, vol. 34, no. 6, pp. 5093-5104, Jun. 2019.

[4] F. Raab, "Effects of circuit variations on the class E tuned power amplifier," *IEEE J. Solid-State Circuits*, vol. 13, no. 2, pp. 239-247, Apr. 1978.

[5] T. Mury and V. Fusco, "Sensitivity characteristics of inverse class-E power amplifier," *IEEE Trans. Circuits Syst. I: Reg. Papers*, vol. 54, no. 4, pp. 768-778, Apr. 2007.

[6] Y. Komiyama, S. Matsuhashi, W. Zhu, T. Mishima, Y. Ito, T. Uematsu, K. Nguyen, and H. Sekiya, "Frequency-modulation controlled load-independent class-E inverter," *IEEE Access*, vol. 9, pp. 144600-144613, 2021.

[7] M. Ahmadi and M. Salehi-Sirzar, "A self-tuned class-E power oscillator," *IEEE Trans. Power Electron.*, vol. 34, no. 5, pp. 4434-4449, May, 2019.

[8] S. Aldhaher, D. Yates, and P. Mitcheson, "Load-independent class E/EF inverters and rectifiers for MHz-switching applications," *IEEE Trans. Power Electron.*, vol. 33, no. 10, pp. 8270-8287, Oct. 2018.

[9] R. Zulinski and K. Grady, "Load-independent class E power inverters. I. theoretical development," *IEEE Trans. Circuits Syst.*, vol. 37, no. 8, pp. 1010-1018, Aug. 1990.

[10] "Load-independent constant-current/zero-current switching inverter with series resonant filter," in *Proc. IEEE Appl. Power Electron. Conf. Expo. (APEC)*, Mar. 2023. (Not yet published.)

[11] X. Huang, Z. Yu, Y. Dou, S. Lin, Z. Ouyang, and M. Andersen, "Load-independent push-pull class E^2 topology with coupled inductors for MHz-WPT applications," *IEEE Trans. Power Electron.*, vol. 37, no. 7, pp. 8726-8737, Jul. 2022.

[12] S. Matsuhashi, Y. Hara, K. Nguyen, H. Sekiya, T. Uematsu, S. Nagaoka, and T. Mishima, "Load-independent self-tuned parallel resonant power oscillator," in *Proc. IEEE Energy Convers. Congr. Expo. (ECCE)*, Detroit, MI, USA, 2020, pp. 1571-1576.

[13] Y. Komiyama, S. Matsuhashi, W. Zhu, K. Nguyen, and H. Sekiya, "Load-independent inverse class-E oscillator with Armstrong-oscillator based topology," in *Proc. Int. SoC Design Conf. (ISOCC)*, 2021, pp. 175-176.

[14] T. Nagashima, X. Wei, T. Suetsugu, M. Kazimierczuk, and H. Sekiya, "Waveform equations, output power, and power conversion efficiency for class-E inverter outside nominal operation," *IEEE Trans. Ind. Electron.*, vol. 61, no. 4, pp. 1799-1810, Apr. 2014.

Chapter 6

Load-Independent Class-E Power Oscillator

6.1 Introduction

The development of wide-bandgap power semiconductor devices, such as GaN and SiC, have accelerated developments of high-frequency inverters [1]. The passive components require less energy storage in high-frequency operation, allowing for physical size and weight reduction. Accordingly, high-frequency inverters increase the power density of the overall circuit. However, the higher frequency causes larger switching losses, which impose the requirement for achieving ZVS. Additionally, in practical applications, such as WPT systems and DC/DC converters, the load variations should be considered in the design [2, 3].

Within the above context, the load-independent class-E inverter [4] has attracted attention. The load-independent class-E inverter inherently achieves the ZVS and constant amplitude of the output voltage against resistive load variations. Therefore, no additional circuits and controls are required to maintain the ZVS and output regulation, simplifying the overall circuit configuration. The load-independent oper-

ation can be attained using a specific set of component values. The design conditions to achieve the load-independent operation are analytically revealed [5], which enables implementation of the load-independent class-E inverter for a wide range of applications and specifications [6–8].

The class-E power oscillator [9–13] is a variant of the class-E inverter, which autonomously oscillates by adding a passive feedback network. The class-E power oscillator generates the gate-drive voltage using the output AC voltage. Therefore, the feedback network needs to compensate for the phase shift between the output and gate-drive voltages. The class-E power oscillator works without the gate-drive circuits, including a crystal oscillator, gate driver, and additional power supplies, which further promotes circuit simplification and cost reduction. Although the class-E power oscillator achieves high efficiency due to the ZVS at the nominal state, its performance seriously degrades against load variations [11]. The load variations affect overall circuit operation, including efficiency deterioration due to the non-ZVS, fluctuations in output voltage and current, and, to make matters worse, the oscillation stops. Various types of the power oscillators, such as class-E [9–13] and class-E/F [14, 15] power oscillators, have been proposed so far. Nevertheless, all these power oscillators achieve optimal performance only within an extremely narrow range of load variations. Addressing load variations is a critical issue for making power oscillators more practical, which motivates enhancing the robustness of the class-E power oscillator.

This chapter proposes the load-independent class-E power oscillator. The load-independent class-E inverter is incorporated into the power oscillator by introducing the feedback network using the LCCL filter. The LCCL filter compensates for the

phase shift between the output and gate-drive voltages of the load-independent class-E inverter. Furthermore, the input impedance of the LCCL filter becomes purely resistive, which does not interfere with the load-independent operation of the inverter. Consequently, the proposed power oscillator obtains load independence in ZVS, output current, and gate-drive voltage. The proposed circuit works with high stability and efficiency over a wide load range, overcoming the sensitivity issue against load variations in the power oscillator. An analytical investigation of the proposed power oscillator is provided to reveal design conditions for achieving the load-independent operation. This chapter also gives closed-form design equations of the load-independent class-E power oscillator. The experimental verifications were carried out at 6.78 MHz oscillation frequency. The measured waveforms were quantitatively agreed with the analytical one, confirming the validity of the experiment.

6.2 Conventional Class-E Power Oscillator

Fig. 6.1 shows the circuit topology of the class-E power oscillator, which consists of the class-E inverter and the feedback network. The class-E power oscillator forms a closed loop with the passive components, and an external oscillator is unnecessary to drive the switch.

Fig. 6.2 shows the example waveforms of the class-E power oscillator, where $\theta = \omega_S t = 2\pi f_S t$ is the angular time, ω_S denotes the angular oscillation frequency, and f_S represents oscillation frequency. The switch is driven by the excitation of the biased sinusoidal voltage v_{gs}, which is generated using the output AC voltage v_O. To induce the sustained oscillation, the total phase shift in the closed loop must be an integer

multiple of 2π. Meanwhile, the nominal phase shift of the output voltage is 0.82π in the class-E inverter [16]. Therefore, the feedback network C_3-C_4-L_3 provides an additional phase shift, compensating the phase shift between the output and the gate-drive voltages. Additionally, the class-E power oscillator features to achieve the ZVS at the nominal state, which contributes to high-efficiency operation.

However, when load variations occur, the class-E power oscillator is unable to maintain the ZVS, and both the output voltage and current fluctuate. The high sensitivity to load variations is attributable to the class-E inverter. The class-E inverter not only causes non-ZVS against load variations but also experiences changes in the phase shift of the output voltage [17]. Consequently, the phase-shift requirement for the oscillation cannot be satisfied, changing the frequency to forcibly induce the oscillation. Therefore, even minor load variations can seriously affect the overall performance of the power oscillator.

6.3 Load-Independent Class-E Power Oscillator

To address the sensitivity of the power oscillator to load variations, the robustness of the inverter should be ensured. Accordingly, this chapter focuses on the load-independent class-E inverter [4]. The load-independent class-E inverter achieves the ZVS regardless of the load resistance without changing the circuit topology from the original class-E inverter. Moreover, another critical aspect is to provide a fixed phase shift in the output voltage against load variations. We found these features are highly suitable for power oscillators. However, the load-independent class-E inverter has a π phase shift between the output and the gate-drive voltages,

which cannot be compensated using the feedback network in the conventional class-E power oscillator. Therefore, the topological change is necessary to incorporate the load-independent class-E inverter into the power oscillator.

Fig. 6.3 shows the circuit topology of the proposed load-independent class-E power oscillator. The proposed power oscillator is composed of input DC-voltage source V_I, switching device S, finite inductor L_1, shunt capacitor C_1, LCCL filter L_2-C_2-C_3-L_3, load resistance R_L, DC-blocking capacitor C_4, and voltage-divide resistances R_1 and R_2. The capacitor C_3 is divided into C_{31} and C_{32} to adjust the amplitude of the gate-drive voltage.

This chapter introduces an LCCL filter to provide an additional phase shift to the load-independent class-E inverter. Fig. 6.4 shows typical waveforms of the proposed power oscillator. The LCCL filter provides a $\pi/2$ phase shift between the currents i_2 and i_O under a specific resonant condition. Also, the phase shift of the voltage across the capacitor C_{32} leads $\pi/2$ against the output current i_O. Consequently, the voltage v_{32} becomes in phase with the gate-drive voltage, satisfying the phase-shift condition necessary for the oscillation. Most notably, these phase shifts are fixed and independent of the load resistance. Besides, the input impedance of the LCCL filter becomes purely resistive in this particular resonant condition, which does not interfere with the load-independent operation of the inverter. Therefore, the proposed power oscillator successfully incorporates the load-independent operation in the power oscillator.

The proposed power oscillator exhibits the load-independent characteristics in ZVS, output current, and gate-drive voltage. Although the load-independent class-E inverter exhibits constant voltage gain against load variations, the proposed power

oscillator has a constant current gain due to the additional LCCL filter. The constant current characteristic makes the amplitude of the voltage v_{32} also constant. As a result, the amplitude of the gate-drive voltage becomes independent of the load resistance, which further improves the stability of the oscillation.

6.4 Circuit Analysis

This section provides the circuit analysis for the load-independent class-E power oscillator. The analysis gives design conditions, waveform equations, and an optimal design point. To perform the analysis for the proposed power oscillator, we put the following assumptions for simplification.

(i) The resistances R_1 and R_2 are large enough so that these components are regarded not to conduct current. Also, they divide the input voltage to produce a bias voltage, which is equal to the threshold voltage of the switching device V_{th}. Namely,

$$V_{th} = \frac{R_1}{R_1 + R_2} V_I. \tag{6.1}$$

(ii) The capacitor C_4 works as a DC blocking and is large enough to be regarded as a DC-voltage source V_{th}.

(iii) The LCCL filter only passes fundamental frequency current, and the output current can be expressed as purely sinusoid as

$$i_O(\theta) = I_O \cos\theta, \tag{6.2}$$

where I_O is the amplitude of the output current.

(iv) The inductor L_2 is divided into an extra-inductive component L_X and a resonant component L_R.

(v) The switching device functions as an ideal switch, turning OFF when $V_{th} > v_{gs}(\theta)$ and turning ON when $V_{th} \leq v_{gs}(\theta)$. Additionally, it possesses zero ON-resistance, zero gate resistance, and infinite OFF-resistance.

(vi) The drain-source and gate parasitic capacitances of the switching device are absorbed into C_1 and C_{32}, respectively.

(vii) All the passive components operate linearly without parasitic components.

From the assumptions above, the equivalent circuit model of the proposed power oscillator is derived as shown in Fig. 6.5.

6.4.1 LCCL filter

From the assumption (iii), the voltage across capacitor C_{32} can be expressed as

$$v_{32}(\theta) = -\frac{I_O}{\omega C_{32}} \sin\theta, \tag{6.3}$$

Accordingly, the gate-drive voltage v_{gs} can be obtained as

$$v_{gs}(\theta) = -\frac{I_O}{\omega C_{32}} \sin\theta + V_{th}. \tag{6.4}$$

The input impedance of the LCCL filter is obtained as

$$Z_{eq} = \frac{R_L}{\omega^2 C_2^2 (R_L^2 + H_2^2)} + j\left[H_1 - \frac{H_2}{\omega^2 C_2^2 (R_L^2 + H_2^2)}\right], \tag{6.5}$$

where H_1 and H_2 are defined as

$$H_1 = \omega L_R - \frac{1}{\omega C_2}, \tag{6.6}$$

and

$$H_2 = \omega L_3 - \frac{1}{\omega C_2} - \frac{1}{\omega C_3}, \tag{6.7}$$

respectively.

For ensuring the load-independent operation, the input impedance of the LCCL filter is designed to be purely resistive. Namely, the resonant conditions should be $H_1 = H_2 = 0$, which determines the angular oscillation frequency ω_S as

$$\omega_S = 2\pi f_S = \frac{1}{\sqrt{L_R C_2}} = \sqrt{\frac{1}{L_3}\left(\frac{1}{C_2} + \frac{1}{C_3}\right)}. \tag{6.8}$$

When (6.8) is satisfied, the input impedance in (6.5) becomes

$$Z_{eq} = R_{eq} = \frac{1}{\omega_S^2 C_2^2 R_L}. \tag{6.9}$$

We can see from (6.6)-(6.8) that the resonant conditions hold regardless of the load resistance R_L. Therefore, (6.9) indicates that the variations of load resistance can be seen as resistive variations for the class-E inverter.

The voltage gain G_f and phase shift φ_f between v_{eq} and v_O can be obtained as

$$G_f = \frac{V_O}{V_{eq}} = \sqrt{\frac{\omega^2 C_2^2 R_L (R_L^2 + H_2^2)}{\sqrt{R_L^2 + [\omega^2 C_2^2 (R_L^2 + H_2^2) H_1 - H_2]^2}}}, \tag{6.10}$$

and

$$\varphi_f = \begin{cases} \arctan\left(\frac{1}{\omega^2 C_1^2 R_L H_1} - \frac{H_2}{R_L}\right) & \text{for} \quad H_1 < 0, \\ -\pi + \arctan\left(\frac{1}{\omega^2 C_1^2 R_L H_1} - \frac{H_2}{R_L}\right) & \text{for} \quad H_1 \geq 0, \end{cases} \tag{6.11}$$

respectively, where V_{eq} and V_O are the amplitudes of the input and output voltages of the LCCL filter. From (6.10) and (6.11), the voltage gain and phase shift under

the resonant condition in (6.8) are derived as

$$G_f = \omega_S C_2 R_L = \frac{R_L}{\omega_S L_R}, \tag{6.12}$$

and

$$\varphi_f = -\frac{\pi}{2}, \tag{6.13}$$

respectively.

6.4.2 Equivalent Class-E Inverter

The voltage across the equivalent resistance R_{eq} is derived from (6.2), (6.12), and (6.13) as

$$v_{eq}(\theta) = V_{eq} \sin\theta = \omega_S L_R I_O \sin\theta. \tag{6.14}$$

Additionally, from (6.4) and the assumption (v), the switch turns OFF during $0 \leq \theta < \pi$ and turns ON during $\pi \leq \theta < 2\pi$.

6.4.2.1 Waveform Equations

During the turn-OFF state, the differential equation for the switch voltage v_S is obtained from Kirchhoff's Voltage Law (KVL) as

$$\frac{d^2 v_S(\theta)}{d\theta^2} + \omega_1^2 v_S(\theta) = \omega_1^2 \left(V_I - \frac{\omega_S L_1 V_{eq} \cos\theta}{R_{eq}} \right), \tag{6.15}$$

where the normalized resonant frequency ω_1 is defined as

$$\omega_1 = \frac{1}{\omega_S \sqrt{L_1 C_1}}. \tag{6.16}$$

The solution to (6.15) yields the expression for the switch voltage in the turn-OFF period as

$$v_S(\theta) = \alpha \cos(\omega_1 \theta) + \beta \sin(\omega_1 \theta) + V_I - \frac{\omega_S L_1 \omega_1^2 V_{eq} \cos\theta}{R_{eq}(\omega_1^2 - 1)}, \tag{6.17}$$

where α and β are constants.

From KVL, we obtain

$$\frac{di_1(\theta)}{d\theta} = \frac{1}{\omega_S L_1}\left[V_I - v_S(\theta)\right]. \tag{6.18}$$

By substituting (6.17) into (6.18) and solving the differential equation, we obtain the expression of current i_1 during turn-OFF period as

$$i_1(\theta) = -\frac{\omega_1[\alpha \sin(\omega_1\theta) - \beta \cos(\omega_1\theta)]}{\omega_S L_1} + \frac{\omega_1^2 V_{eq} \sin\theta}{R_{eq}(\omega_1^2 - 1)} \tag{6.19}$$

During the turn-ON state, the switch is shorted out, making the switch voltage to be zero as

$$v_S(\theta) = 0. \tag{6.20}$$

From KVL, we obtain

$$\frac{di_1(\theta)}{d\theta} = \frac{V_I}{\omega_S L_1}. \tag{6.21}$$

By solving (6.21), we obtain

$$i_1(\theta) = \frac{V_I}{\omega_S L_1}\theta + \gamma, \tag{6.22}$$

where γ is a constant.

6.4.2.2 Boundary Condition

By considering the continuity of the current i_1, the boundary condition can be formulated as

$$i_1(\pi^-) = i_1(\pi^+). \tag{6.23}$$

From (6.19), (6.22), and (6.23), the unknown constant γ can be obtained, and the expression of i_1 during turn-ON period becomes

$$i_1(\theta) = \frac{V_I(\theta-\pi) - \omega_1[\alpha\sin(\pi\omega_1) - \beta\cos(\pi\omega_1)]}{\omega_S L_1}, \tag{6.24}$$

The unknown constants α and β can also be obtained from the boundary conditions of

$$i_1(0) = i_1(2\pi), \tag{6.25}$$

and

$$\left.\frac{di_1(\theta)}{d\theta}\right|_{\theta=0} = \left.\frac{di_1(\theta)}{d\theta}\right|_{\theta=2\pi}. \tag{6.26}$$

From (6.19) and (6.24)-(6.26), we obtain

$$\alpha = \frac{1}{\omega_S C_1}\left[\frac{V_{eq}}{R_{eq}(\omega_1^2-1)} - \frac{V_I}{\omega_S L_1 \omega_1^2}\right], \tag{6.27}$$

and

$$\beta = \frac{\pi\omega_1 V_I - \left[\frac{\omega_1^2\omega_S L_1 V_{eq}}{R_{eq}(\omega_1^2-1)} - V_I\right]\sin(\pi\omega_1)}{1-\cos(\pi\omega_1)}, \tag{6.28}$$

6.4.2.3 Design Condition

As the band-pass filter only passes the fundamental frequency component, the amplitude of the voltage across the equivalent resistance R_{eq} and the extra inductance L_X can be obtained from the first harmonic term of the Fourier Series Expansion as

$$V_{eq} = \frac{1}{\pi}\int_0^{2\pi} v_S(\theta)\sin\theta d\theta, \tag{6.29}$$

and

$$\frac{\omega_S L_X V_{eq}}{R_{eq}} = \frac{1}{\pi}\int_0^{2\pi} v_S(\theta)\cos\theta d\theta, \tag{6.30}$$

respectively.

We impose the switch voltage to achieve the turn-ON ZVS, which can be formulated as

$$v_S(\pi) = 0. \tag{6.31}$$

From (6.17), (6.27), (6.28), and (6.31), the design condition can be obtained as

$$\tan\left(\frac{\pi\omega_1}{2}\right) + \frac{\pi\omega_1}{2} = 0, \tag{6.32}$$

which can be numerically solved as

$$\omega_1 \approx 1.292. \tag{6.33}$$

From (6.17), (6.20), and (6.27)-(6.29), the amplitude of the voltage across the equivalent resistance R_{eq} becomes

$$V_{eq} = \frac{\omega_1^3 V_I}{(1-\omega_1^2)\tan\left(\frac{\pi\omega_1}{2}\right)} \approx 1.590 V_I. \tag{6.34}$$

We can see from (6.34) that the amplitude of the voltage v_{eq} is independent of the load resistance. Accordingly, from (6.14), the amplitude of the output current can be derived as

$$I_O = \frac{\omega_1^3 V_I}{\omega_S L_1 (1-\omega_1^2) \tan\left(\frac{\pi\omega_1}{2}\right)} \approx \frac{1.590 V_I}{\omega_S L_1}. \tag{6.35}$$

which is also unaffected by the load resistance.

From (6.17), (6.20), (6.27), (6.28), and (6.30), the ratio of L_X and L_1 is determined uniquely as

$$\frac{L_X}{L_1} = -\frac{2\omega_1^3}{\pi(\omega_1^2-1)^2 \tan\left(\frac{\pi\omega_1}{2}\right)} - \frac{\omega_1}{2(\omega_1^2-1)} \approx 0.2662. \tag{6.36}$$

From the circuit analysis, it can be concluded that the design condition for the load-independent class-E power oscillator is to satisfy (6.8), (6.33), and (6.36). Also, the fact that the proposed power oscillator achieves the ZVS regardless of the load resistance can be verified using (6.17), (6.27), and (6.28) as

$$\begin{aligned} \frac{\partial v_S(\pi)}{\partial R_L} &= \frac{\partial v_S(\pi)}{\partial R_{eq}} \cdot \frac{\partial R_{eq}}{\partial R_L} \\ &= \frac{\partial}{\partial R_{eq}} \left\{ \left[2 + \frac{\pi\omega_1 \sin(\pi\omega_1)}{1-\cos(\pi\omega_1)} \right] V_I \right\} \cdot \frac{\partial R_{eq}}{\partial R_L} \\ &= 0. \end{aligned} \tag{6.37}$$

6.4.2.4 Circuit Characteristics

It is stated from (6.36) that the proposed power oscillator can be designed with arbitrary input inductance L_1. Therefore, a reasonable value of the inductance should be explored. Fig. 6.6 shows the circuit characteristics as functions of normalized inductance $\omega_S L_1/R_{Ld}$, where R_{Ld} is the value of load resistance at the design point.

The power-output capability is calculated as

$$c_p = \frac{P_O}{V_{Smax} I_{Smax}} = \frac{V_{eq}^2}{2 R_{eq} V_{Smax} I_{Smax}}, \tag{6.38}$$

where P_O is the output power, and V_{Smax} and I_{Smax} are peak values of the switch voltage and current, respectively. It can be seen from Fig. 6.6(a) that the maximum switch voltage monotonically decreases as the increase of L_1. Meanwhile, the maximum switch current monotonically decreases as the increase of L_1. Thus, we can find from (6.34) and (6.38) that certain L_1 maximizes the power-output capability. We can see from Fig. 6.6(b) that the power-output capability is maximized to $c_p = 1.02$ at $\omega_S L_1 / R_{Ld} = 1.05$.

6.5 Experimental Verification

The experimental verifications for the proposed power oscillator were performed under the specifications given in Table 6.1. We also conducted the experiment for the conventional class-E power oscillator under the same conditions. Based on the specifications, we selected GS61004B e-GaN HEMT from Infineon Technologies for the switching device S. From the datasheet, the maximum gate-to-source voltage and the threshold voltage were obtained as $V_{Sm} = 7$ V and $V_{th} = 1.7$ V, respectively. Thus, the amplitude of the gate-drive voltage was designed to be $V_{gs} = 4$ V.

6.5.1 Circuit Design for Proposed Power Oscillator

The proposed power oscillator is designed based on the specifications. From the circuit analysis given in Section 6.4, closed-form design equations can be derived,

which determine all the component values uniquely. For designing the power oscillator to achieve the maximum power-output capability, the L_1 should be determined as

$$L_1 = \frac{0.167R_{Ld}}{f_S} \approx 639 \text{ nH}. \tag{6.39}$$

From (6.33) and (6.39), the shunt capacitance C_1 is obtained as

$$C_1 = \frac{0.0909}{f_S R_{Ld}} \approx 517 \text{ pF}. \tag{6.40}$$

From the specifications, we obtain

$$L_2 = \frac{Q_2 R_{Ld}}{f_S} \approx 1015 \text{ nH}, \tag{6.41}$$

and

$$L_3 = \frac{Q_3 R_{Ld}}{f_S} \approx 2347 \text{ nH}. \tag{6.42}$$

From (6.36) and (6.39), the extra inductance L_X is determined as

$$L_X = \frac{0.0445R_{Ld}}{f_S} \approx 170 \text{ nH}. \tag{6.43}$$

From (6.6) and (6.8), the capacitance C_2 becomes

$$C_2 = \frac{0.0253}{f_S^2(L_2 - L_X)} \approx 652 \text{ pF}. \tag{6.44}$$

From (6.7) and (6.8), the capacitance C_3 is

$$C_3 = \frac{0.0253}{f_S^2(L_3 - L_2 + L_X)} \approx 367 \text{ pF}. \tag{6.45}$$

From (6.2), (6.14), and (6.34), we obtain

$$C_{32} = \frac{0.0403V_I}{f_S^2 L_2 V_{gs}} \approx 6478 \text{ pF}. \tag{6.46}$$

As the capacitances C_{31} and C_{32} are connected in series, the capacitance C_{31} is obtained from (6.45) and (6.46) as

$$C_{31} = \frac{C_{32}C_3}{C_{32} - C_3} \approx 389 \text{ pF}. \tag{6.47}$$

Fig. 6.8 shows the bode plot of the LCCL filter obtained using (6.10) and (6.11), where the rated load resistance is specified as $R_{Lr} = 25\ \Omega$. It can be seen that the filter can eliminate the harmonic frequencies, such as 13.56 MHz and 20.34 MHz, which is compatible with the assumption (iii) in the analysis. Additionally, the phase shift becomes $-\pi/2$, which is constant for different normalized load resistances at 6.78 MHz.

To implement the inductors, we used Mix 2 Iron-Powder Core from Micrometals. Fig. 6.9 shows the implemented load-independent class-E power oscillator. As seen from Fig. 6.9, the power oscillator requires only the main DC-supply voltage to perform DC to AC conversion, simplifying the implementation.

6.5.2 Experimental Results for Class-E Power Oscillator

Fig. 6.10 shows the experimental waveforms of the conventional class-E power oscillator, where the waveforms were measured by the MSO58 Mixed Signal Oscilloscope from Tektronix. We can see from Fig. 6.10 that the gate-drive voltage v_{gs} did not shape pure sinusoid, causing a voltage depression at the turn-OFF period. A similar observation has also been reported in [**?**] and is believed to be caused by the nonlinearity of the gate parasitic capacitance. As widely recognized, the allowable gate-voltage range of GaN e-HEMT is extremely narrow. Therefore, this operation could potentially damage the device. We can also observe that the switch voltage

achieved the ZVS for $R_L/R_{Lr} = 1$, as shown in Fig. 6.10(a). Although we tried to experiment with the operation for the case of $R_L/R_{Lr} < 1$ a number of times, the waveforms could not be measured even at $R_L/R_{Lr} = 0.9$ due to the instantaneous damage to the switching device. This is because a sudden reverse conduction occurred in the GaN e-HEMT at the turn-OFF period, which harmed the device. Therefore, we measured the operation for $R_L/R_{Lr} = 2$, as shown in Fig. 6.10(b). However, the switch voltage could not achieve the ZVS. Besides, the amplitude of the output current changed depending on the load resistance.

The experimental results show that the conventional class-E power oscillator cannot tolerate even small load variations, which significantly degrades the overall performance.

6.5.3 Experimental Results for Proposed Power Oscillator

Fig. 6.11 shows the superimposed experimental and analytical waveforms of the load-independent class-E power oscillator. We can see from Fig. 6.11 that the gate-drive voltage was purely sinusoid without the voltage depression compared with the conventional class-E power oscillator in Fig. 6.10. This is because the nonlinear gate capacitance was absorbed into the external capacitance C_{32}, mitigating the effect of the nonlinearity. We can also see that the ZVS was achieved regardless of the load resistance. Additionally, the output current maintained constant amplitude and phase shift. Moreover, the load-independent operation contributes to generating gate-drive voltage with constant amplitude and phase shift against load variations. Therefore, the proposed power oscillator maintained a stable oscillation against load

variations. The experimental and analytical waveforms were in good agreement, which demonstrated the validity of the experiment.

6.5.4 Circuit Characteristics

Fig. 6.12 illustrates the output-current amplitude and efficiency as functions of load resistance for conventional and proposed power oscillator, where I_{mr} is the output-current amplitude in the rated condition. The power-conversion efficiency including the gate-drive losses was calculated as

$$\eta = \frac{P_O}{P_I} = \frac{R_L I_O^2}{2 V_I I_I}, \tag{6.48}$$

where P_I and I_I are the input power and current, respectively.

It can be seen from Fig. 6.12 that the proposed power oscillator maintained a constant output-current amplitude against load variations. Additionally, the high power-conversion efficiency above 80 % was maintained within $0.4 \leq R_L/R_{Lr} \leq 2$ due to the load-independent ZVS operation. The peak power-conversion efficeincy was 87.4 % at $R_L/R_{Lr} = 1.6$.

The conventional power oscillator could not oscillate within $R_L/R_{Lr} < 1$ due to the instantaneous damage of the switching device. Therefore, the circuit performance for $1 \leq R_L/R_{Lr} \leq 2$ was evaluated. The output current fluctuated compared with the proposed power oscillator. Besides, the power-conversion efficiency was up to 82.8 % and decreased with the increase of load resistance.

From these results, we validated the load-independent operation of the proposed power oscillator, demonstrating its effectiveness.

6.6 Conclusion

This chapter has proposed the load-independent class-E power oscillator. The proposed power oscillator inherently achieves the ZVS regardless of the load resistance. Additionally, the amplitude and phase shift of both gate-drive voltage and output current are also independent of the load. These features enable the circuit to oscillate with high stability and efficiency over a wide range of load variations. The experimental results demonstrated the effectiveness of the proposed power oscillator.

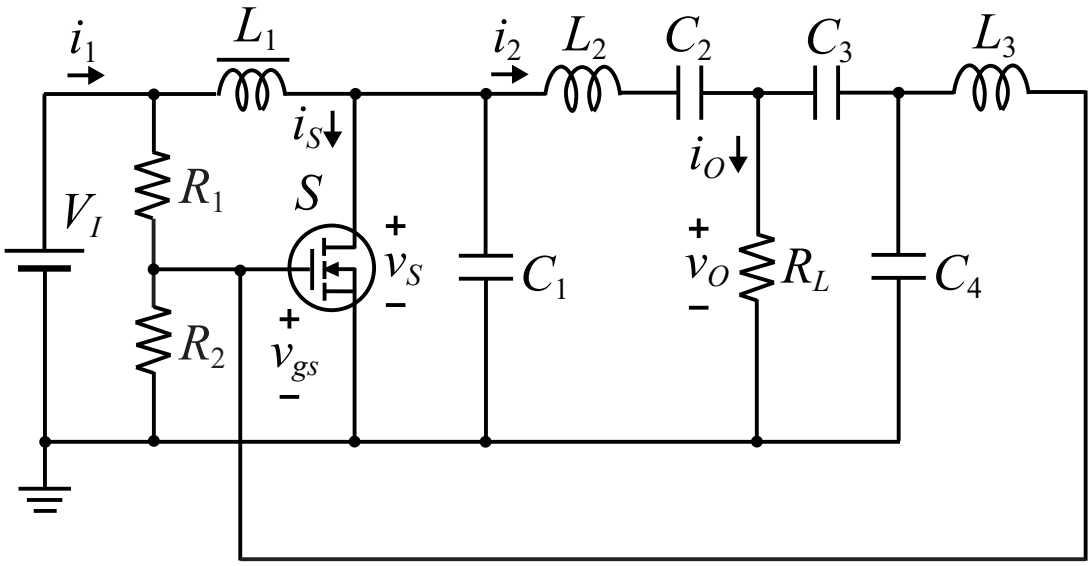

Fig. 6.1: Circuit topology of the conventional class-E power oscillator.

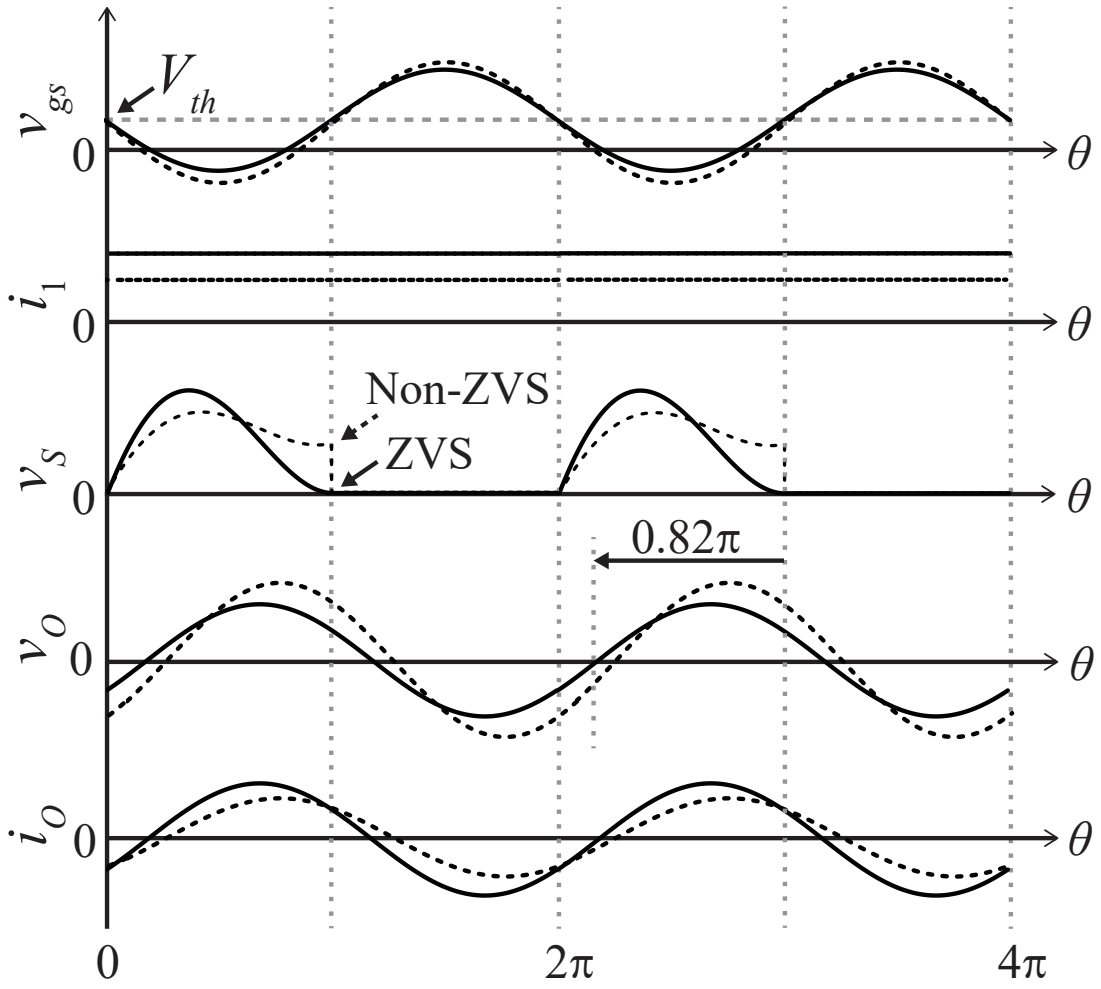

Fig. 6.2: Example waveforms of the conventional class-E power oscillator. (solid line: for the nominal state, dashed line: for load variations.)

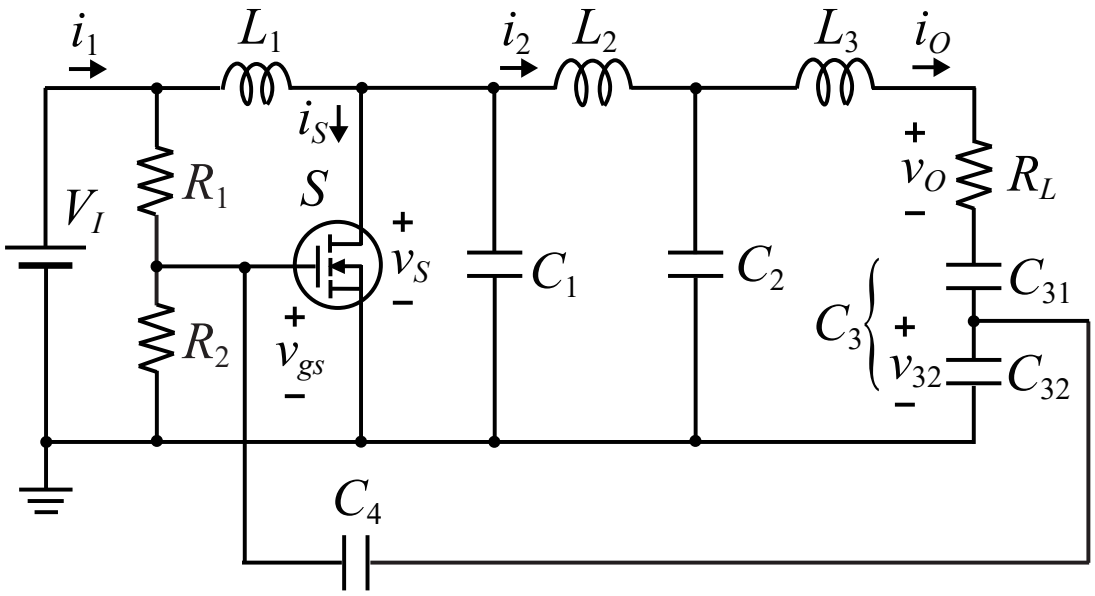

Fig. 6.3: Circuit topology of the load-independent class-E power oscillator.

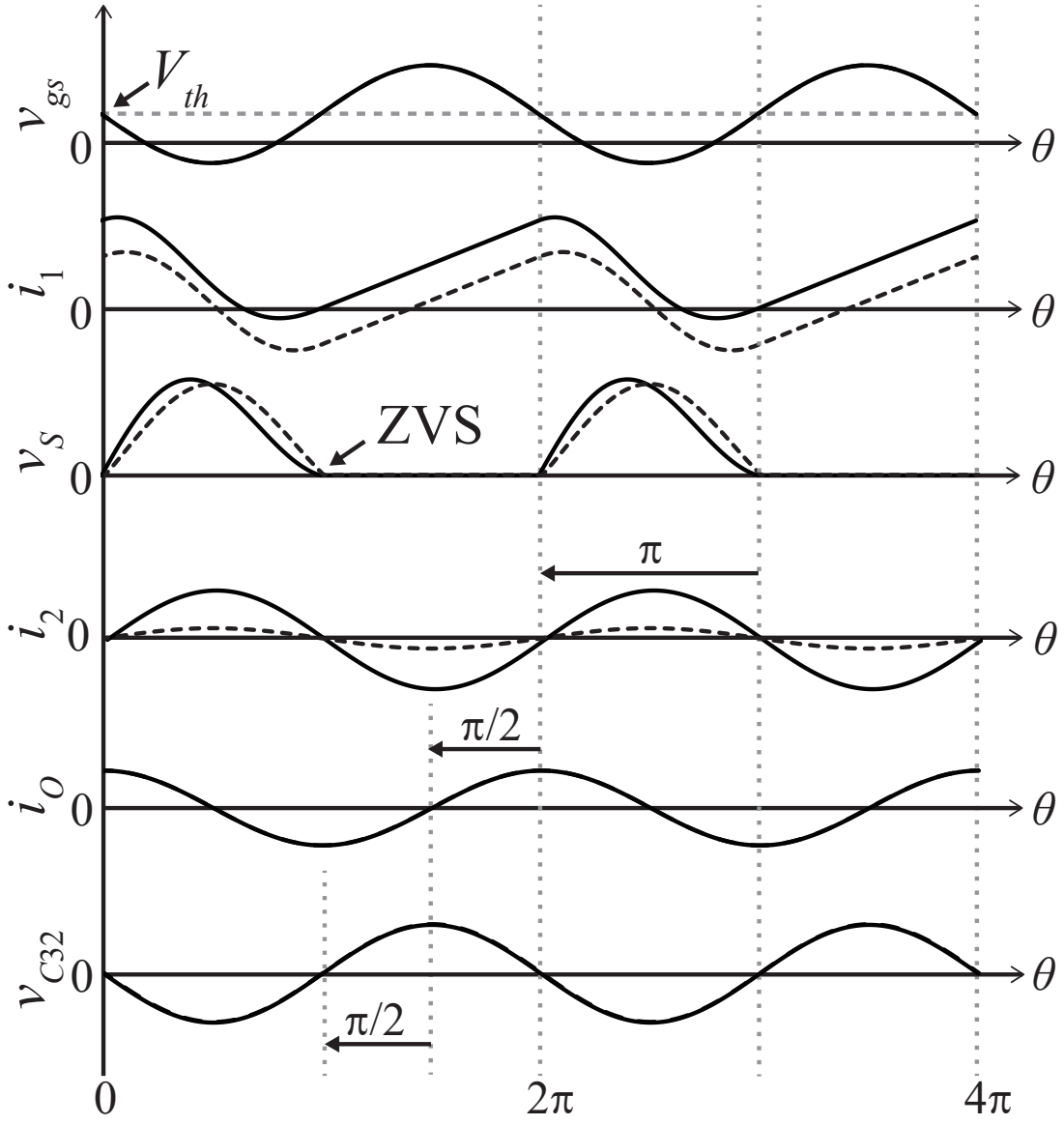

Fig. 6.4: Typical waveforms of the load-independent class-E power oscillator. (solid line: $R_L/R_{Lr} = 1$, dashed line: $R_L/R_{Lr} = 0.1$.)

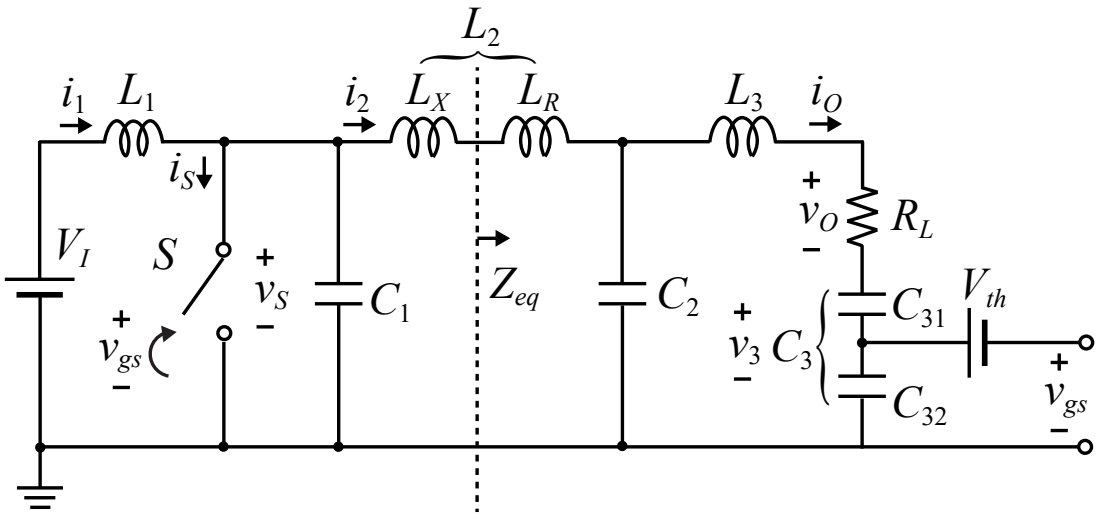

Fig. 6.5: Analytical circuit model of the proposed power oscillator. (a) Overall circuit. (b) Equivalent inverter model.

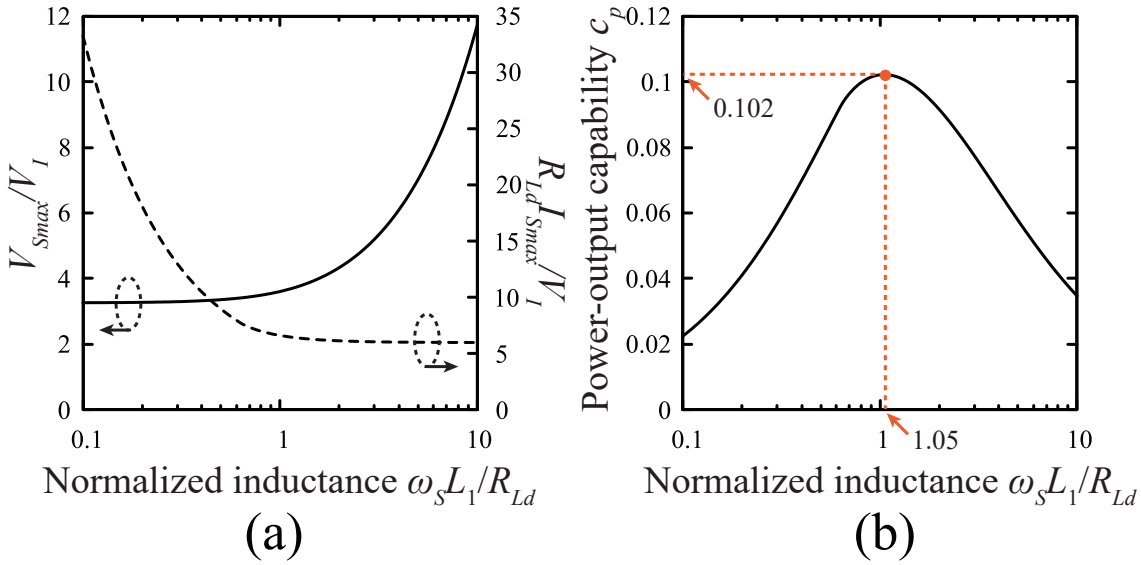

Fig. 6.6: Circuit characteristics as functions of normalized inductance $\omega L_1/R_{Lr}$. (a) Normalized maximum switch voltage and current. (b) Power-output capability c_p.

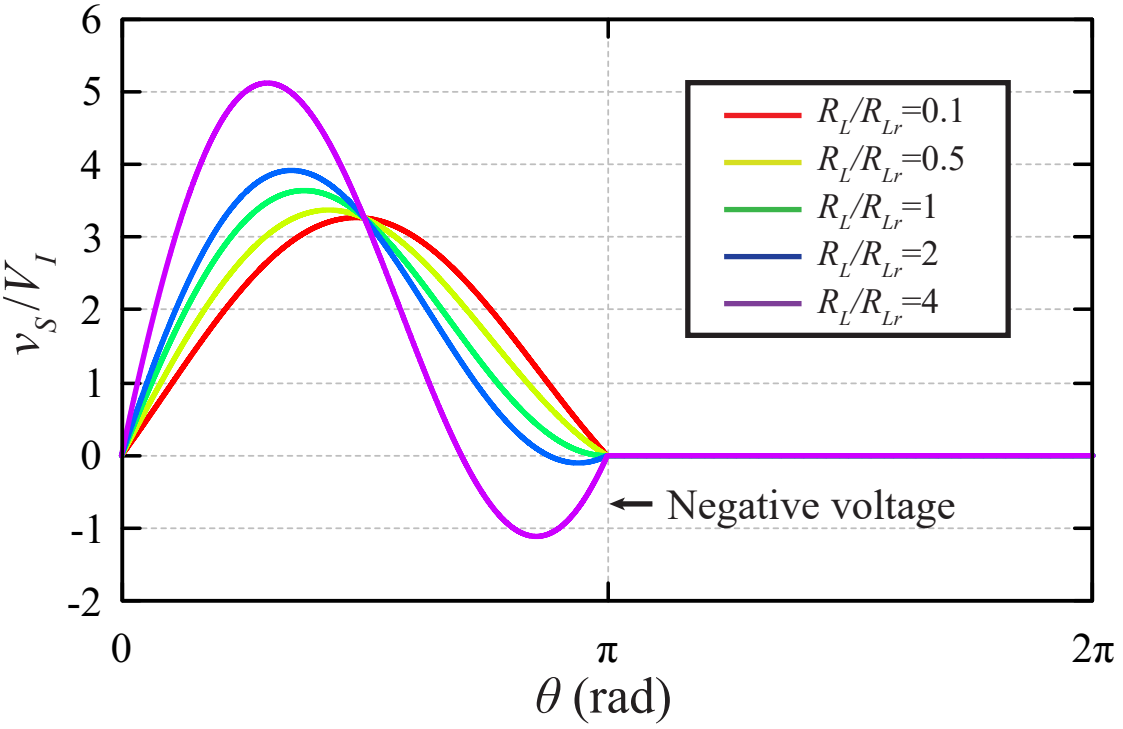

Fig. 6.7: Waveforms of the normalized switch voltage for fixed load resistances.

Table 6.1: The specifications for the experimental verifications.

Parameter	Specification
Input DC-voltage V_I	25 V
Oscillation frequency f_S	6.78 MHz
Load resistance at design point R_{Ld}	50 Ω
Normalized inductance $\omega_S L_2/R_{Ld}$	0.72
Normalized inductance $\omega_S L_3/R_{Ld}$	5

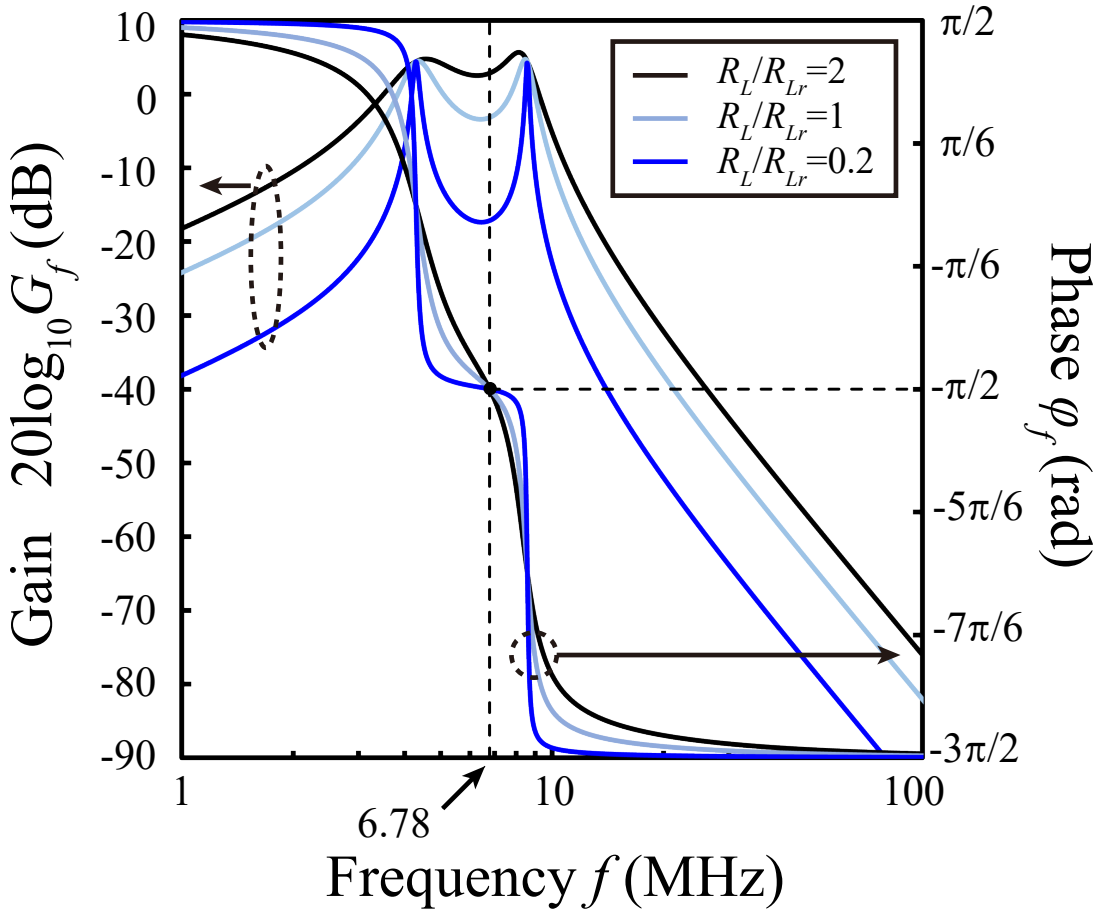

Fig. 6.8: Gain $\log_{10}|I_O/V_{eq}|$ and phase of the LCCL filter as functions of the frequency.

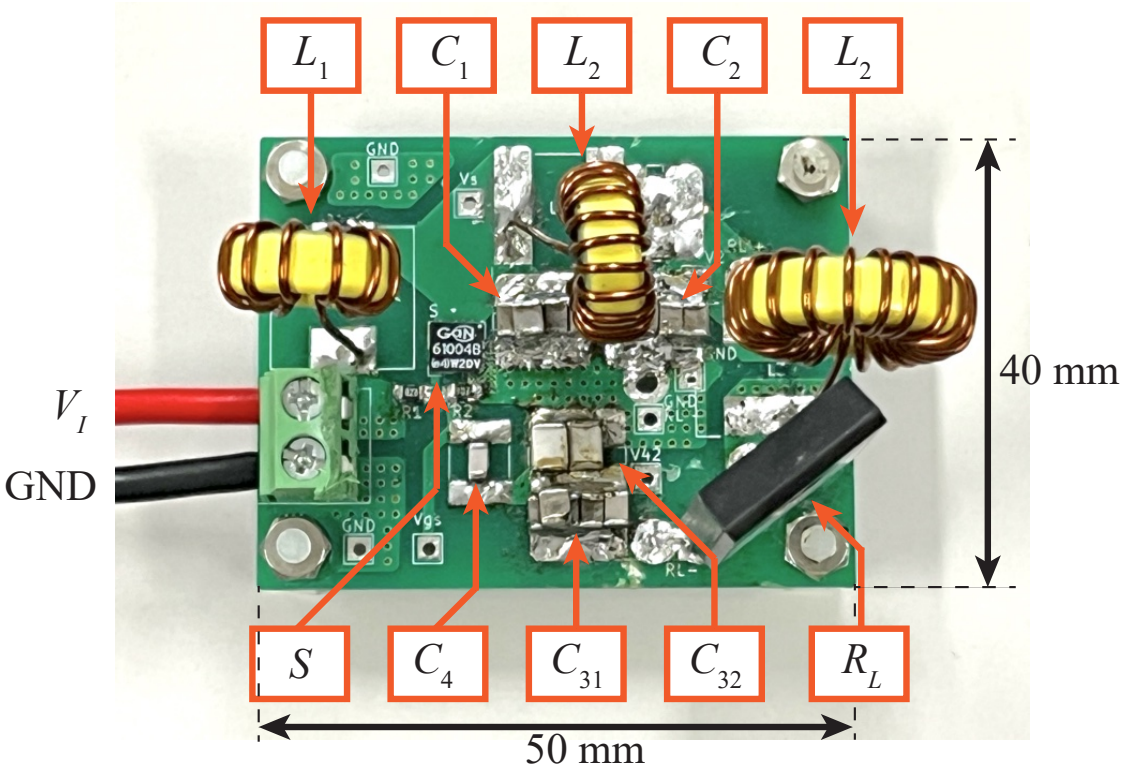

Fig. 6.9: Photo of the implemented load-independent class-E power oscillator.

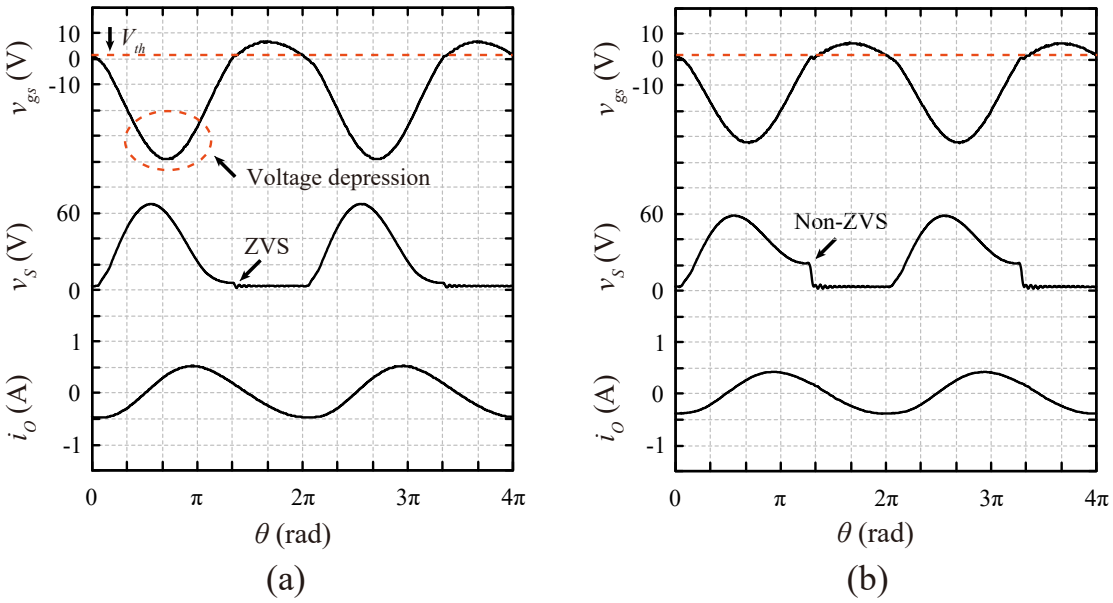

Fig. 6.10: Experimental waveforms of the conventional class-E power oscillator for fixed load resistance. (black: $R_L/R_{Lr} = 1$, blue: $R_L/R_{Lr} = 1.2$.)

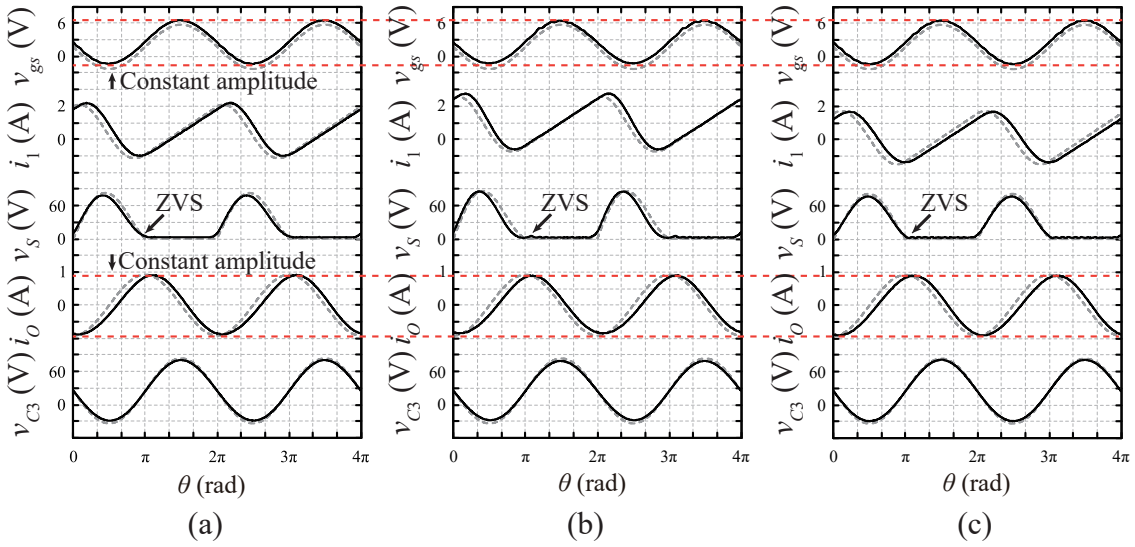

Fig. 6.11: Superimposed experimental and analytical waveforms of the load-independent class-E power oscillator for fixed load resistance. (solid line: experiment, dashed line: analytical.) (a) $R_L/R_{Lr} = 1$. (a) $R_L/R_{Lr} = 0.5$. (c) $R_L/R_{Lr} = 0.1$.

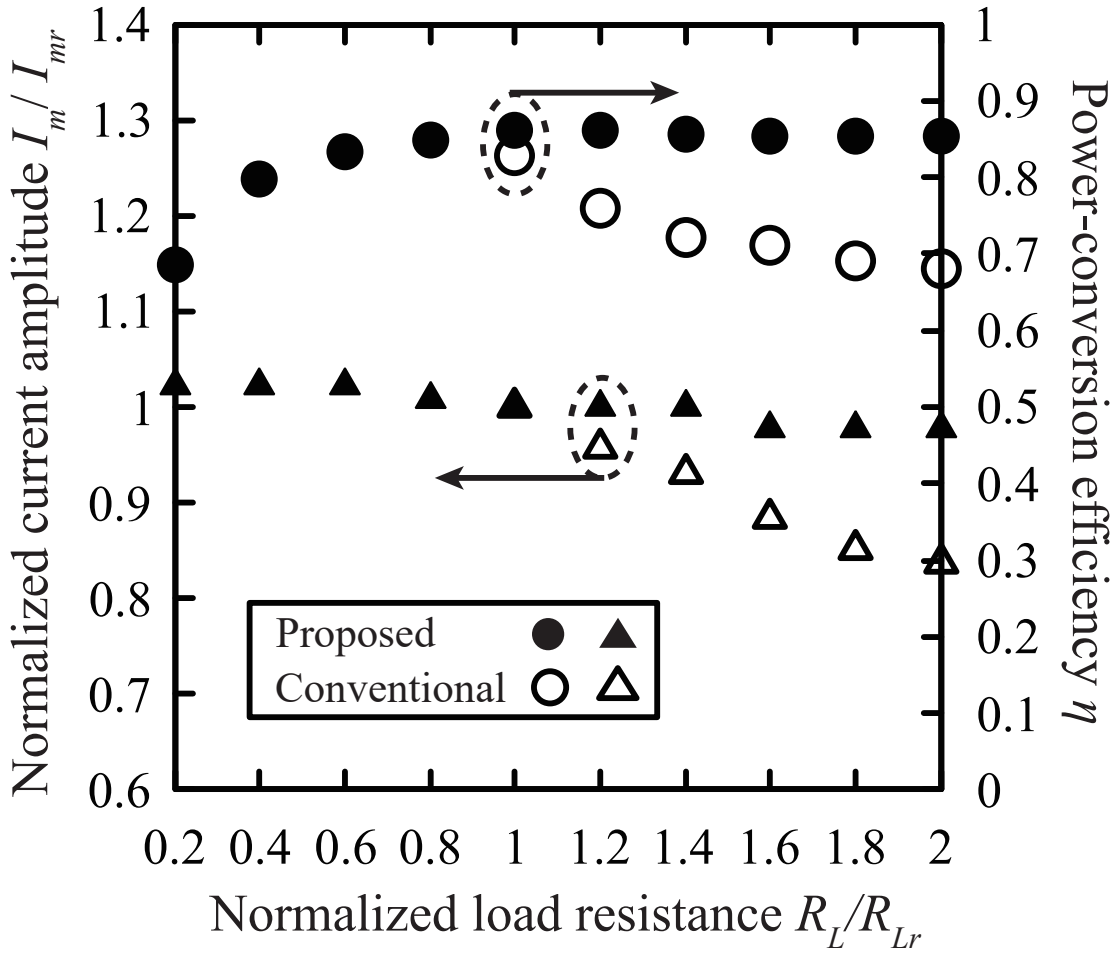

Fig. 6.12: Output-current amplitude I_m and power-conversion efficiency η as functinos of load resistance R_L.

References

[1] X. Long, Z. Jun, B. Zhang, D. Chen, and W. Liang, "A unified electrothermal behavior modeling method for both SiC MOSFET and GaN HEMT," IEEE Trans. Ind. Electron., vol. 68, no. 10, pp. 9366-9375, 2021.

[2] A. Ghahremani, A.-J. Annema, and B. Nauta, "Load mismatch sensitivity of class-E power amplifiers," IEEE Trans. Microw. Theory Tech., vol. 67, no. 1, pp. 216-230, 2019.

[3] Z.Sun, Y.Wang, J.Sun, Y.Guan, and D.Xu, "Design of a strong robust wireless power transfer system with wide-range output regulation based on dual-band architecture," IEEE Trans. Ind. Electron., vol. 70, no. 11, pp. 11142-11152, 2023.

[4] R. Zulinski and K. Grady, "Load-independent class E power inverters. I. theoretical development," IEEE Trans. Circuits Syst., vol. 37, no. 8, pp. 1010-1018, 1990.

[5] S. Aldhaher, D. C. Yates, and P. D. Mitcheson, "Load-independent Class E/EF inverters and rectifiers for MHz-switching applications," IEEE Trans. Power Electron., vol. 33, no. 10, pp. 8270-8287, 2018.

[6] H. Sekiya, K. Tokano, W. Zhu, Y. Komiyama, and K. Nguyen, "Design procedure of load-independent class-E WPT systems and its application in robot arm," IEEE Trans. Ind. Electron., vol. 70, no. 10, pp. 10014-10023, 2023.

[7] J. M. Arteaga, S. Aldhaher, G. Kkelis, C. Kwan, D. C. Yates, and P. D. Mitcheson, "Dynamic capabilities of multi-MHz inductive power transfer sys-

tems demonstrated with batteryless drones," IEEE Trans. Power Electron., vol. 34, no. 6, pp. 5093-5104, 2019.

[8] W. Zhu, Y. Komiyama, A. Komanaka, K. Nguyen, and H. Sekiya, "Analysis of load-independent ZCS parallel-resonant inverter with constant current," IEEE Trans. Ind. Electron., vol. 71, no. 9, pp. 10433-10443, 2024.

[9] J. Ebert and M. Kazimierczuk, "Class E high-efficiency tuned power oscillator," IEEE J. Solid-State Circuits, vol. 16, no. 2, pp. 62-66, 1981.

[10] M. Kazimierczuk, V. Krizhanovski, J. Rassokhina, and D. Chernov, "Class-E MOSFET tuned power oscillator design procedure," IEEE Trans. Circuits Syst. I: Reg. Papers, vol. 52, no. 6, pp. 1138-1147, 2005.

[11] M. Ahmadi and M. Salehi, "A self-tuned class-E power oscillator," IEEE Trans. Power Electron., vol. 34, no. 5, pp. 4434-4449, 2019.

[12] M. Ahmadi and S. Pezeshkpour,"A self-starting class-E power oscillator with an inverting gate driver," IEEE Trans. Ind. Electron., vol. 67, no. 10, pp. 8344-8354, 2020.

[13] D. Kim, J. Chae, K.-B. Park, and G.-W. Moon, "A self-oscillated feedback network for push-pull resonant power converters," IEEE Trans. Power Electron., vol. 38, no. 11, pp. 14 249-14 261, 2023.

[14] T. Inaba and H. Koizumi, "Class E/F3 tuned power oscillator," IEEE Trans. Power Electron., vol. 33, no. 2, pp. 1420-1427, 2018.

[15] S. Pezeshkpour and M. M. Ahmadi, "A self-tuned class-E/F3 power oscillator," IEEE Trans. Power Electron., vol. 39, no. 9, pp. 11398-11408, 2024.

[16] N. Sokal and A. Sokal, "Class E-A new class of high-efficiency tuned single-ended switching power amplifiers," IEEE J. Solid-State Circuits, vol. 10, no. 3, pp. 168-176, 1975.

[17] T. Nagashima, X. Wei, T. Suetsugu, M. K. Kazimierczuk, and H. Sekiya, "Waveform equations, output power, and power conversion efficiency for class-E inverter outside nominal operation," IEEE Trans. Ind. Electron., vol. 61, no. 4, pp. 1799-1810, 2014.

Chapter 7

Load-Independent Class-E Synchronous Rectifier

7.1 Introduction

The evolution in wide-bandgap power semiconductor devices has accelerated the development of power electronics circuits operating in the MHz regime. The high-frequency operation reduces the energy-storage requirements for the passive components, allowing the downsizing of the overall circuit. However, high-frequency operation increases the switching losses, making it essential to achieve ZVS. Furthermore, it is also crucial to address load variations in practical applications. Namely, the high-frequency circuits that satisfy the ZVS and the output regulation against load variations are in high demand.

The load-independent class-E rectifier [1–5] achieves the ZVS and constant output voltage against load variations without any specific control. The load-independent class-E rectifier exhibits a time-reversed dual operation with the load-independent class-E inverter [5–7]. Hence, in order to attain the load-independent operation in the rectifier, synchronous rectification with forced turn-off is required. However,

conventional load-independent class-E synchronous rectifiers [1–5] require accurate phase detection, which is challenging in the MHz operation. Besides, the additional digital devices cause propagation delay, complicating the circuit design. Therefore, this chapter aims to fundamentally address the challenges in high-frequency synchronous rectification by realizing synchronous rectification using only passive components.

This chapter proposes the load-independent class-E synchronous rectifier with a passive feedforward network. The proposed rectifier generates the synchronized drive voltage using the voltage across the resonant capacitor. Therefore, additional phase-detection circuits and digital devices are not required for the synchronous rectification. Moreover, the proposed synchronous rectifier achieves the ZVS and constant output voltage against load variations. The validity and effectiveness of the proposed rectifier are confirmed by the experiment.

7.2 Proposed Rectifier

Fig. 1(a) shows the circuit topology of the proposed rectifier, which is composed of the LCCL filter $L_0 - C_0 - C_1 - L_1$, shunt capacitor C_2, switching device S, finite inductor L_2, voltage-divide resistances R_1 and R_2, filter capacitor C_f, DC-blocking capacitor C_3, and load resistance R_L. The capacitor C_0 is divided into C_{01} and C_{02} to adjust the amplitude of the gate-drive voltage.

Fig. 1(b) shows the example waveforms for fixed load resistance, where $\theta = 2\pi ft$ is the angular time and f is the operating frequency. Besides, R_{Lr} denotes the rated load resistance. The gate-drive voltage of the switching device is produced

using the voltage across the capacitor C_{02} for the phase information and the output voltage for the DC-bias voltage. The sinusoidal voltage across the capacitor C_{02} is delayed in phase by 90 degrees against the AC source. Also, the current i_1 leads the AC source by 90 degrees. Therefore, the phase shift between the voltage across the capacitor C_{02} and the current i_1 becomes just 180 degrees, which is consistent with the phase condition in the load-independent class-E rectifier [5]. Namely, the proposed rectifier realizes synchronous rectification using the phase information in the voltage across the capacitor C_{02}. The proposed rectifier realizes the synchronous rectification using only passive components, freeing it from accurate phase detection and consideration for the propagation delays caused by digital devices. Furthermore, the proposed rectifier achieves the ZVS and constant output voltage regardless of the load resistance when the current i_0 is independent of the load, as shown in Fig.1 (b).

7.3 Circuit Analysis

The input resistance and capacitance of the load-independent class-E rectifier with a 50 % duty ratio can be obtained by applying the analysis in [1] as

$$R_E = 1.263 R_L, \tag{7.1}$$

and

$$C_E = \frac{0.07155}{\omega}, \tag{7.2}$$

respectively. Hence, the proposed rectifier is transformed into the equivalent model, as shown in Fig. 2, where the feedforward network can be neglected to assume that

it has a high impedance at the operating frequency.

The input impedance of the proposed rectifier Z_{in} can be derived as

$$Z_{in} = \frac{R_E + j\{\omega C_1(\omega L_1 - \frac{1}{\omega C_E})[1 - \omega C_1(\omega L_1 - \frac{1}{\omega C_E})] - \omega C_1 R_E^2\}}{[1 - \omega C_1(\omega L_1 - \frac{1}{\omega C_E})]^2 + \omega^2 C_1^2 R_E^2} + j\left(\omega L_0 - \frac{1}{\omega C_0}\right). \tag{7.3}$$

The proposed rectifier is designed to have an input reactance which is independent of the load resistance. Therefore, the resonant conditions can be obtained as

$$\omega L_0 - \frac{1}{\omega C_0} - \frac{1}{\omega C_1} = 0, \tag{7.4}$$

and

$$\omega L_1 - \frac{1}{\omega C_1} = 0. \tag{7.5}$$

From (3) and (4), the input impedance of the proposed rectifier becomes

$$Z_{in} = \frac{1}{\omega C_1^2(R_E + \frac{1}{j\omega C_E})}. \tag{7.6}$$

From (5), the output voltage of the proposed rectifier V_O can be obtained as

$$V_O = \omega C_1 \sqrt{\frac{R_E R_L}{2}} |\dot{V}_{in}| = 0.7948 \omega C_1 R_L |\dot{V}_{in}|. \tag{7.7}$$

7.4 Experimental Verifications

Fig.3 shows the circuit configuration of the WPT system using the proposed rectifier for experimental verification. We employ the load-independent class-E inverter for the transmitter and the proposed rectifier for the receiver. By using the load-independent class-E inverter and the S-S coupling, the amplitude and the phase

shift of current i_0 can be independent of the load resistance [6]. The experimental specifications were given as $V_I = 30$ V, $f = 6.78$ MHz, and $R_L r = 100\Omega$. Table 1 gives the component values.

Fig. 4 shows the experimental waveforms of the proposed rectifier. We can see from Fig. 4(a) that the proposed rectifier was driven with the sinusoidal voltage, achieving synchronous rectification. We can also see from Fig. 4(a)-(c) that the voltage $v_S 2$ achieved the ZVS, and a constant output voltage was obtained against load variations.

Fig. 5 shows the output voltage and power-transfer efficiency as functions of the normalized load resistance. We can see that the consistent output voltage was obtained against a wide range of load variations. The maximum overall efficiency of 88.7 % was obtained at the rated condition.

7.5 Conclusion

This chapter has proposed the load-independent class-E synchronous rectifier with a passive feedforward network. The effectiveness of the proposed rectifier was confirmed by the experiment.

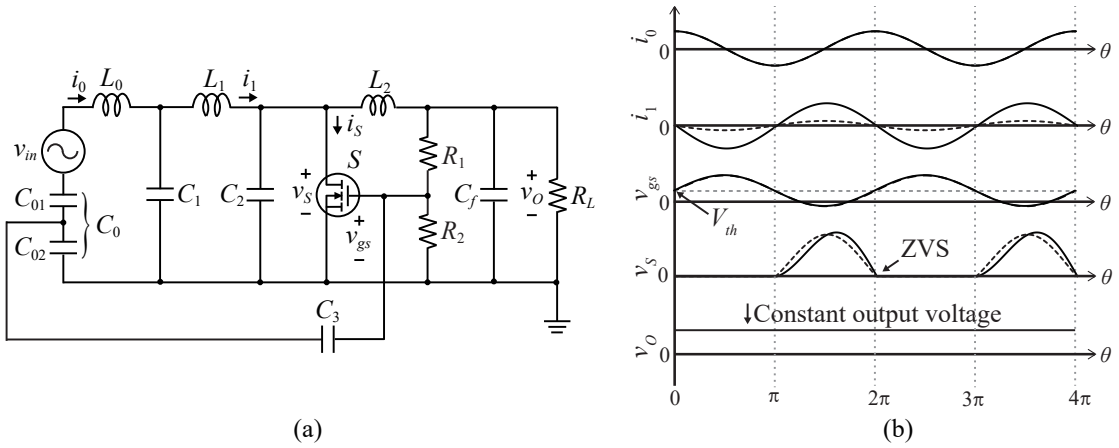

Fig. 7.1: Proposed rectifier. (a) Circuit topology. (b) Example waveforms for fixed load resistance (solid line: $R_L/R_{Lr} = 1$, dashed line: $R_L/R_{Lr} = 10$).

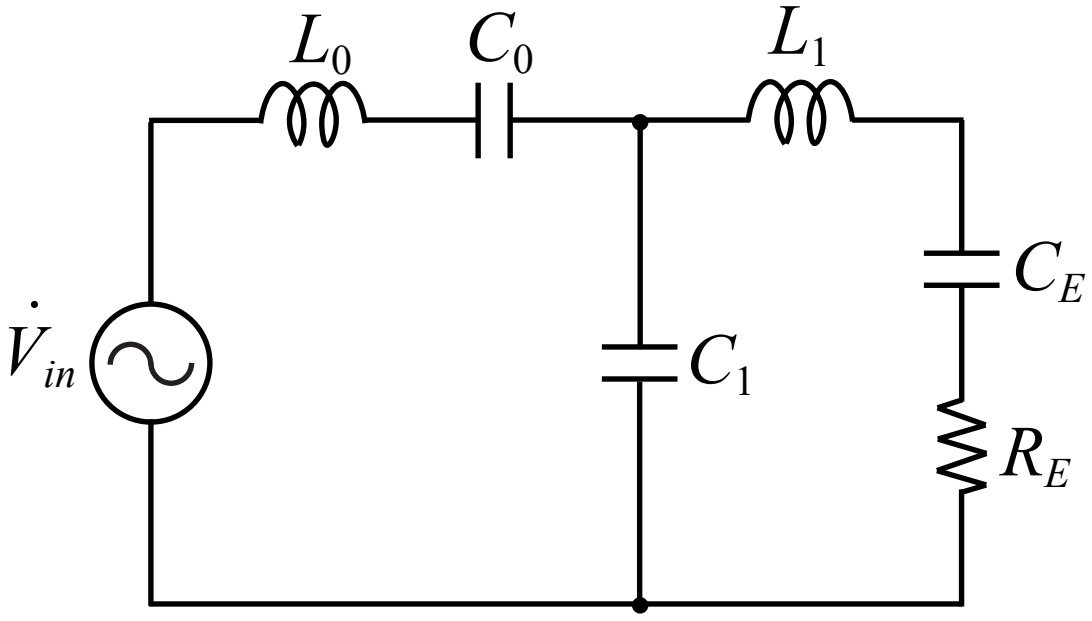

Fig. 7.2: Equivalent circuit model of the proposed rectifier.

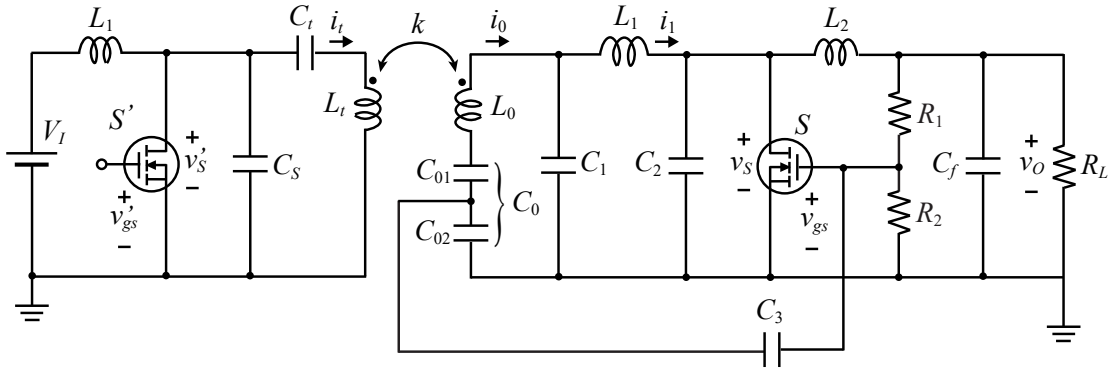

Fig. 7.3: Circuit configuration of the WPT system with the proposed rectifier for the experimental verifications.

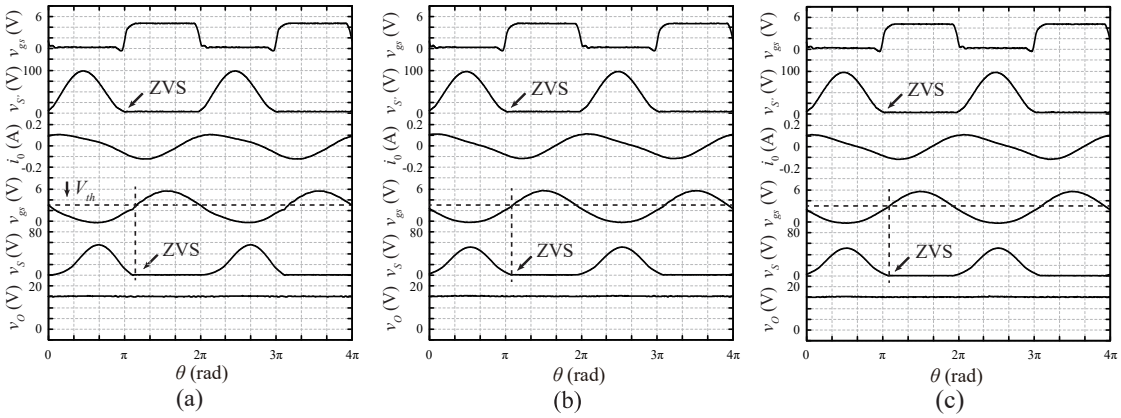

Fig. 7.4: Experimental waveforms of the WPT system with proposed rectifier for fixed load resistance. (a) For $R_L/R_{Lr} = 1$. (b) For $R_L/R_{Lr} = 5$. (c) For $R_L/R_{Lr} = 10$.

Table 7.1: Component values of the WPT system.

L_I	2.12μH	C_t	40.4pF
L_t	14.1μH	C_{01}	85.9pF
L_0	14.0μH	C_{02}	327pF
L_1	5.87μH	C_1	93.9pF
L_2	1.23μH	C_2	68.0pF
k	0.45	C_3	0.1μF
C_S	33.0pF	C_f	0.1μF

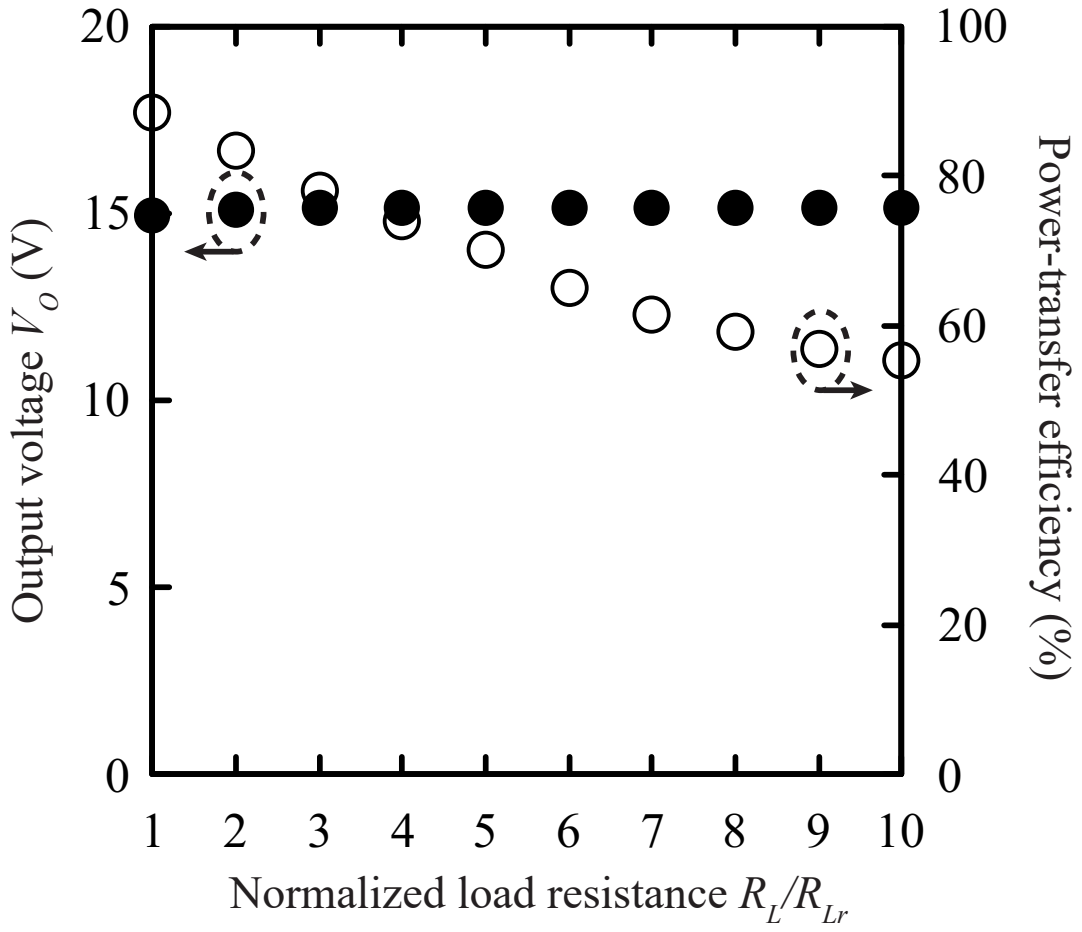

Fig. 7.5: Output voltage and power-transfer efficiency as functions of normalized load resistance.

References

[1] X. Huang, Y. Dou, S. Lin, Y. Tian, Z. Ouyang, and M. A. E. Andersen, "Synchronous push-pull class E rectifiers with load-independent operation for megahertz wireless power transfer," IEEE Trans. Power Electron., vol. 36, no. 6, pp. 6351-6363, June 2021.

[2] S. Aldhaher, D. C. Yates, and P. D. Mitcheson, "13.56MHz 50W load-independent synchronous class E rectifier using GaN devices for space-constrained applications," in Proc. IEEE Wireless Power Transfer Conf. (WPTC), Montreal, QC, Canada, 2018, pp. 1-4.

[3] C. D. Rouse and A. Tahavorgar, "Multi-megahertz load independent synchronous rectifier for resonant wireless power transfer applications," in Proc. IEEE Appl. Power Electron. Conf. Expo. (APEC), Houston, TX, USA, 2022, pp. 505-511.

[4] X. Huang, Z. Yu, Y. Dou, S. Lin, Z. Ouyang, and M. A. E. Andersen, "Load-independent push-pull class E2 topology with coupled inductors for MHz-WPT applications," IEEE Trans. Power Electron., vol. 37, no. 7, pp. 8726-8737, July 2022.

[5] S. Aldhaher, D. C. Yates, and P. D. Mitcheson, "Load-independent class E/EF inverters and rectifiers for MHz-switching applications," IEEE Trans. Power Electron., vol. 33, no. 10, pp. 8270-8287, Oct. 2018.

[6] H. Sekiya, K. Tokano, W. Zhu, Y. Komiyama, and K. Nguyen, "Design procedure of load-independent class-E WPT systems and its application in robot arm," IEEE Trans. Ind. Electron., vol. 70, no. 10, pp. 10014-10023, Oct. 2023.

[7] L. Roslaniec, A. S. Jurkov, A. A. Bastami, and D. J. Perreault, "Design of single-switch inverters for variable resistance/load modulation operation," IEEE Trans. Power Electron., vol. 30, no. 6, pp. 3200-3214, June 2015.

Chapter 8

Overall Conclusion and Future Work

8.1 Overall Conclusion

This thesis presents high-frequency load-independent resonant circuits, including inverter, power oscillator, and synchronous rectifier. Several load-independent inverters have been proposed in this study. Furthermore, the load-independent design for the inverter is applied to power oscillators. By discovering the time-reversal duality between power oscillators and synchronous rectifiers, the load-independent design for power oscillators can also be applied to synchronous rectifiers. Consequently, it was demonstrated that the load-independent design for inverters can be extended to power oscillators and synchronous rectifiers.

Chapter 3 presents the analysis and design of the load-independent series resonant inverter with CC output, along with its WPT system application. The proposed inverter inherently achieves ZCS and a CC output regardless of the load resistance. Furthermore, the proposed inverter can generate a sufficiently pure sinusoidal output even with a low-Q SR filter. In the experiment, the WPT system that incorporates

the proposed inverter as the transmitter was implemented.

Chapter 4 has proposed the design of the load-independent class-Φ_3 inverter. The load-independent class-Φ_3 inverter achieves the ZVS and constant AC output voltage regardless of the load resistance. Additionally, it achieves higher efficiency and power-output capability than the load-independent class-Φ_2 inverter. In the experiment, the load-independent class-Φ_3 inverter achieved 87.5 %-95.9 % power-conversion efficiency within a tenfold change in the load resistance, showing the effectiveness of the proposed inverter.

Chapter 5 has proposed the self-tuned series resonant power oscillator with LI operation. The proposed oscillator maintains high efficiency and constant AC output even with load variations and component tolerances. The experimental results show the effectiveness of the proposed power oscillator.

Chapter 6 has proposed the load-independent class-E power oscillator. The proposed power oscillator inherently achieves the ZVS regardless of the load resistance. Additionally, the amplitude and phase shift of both gate-drive voltage and output current are also independent of the load. These features enable the circuit to oscillate with high stability and efficiency over a wide range of load variations. The experimental results demonstrated the effectiveness of the proposed power oscillator.

Chapter 7 has proposed the load-independent class-E synchronous rectifier with a passive feedforward network. The proposed rectifier generates the synchronized drive voltage using the voltage across the resonant capacitor. Therefore, additional phase-detection circuits and digital devices are not required for the synchronous rectification. Moreover, the proposed synchronous rectifier achieves the ZVS and constant output voltage against load variations. The validity and effectiveness of

the proposed rectifier are confirmed by the experiment.

Chapter 8 shows the conclusion of this thesis. Additionally, future research topics are introduced in this section.

8.2 Future Work

Thus far, load-independent design has been applied to fundamental power electronics circuits, such as DC-AC converters and AC-DC converters. In the future, I plan to research DC-DC converters and WPT systems, which combine these basic circuits. In particular, the synchronous rectifier proposed in this study does not require auxiliary power supplies or additional digital devices, making it highly suitable for application on the secondary side of WPT systems. Furthermore, there are a few examples of WPT systems utilizing power oscillators, and this is one of the areas I want to explore in the future.

Research achievements

Academic journal papers

- W. Zhu, A. Komanaka, **Y. Komiyama**, H. Koizumi and H. Sekiya, "Simultaneous Wireless Power and Data Transfer System with Reconfigurable Load-Independent Class-E Inverter," IEEE Journal of Emerging and Selected Topics in Power Electronics. (Accepted)

- A. Konishi, K. Onodera, **Y. Komiyama**, X. Wei, K. Nguyen, and H. Sekiya, "High-Frequency Load-Independent WPT System for Multiple-Receiver with LCC-S Compensators," IEEJ Journal of Industry Applications, 2024. (Accepted)

- H. Wan, **Y. Komiyama**, X. Wei, A. Konishi, K. Nguyen, and H. Sekiya, "Analysis and Design of High-Frequency Multiple-Output WPT System with Load-Independent Class-E/F Inverter," International Journal of Circuit Theory and Applications, 2024. (Accepted)

- Y. Xie, W. Zhu, **Y. Komiyama**, A. Komanaka, A. Konishi, X. Wei, K. Nguyen, and H. Sekiya, "Load-Independent Class-E Frequency Multipliers," IEEE Transactions on Circuits and Systems I: Regular Papers, vol. 71, no. 5,

pp. 2443-2456, May 2024.

- **Y. Komiyama**, A. Komanaka, W. Zhu, A. Konishi, K. Nguyen and H. Sekiya, "Analysis and Design of Load-Independent Series Resonant Power Amplifier With Constant Current Output and Its Application for WPT System," IEEE Transactions on Power Electronics, vol. 39, no. 5, pp. 6515-6525, May 2024.

- **Y. Komiyama**, A. Komanaka, H. Ota, Y. Ito, T. Mishima, T. Uematsu, A. Konishi, W. Zhu, K. Nguyen, and H. Sekiya, "Analysis and Design of High-Frequency WPT System Using Load-Independent Inverter With Robustness Against Load Variations and Coil Misalignment," IEEE Access, vol. 12, pp. 23043-23056, 2024.

- W. Zhu, **Y. Komiyama**, A. Komanaka, K. Nguyen and H. Sekiya, "Analysis of Load-Independent ZCS Parallel-Resonant Inverter With Constant Current," IEEE Transactions on Industrial Electronics, vol. 71, no. 9, pp. 10433- 10443, Sept. 2024.

- H. Sekiya, K. Tokano, W. Zhu, **Y. Komiyama**, and K. Nguyen, "Design procedure of load-independent class-E WPT systems and its application in robot arm," IEEE Transactions on Industrial Electronics, vol. 70, no. 10, pp. 10014- 10023, Oct. 2023.

- **Y. Komiyama**, S. Matsuhashi, W. Zhu, T. Mishima, Y. Ito, T. Uematsu, K. Nguyen, H. Sekiya, "Wireless power transfer system with load-independent inverse class-E oscillator," IEICE Nonlinear Theory and Its Application, vol. E13-N, No.2, Apr. 2022.

- **Y. Komiyama**, S. Matsuhashi, W. Zhu, T. Mishima, Y. Ito, T. Uematsu, K. Nguyen, H. Sekiya, “Frequency-modulation controlled load-independent class-E inverter,” IEEE Access, vol.9, pp.144600-144613, Nov. 2021.

- W. Zhu, **Y. Komiyama**, K. Nguyen, and H. Sekiya, “Comprehensive and simplified numerical design procedure for class-E switching circuits,” IEEE Access, vol. 9, pp. 149971-149981, Oct. 2021.

International conferences

- T. Kobayashi, **Y. Komiyama**, A. Konishi, K. Nguyen, and H. Sekiya, ”Design of Capacitive Power Transfer System,” IEEE Workshop on Nonlinear Circuit Networks (NCN2024), Tokushima, Japan, Dec. 2024.(Accepted)

- N. Fukuda, **Y. Komiyama**, Y. Xie, A. Komanaka, W. Zhu, A. Konishi, K. Nguyen, and H. Sekiya, ”Design of Magnetic Resonant WPT Systems,” IEEE Workshop on Nonlinear Circuit Networks (NCN2024), Tokushima, Japan, Dec. 2024.(Accepted)

- R. Kaneiso, A. Komanaka, Y. Xie, **Y. Komiyama**, A. Konishi, K. Nguyen, and H. Sekiya, ”Design of Resonant Converter with Genetic- Algorithm Optimization,” 2024 21st International SoC Design Conference (ISOCC), Sapporo, Japan, 2024, pp. 211-212.

- T. Kobayashi, **Y. Komiyama**, A. Konishi, H. Ota, Y. Ito, T. Mishima, T. Uematsu, K. Nguyen, and H. Sekiya, ”Analysis and Design of Capacitive Cou-

pling Wireless Power Transfer System Using Load-Independent Class-EF Inverter," IEEE Applied Power Electronics Conference and Exposition (APEC), Atlanta, GA, USA, 2025. (Accepted)

- Y. Xie, W. Zhu, **Y. Komiyama**, A. Komanaka, A. Konishi, K. Nguyen, and H. Sekiya, "Design of Dual-Frequency Rectifier in Wireless Power Transfer Systems," International Conference on Renewable Energy Research and Application (ICRERA), Nov. 2024. (Accepted)

- **Y. Komiyama**, W. Zhu, A. Konishi, K. Nguyen, and H. Sekiya, "Design of Load-Independent Class-Φ 3 Resonant Inverter", IEEE Energy Conversion Congress and Exposition (ECCE), Phoenix, AZ, USA, Oct. 2024. (Accepted)

- W. Zhu, A. Komanaka, **Y. Komiyama**, K. Nguyen, and H. Sekiya, "Load-independent Class-E Inverter with ASK Modulation", IEEE Energy Conversion Congress and Exposition (ECCE), Phoenix, AZ, USA, Oct. 2024. (Accepted)

- **Y. Komiyama**, W. Zhu, A. Konishi, K. Nguyen, and H. Sekiya, "Design of Self-Oscillating Class-E Inverter", Taiwan and Japan Conference on Circuit and Systems (TJCAS), Kumamoto, Japan, Aug. 2024.

- **Y. Komiyama**, W. Zhu, A. Konishi, K. Nguyen, and H. Sekiya, "Design of Class-Φ 3 Power Oscillator", IEEE International Symposium on Circuits and Systems (ISCAS), Singapore, Singapore, May 2024, pp. 1-5.

- A. Konishi, K. Onodera, **Y. Komiyama**, K. Nguyen, H. Sekiya and X. Wei, "Load-Independent Multiple Output WPT System With Fixed Coupling

Coils," International SoC Design Conference (ISOCC), Jeju, Korea, Republic of, 2023, pp. 165-166.

- W. Zhu, A. Komanaka, **Y. Komiyama**, X. Wei, K. Nguyen and H. Sekiya, "Reconfigurable Class-E/EF Load-independent Inverter With CC-CV Output," IEEE Energy Conversion Congress and Exposition (ECCE), Nashville, TN, USA, 2023, pp. 2307-2312.

- H. Wang, **Y. Komiyama**, A. Konishi, K. Nguyen, H. Sekiya and X. Wei, "Load-Independent High-Frequency WPT System for Multiple Receivers with Single Transmitter," IEEE Annual Conference of the Industrial Electronics Society (IECON), Singapore, Singapore, 2023, pp. 1-6.

- **Y. Komiyama**, W. Zhu, A. Komanaka, X. Wei, K. Nguyen, and H. Sekiya, "Self-tuned series resonant power oscillator with load-independent operation," IEEE International Symposium on Circuits and Systems (ISCAS), Monterey, CA, USA, May 2023, pp. 1-5.

- Y. Xie, W. Zhu, **Y. Komiyama**, K. Nguyen, and H. Sekiya, " Analysis and Design of Push-pull Load-independent Class-E Frequency Tripler", International Workshop on Nonlinear Circuits, Communications and Signal Processing (NCSP'23), Mar. 2023.

- Y. Hirama, A. Komanaka, **Y. Komiyama**, W. Zhu, K. Nguyen, X. Wei, and H. Sekiya, " Simulator-based optimization software for high-frequency power-electronics circuits," IEEE International Symposium on Circuits and Systems (ISCAS), Monterey, CA, USA, 2023, pp. 1-5.

- T. Matsuda, **Y. Komiyama**, W. Zhu, K. Nguyen and H. Sekiya, "Maximum Efficiency Tracking for Wireless Power Transfer with Multiple Receivers," International SoC Design Conference (ISOCC), Gangneung-si, Korea, Republic of, 2022, pp. 227-228.

- **Y. Komiyama**, W. Zhu, X. Wei, K. Nguyen, and H. Sekiya, " Wireless Power Transfer System with Series Resonant Inverse Class-E Inverter," International Workshop on Nonlinear Circuits, Communications and Signal Processing (NCSP'23), pp.194-197, Mar.

- Y. Xie, W. Zhu, **Y. Komiyama**, K. Nguyen, and H. Sekiya, "Design of Class-E Frequency Doubler Corresponding to Load Variations in Large Ranges," IEEE Workshop on Nonlinear Circuits Networks (NCN2022), Dec. 2022.

- W. Zhu, **Y. Komiyama**, K. Nguyen and H. Sekiya, "Achievement of CV and CC Output Modes on Class-E/F Inverter with One Auxiliary Switch," IEEE International Symposium on Circuits and Systems (ISCAS), Austin, TX, USA, 2022, pp. 2635-2639.

- **Y. Komiyama**, S. Matsuhashi, W. Zhu, K. Nguyen, T. Uematsu, Y. Ito, T. Mishima, and H. Sekiya, " Wireless Power Transfer System with Load-Independent Inverse Class-E Oscillator," Nonlinear Science Workshop (NLSW2021), p.39, Dec. 2021.

- **Y. Komiyama**, S. Matsuhashi, W. Zhu, K. Nguyen, T. Uematsu, Y. Ito, T. Mishima, and H. Sekiya, "Constant Voltage Output Autonomous Wireless Power Transfer System," IEEE Workshop on Nonlinear Circuit Networks

(NCN2021), pp.21-24, Dec. 2021.

- W. Zhu, **Y. Komiyama**, K. Nguyan and H. Sekiya, "PSO-based Design Procedure for Class-DE Inverter," International SoC Design Conference (ISOCC), Jeju Island, Korea, Republic of, 2021, pp. 173-174.

- **Y. Komiyama**, W. Zhu, K. Nguyen, and H. Sekiya, "Load-independent constant-current/zero-current switching inverter with series resonant filter," IEEE Applied Power Electronics Conference and Exposition (APEC), Orlando, FL, USA, 2023, pp. 490-494.

- **Y. Komiyama**, S. Matsuhashi, W. Zhu, T. Mishima, Y. Ito, T. Uematsu, K. Nguyen, H. Sekiya, "Load-Independent Inverse Class-E Oscillator with Armstrong-Oscillator Based Topology," International SoC Design Conference (ISOCC), Jeju Island, Korea, Republic, Oct. 2021, pp. 175-176.

- W. Zhu, **Y. Komiyama**, K. Nguyen, and H. Sekiya, "Heuristic algorithm-based design method for class-E switching circuits," IEEE Energy Conversion Congress and Exposition (ECCE), Vancouver, BC, Canada, 2021, pp. 5692-5697.

- **Y. Komiyama**, W. Zhu, K. Nguyen, and H. Sekiya, "Class-E inverter with frequency modulation control," International Conference on Renewable Energy Research and Application (ICRERA), Istanbul, Turkey, 2021, pp. 94-98.

Domestic (Japan) conferences and symposiums

- A. Komanaka, J. Yan, **Y. Komiyama**, Y. Xie, A. Konishi, W. Zhu, X. Wei, K. Nguyen, and Hiroo Sekiya, "Analysis and Design of CC/CV ZVS Wireless Power Transfer System without Wireless Communication Control between Transmitter and Receiver", Technical Committee Energy Eng. Electron. Commun. (EE), Jan. 2024.

- T. Kobayashi, **Y. Komiyama**, A. Konishi, H. Ota, Y. Itoh, T. Mishima, T. Uematsu, K. Nguyen, H. Sekiya, "Analysis and Design of Capasitive Coupling Wireless Power Transfer System with Load-Independent Class-EF Inverter", Technical Committee Energy Eng. Electron. Commun. (EE), EE2024-5, pp. 1-6, July 2024.

- N. Fukuda, **Y. Komiyama**, W. Zhu, Y. Xie, A. Komanaka, A. Konishi, K. Nguyen, H. Sekiya, "Design Method for Load-Independent WPT Systems Using Machine Learning", Technical Committee Energy Eng. Electron. Commun. (EE), EE2023-58, pp.6-11.

- **Y. Komiyama**, A. Konishi, W. Zhu, A. Komanaka, K. Nguyen, H. Sekiya, "Analysis and Design of Class-Φ 3 Power Oscillator", Technical Committee Energy Eng. Electron. Commun. (EE), vol.123, no.343, pp.83-87, Jan. 2024.

- W. Zhu, A. Komanaka, **Y. Komiyama**, K. Nguyen, H. Sekiya, "Design of Load-independent Parallel-resonant Inverter with CC/CV output", Technical Committee Energy Eng. Electron. Commun. (EE), EE2023-56, pp.93-97, Jan. 2024.

- A. Konishi, K. Onodera, **Y. Komiyama**, K. Nguyen, H. Sekiya, "Load-Independent Multiple Output WPT System for Realizing Wire-Free Robots", IEEJ Annu. Conf. Electronics Infromation, and Systems, GS5-7, pp.1318-1323, Sept. 2023.

- J. Yan, W. Zhu, **Y. Komiyama**, A. Konishi, X. Wei, K. Nguyen, H. Sekiya, " Design of CC/CV Output Load-Independent High-Frequency WPT System", Technical Committee Energy Eng. Electron. Commun. (EE), vol.123, no.119, pp.55-60, July 2023.

- H. Wan, **Y. Komiyama**, X. Wei, A. Konishi, K. Nguyen, H. Sekiya, "A multi-receiver WPT system with load-independent class-E/F inverter", Technical Committee Energy Eng. Electron. Commun. (EE), vol.123, no.119, pp.61-66, July 2023.

- J. Yan, W. Zhu, **Y. Komiyama**, Y. Xie, K. Nguyen, H. Sekiya, "バッテリー充電向け定電流/定電圧出力負荷非依存 WPT システムの設計", in Proc. IEICE Engineering Sciences Society/NOLTA Society Conference, no.NLS-41, June 2023.

- H. Wan, **Y. Komiyama**, X. Wei, K. Nguyen, H. Sekiya, "負荷変動及び位置ずれに対してロバストな 6.78MHz 一送電多受電無線電力転送システム", in Proc. IEICE Engineering Sciences Society/NOLTA Society Conference, June 2023.

- W. Zhu, A. Komanaka, **Y. Komiyama**, K. Nguyen, H. Sekiya, "Load-independent Class-E Inverter with Constant-Current and Constant-Voltage Output", Tech-

nical Committee Energy Eng. Electron. Commun. (EE), EE2022-57, pp.13-18, Mar. 2023.

- **Y. Komiyama**, W. Zhu, K. Nguyen, H. Sekiya, "Load-independent constant-current output series-resonant inverter", Technical Committee Energy Eng. Electron. Commun. (EE), EE2022-42, vol.122, no.343, pp.89-94, Jan. 2023.
- Y. Hirama, **Y. Komiyama**, W. Zhu, K. Nguyen, H. Sekiya, "Optimization software for high-frequency converter designs with heuristic algorithm and SPICE", Technical Meeting on Electronic Circuits (ECT), ECT-22-011, Mar. 2022.
- Y. Xie, W. Zhu, **Y. Komiyama**, K. Nguyen, H. Sekiya, "Design of Class-E Frequency Doubler with Robustness to Load Variations", Technical Committee Energy Eng. Electron. Commun. (EE), vol.122, no.109, pp.11-16, July 2022.
- T. Matsuda, **Y. Komiyama**, W. Zhu, K. Nguyen, H. Sekiya, "Maximum efficiency tracking for Wireless Power Transfer with Multiple Receivers", Technical Committee Energy Eng. Electron. Commun. (EE), EE2022-12, pp.22-26, July 2022.
- Y. Xie, W. Zhu, **Y. Komiyama**, K. Nguyen, H. Sekiya, "Analysis and Desugn of Load-independent Class-E Frequency Multiplier", in Proc. IEICE Engineering Sciences Society/NOLTA Society Conference, June 2022.
- T. Matsuda, **Y. Komiyama**, W. Zhu, K. Nguyen, H. Sekiya, "Maximum efficiency tracking for Wireless Power Transfer with Multiple Receivers", in

Proc. IEICE Engineering Sciences Society/NOLTA Society Conference, p.37, June 2022.

- W. Zhu, A. Komanaka, **Y. Komiyama**, K. Nguyen, H. Sekiya, "Particle Swarm Optimization Based Design Method for Class-E Switching Circuits", Technical Committee Complex Commun. Sciences (CCS), CCS2021-42, pp.37-41, Mar. 2022.

- **Y. Komiyama**,K. Nguyen,T. Mishima,Y. Itoh,T. Uematsu,H. Sekiya, "Load-Independent Class-E Inverter with Frequency Modulation Control", Technical Committee Energy Eng. Electron. Commun. (EE), EE2021-8, vol.121, no.124, pp.6-11, July 2021.

Invited Lecture

- **Y. Komiyama**, W. Zhu, A. Konishi, K. Nguyen, and H. Sekiya, "Load-Independent Class-E Power Oscillator and Synchronous Rectifier", IEEE Workshop on Nonlinear Circuit Networks (NCN2024), Tokushima, Japan, Dec. 2024.

Patents

- T. Mishima, Y. Itoh, H. Ota, S. Nagaoka, T. Uematsu, H. Sekiya, **Y. Komiyama**, Wireless Power Transfer System, WPT System, WPT Transmitter and Receiver Circuit, Japan Patent Office, 2024-037070.